Title
Electrical and Thermal Transport Studies on Topologically Non-Trivial Systems

Author
Casas, Brian Wesley

Publication Date
2020

Peer reviewed|Thesis/dissertation

UNIVERSITY OF CALIFORNIA,
IRVINE

Electrical and Thermal Transport Studies on Topologically Non-Trivial Systems

DISSERTATION

submitted in partial satisfaction of the requirements
for the degree of

DOCTOR OF PHILOSOPHY

in Physics

by

Brian Wesley Casas

Dissertation Committee:
Professor Jing Xia Irvine, Chair
Professor Emeritus Zachary Fisk Irvine
Assistant Professor Javier Sanchez-Yamagishi Irvine

2020

Dedication

I would like to dedicate this dissertation to my twin brother, Zach. His support of me since beginning graduate school as continued to help me push through any challenges that I faced. He gave me a picture of what life after school could look like, and it pushed me every day. It hasn't been easy being so far apart, but I'm hoping that I can make more time now.

Table of Contents

List of Figures

Acknowledgements

First and foremost, I would be remiss if I did not acknowledge my advisor, Jing Xi for giving me the opportunity to advance on my educational journey. The freedom that I was allowed in the lab gave me the chance to better develop as a scientist and a leader.

Additionally, I would like to thank both Zachary Fisk and Javier Sanchez-Yamagishi for their wonderful insights and willingness to discuss technical aspects of my experiments and research interests. I always knew that they would be happy to answer any questions that I had. Being able to learn single crystal growth from Zach has been one of the highlights of my research career.

I would like to thank my friends and colleagues, that without whom, progressing through this crazy world of graduate school would have been impossible. From the bottom of my heart, I extend my thanks to: Pavel Maximov, Mingru Yang, Randy Sawaya, Sophia Nsar, Freida Rivera, Jinyu Liu, Ian Sequeira, Paige Lampen, Ellie Clements, Kristen Repa, Zohre Nemati, Javier Alonso, Caitlin Suire, Connor Strobel, Mel Dahlin, Matt Brand, Maureen Purcell.

I must also extend a big thanks to Alex Stern for training me on everything in the lab. Without your presence in the lab the first few years I would not be where I am now.

Special thanks should go to Sahel Hakimi and Sunny Yu. Their friendship since we began coursework together has been invaluable. The many cathartic conversations with Sahel regarding struggles in research kept me going. The numerous fun outings and conversations with Sunny about our research always inspired me. Seeing the crossover in interests, techniques, and theory between Quantum Matter and Quantum Gravity always gave me a jolt of motivation to learn more.

And finally, I must thank my family for their support of over the past 5 years. It has not been easy only seeing them once or twice per year, but I think we made the best of the situation. My weekly Zoom and Netflix sessions with Zach and Lauren made the quarantine life much more bearable.

Vita

RESEARCH INTERESTS
Flux growth of single crystals, strongly correlated systems, unconventional superconductivity, topological materials

EXPERIMENTAL TECHNIQUES
Flux growth single crystals, electrical, magneto, thermal transport, magnetometry, uniaxial strain, sol gel growth nanocrystals, Quantum Design PPMS, Quantum Design SQUID, Oxford Dilution Refrigerator

EDUCATION
September 2015 – August 2020 University of California Irvine
Irvine, California
Ph.D., Condensed Matter Physics
Advisor: Jing Xia
"Electrical and Thermal Transport Studies on Topologically Non-Trivial Systems"

August 2013 – July 2015 University of South Florida
Tampa, Florida
M.S., Materials Physics
Advisors: Hariharan Srikanth
Co-Advisor: Manh-Huong Phan
"Effects of disorder and low dimensionality on frozen dynamics in Ca3Co2-xMnxO6"

August 2009 – May 2013 Rutgers University
New Brunswick, New Jersey
B.S. Physics
Advisor: Sang -Wook Cheong

AWARDS, FELLOWSHIPS, GRANTS
National Science Foundation AGEP Supplement – January 2017 to June 2019 ($130,712)
UCI Associated Graduate Student Travel Award – March 2019
Graduate Assistance in Areas of National Need (GAANN) – October2015 to September 2016 ($65,356)
GMAG Travel Award – March 2015

PUBLICATIONS
(8) **B. Casas***, L. Chen, Z. Fisk, J. Xia, "Thermal Conductivity in sub Kelvin environment of Kondo Insulator under Uniaxial Strain" (in preparation)

(7) A. Stern*, **B. Casas***, J. Pollanen, K. West, L. Pfeiffer, J. Xia, "Strain-induced resistance anisotropy near the FQHE v= 5/2 in two-dimensional GaAs single quantum wells" (in preparation)
(6) L. Pan, A. Grutter, X. Che, T Nozaki, A. Stern, M. Street, B. Zhang, **B. Casas**, Q. L. He, E. S. Choi, S. M. Dissler, D. A. Gilbert, G. Yin, Q. Shao, P. Zhang, Y. Wu, X. Liu, X Kou, S. Masashi, Z. Han, C. Binek, S. Chambers, J. Xia, K. L. Wang, "Exchange interaction in a quantum anomalous Hall insulator/antiferromagnet heterostructure" (in preparation)
(5) L. Pan, X. Liu, Q. L. He, A. Stern, G. Yin, X. Che, Q. Shao, P. Zhang, P. Deng, C.-Y. Yang, **B. Casas**, E. S. Choi, J. Xia, X. Kou, K. L. Wang, "Probing the low temperature limit of the quantum anomalous Hall effect" (in preparation)
(4) P. Lampen-Kelley, E. M. Clements, **B. Casas**, M. H. Phan, H. Srikanth, J. Marcin, I. Skorvanek, H. T. Yi, S.-W. Cheong, "Impact of reduced dimensionality on the correlation length and magnetization dynamics of the spin chain cobaltite Ca3Co2O6", J.M.M.M 494 (2019)
(3) Q.L.He, G. Y, L. Yu, A. J. Grutter, L. Pan, Chui.-Z. Chen, X. Che, G. Y, B. Zhang, , Q. Shao, A. Stern, **B. Casas**, J. Xia, X. Han, B. J. Kirby, R. K. Lake, K. T. Law, K. L. Wang, "Topological transitions induced by antiferromagnetism in a thin-film topological insulator", Phys. Rev. Lett. 121 (2018)
(2) **B. Casas***, A. Stern, D.K.Efimkin, Z. Fisk, J. Xia, "Direct observation of surface-state thermal oscillations in SmB6 oscillators", Phys. Rev. B 97 (2018)
(1) S.-Z. Lin, X. Wang, Y. Kamiya, G.-W. Chern, F. Fan, D. Fan, **B. Casas**, Y. Liu, V. Kiryukhin, W. H. Zurek, C. D. Batista & S.-W. Cheong, "Topological defects as relics of emergent continuous symmetry and Higgs condensation of disorder in ferroelectrics", Nat. Phys 10 970-977 (2014)

POSTERS & PRESENTATIONS

Oral Presentation: "Search for charge neutral majorana fermions in SmB_6 under uniaxial strain" APS March Meeting (2019), Boston, Massachusetts
Oral Presentation: "Direct Observation of Surface State Thermal Oscillations in SmB_6 Oscillators" APS March Meeting (2018), Los Angeles, California
Poster Presentation: "Frozen spin dynamics and complex phase diagram of the quasi-one dimensional Ising spin chain $Ca_3Co_{2-x}Mn_xO_6$" MMM (2016) San Diego, California
Invited Panelist: "Peer Mentoring" APS National Mentoring Community & Bridge Program Conference (2015), Miami, Florida
Oral Presentation: "Effects of magnetic site disorder of the 1-D Ising spin chain compounds $Ca_3(Co,Mn)_2O_6$ with dilute doping" APS March Meeting (2015), San Antonio, Texas

ACADEMIC AND COMMUNITY SERVICE

Associated Graduate Student Council (2017-2019)
Acted as an elected representative of the School of Physical Sciences.
Peer Mentorship Program (UCI)
Mentored three incoming graduate students of color.
Member of American Physical Society
Member of Physics Graduate Caucus (UCI)
Member of Women in Physics (UCI)
APS Bridge Program Mentor Supervisor (USF)

Supervised a mentorship program associated with the APS Bridge Program site at USF. I helped structure and coordinate this program to help offer support for the incoming Bridge Fellows in order to help these students succeed in graduate school.

Abstract of the Dissertation

Electrical and Thermal Transport Studies on Topologically Non-Trivial Systems

by

Brian Casas

Doctor of Philosophy in Physics

University of California, Irvine, 2020

Professor Jing Xia, Chair

Topology has become a topic that has become ubiquitous in Condensed Matter Physics over the last decade or so with the observations of topological insulators, Dirac and Weyl semimetals, topological superconductors, etc. These materials exhibit a wide array of physical properties of both academic and industrial interest. As such, understanding existing topological phases is of interest for both Physics purists (like myself) and those interested in exploiting these properties for technological gains. In this dissertation, I explore the properties of two topologically (potentially) non-trivial systems, the Fractional Quantum Hall state, and proposed topological Kondo insulator SmB_6.

The observation of voltage oscillations in a single crystal of cryogenically cooled SmB_6 that had been proposed to be related to bulk-surface conduction crossover presented a question regarding the implicit thermal mechanism. As such I explored the time dependent thermal oscillations in SmB_6 that gave rise to the potential high frequency oscillations.

My introduction to uniaxial strain came simultaneously with projects looking to explore the thermal conductivity of SmB_6 in order to probe the possible existence of bulk neutral excitations, as well as to study the emergent nematic state in $\nu = 5/2$ state in a two dimensional electron gas hosted in semiconductor quantum wells.

By subjecting the two-dimensional electron gas to uniaxial strain while electrons sit in the $\nu = 5/2$ state we found that stripe phases can be made to emerge. In addition to this behavior, we noted the effect of strain was dramatically coupled to the Landau Level at which the electrons sit during the strain application.

Finally, the development of a novel thermal transport experimental design for use in uniaxial strain cells was pursued for the purpose of understanding the bulk excitations in SmB_6. A symmetrized thermal conductivity technique was developed for single crystals that is compatible with uniaxial strain experiments. Preliminary measurements show that when care is taken in the sample preparation, the measured values of $\kappa(T)$ are in good agreement with theory and conventional thermal conductivity experiments, making this technique useful for a broad array of experiments.

Chapter 1

Topology and Topological Phases of Matter

One of the greatest successes of Condensed Matter Physics was the ability to understand the microscopic origins and macroscopic behavior of phase transitions. The Ginzburg-Landau formalism provided a perturbative power series expansion of the Free Energy functional of an order parameter[1,2]. This order parameter is a field, specific to the phases of matter of interest, that takes on a finite value in an ordered phase from a value of zero in the disordered phase. This formalism is specifically valid at phase transitions at which order parameter breaks symmetries

allowed by the Hamiltonian (in the ordered state)[1,3]. This work proved to be remarkably useful in understanding the physics of a massive set of both classical and quantum phases of matter including magnetism and superconductivity. This laid the framework for the BCS theory of superconductivity among many others[4]. However, it became clear that perhaps symmetry could not be the only consideration for the transformation of phases of matter.

It was in this context that Topology was introduced into the field of phase transitions and in understanding electronic phases of matter. The Quantum Hall state, a phase in which electronic phase transitions occur with identical symmetries was explained through invoking topology of the system[5,6].

This work opened an entirely new field within Condensed Matter Physics that would lead to the proposal and shortly thereafter, discovery of Topological Insulators, materials that while gapped in the bulk, laid host to metallic surface states.

1.1 Origin of Topology in Condensed Matter Physics

Topology is a field of modern Mathematics that is concerned with the properties of geometric objects. Famously, and maybe a somewhat a tongue-in-cheek example, one may show that through Topology objects such as a coffee cup and a donut, or a cow and a sphere are topologically equivalent, or homeomorphs of one another[7].

First it is useful to discuss the effects of curvature on a vector undergoing parallel transport, motion along a closed path in which the vector is rotated to remain as close to parallel to the trajectory as feasible[7]. We may consider a vector that is confined to move along a circular closed path in a two-dimensional space. One can show that as the vector is moved along this close path that the vector

returns to its original orientation when it arrives back at the origin of motion. This is a consequence of the lack of Gaussian Curvature in two-dimensional space[7]. However, higher dimensional space is not so simple. If this example is extended to a vector moving along the surface of a sphere the behavior is radically different. In fact, it can be shown that a set of vectors that are maintained as close to parallel to the path of displacement as possible undergo a rotation simply by virtue of moving along with closed path in a curved space. This angle of rotation is known as Berry phase[8].

While this sample is easily illustrative of the concept of Berry phase, it is not exactly evident how it plays into the behavior of physical particles that give rise to the electronic or magnetic properties discussed in this dissertation. For that, we must shift away from the picture of a physical space and recall that in Quantum Mechanics orthogonal eigen vectors are used to define a space called Hilbert Space[8,9]. It is within this space we can ask, how does transforming a state along some closed path in Hilbert Space relate to a Berry phase? To understand this, we can start with the time dependent Schrodinger Equation, equation 1.

$$\mathcal{H}\left(\vec{R}(t)\right)|\psi(t)\rangle = i\hbar\frac{d}{dt}|\psi(t)\rangle \tag{1}$$

Here we can define the state $|\psi(t)\rangle$ in equation 2. Here we are taking our system to be tunable through a parameter variable in time, $\vec{R}(t)$. We note that this parameter may be something tunable in the lab such as magnetic field, strain, pressure, etc.

$$|\psi(t)\rangle = e^{-i\vec{\theta}(t)}\left|n\left(\vec{R}(t)\right)\right\rangle \tag{2}$$

$$E_n\left(\vec{R}(t)\right)\left|n\left(\vec{R}(t)\right)\right\rangle = \hbar\left(\frac{d}{dt}\theta(t)\right)\left|n\left(\vec{R}(t)\right)\right\rangle + i\hbar\frac{d}{dt}\left|n\left(\vec{R}(t)\right)\right\rangle \tag{3}$$

The phase here, θ(t), unfortunately, is not the Berry phase as discussed earlier, but it can be further

shown that the right most equality in equation 1 can be expanded in terms of this definition of our state in equation 2, yielding the result in equation 3. there it is clear that there are now two terms, the first exclusively concerning this phase factor and its evolution in time. We can take the scalar product of equation 3 with $\langle n(\vec{R}(t))|$ resulting in:

$$E_n\left(\vec{R}(t)\right) - i\hbar\left\langle n\left(\vec{R}(t)\right)\middle|\frac{d}{dt}\middle|n\left(\vec{R}(t)\right)\right\rangle = \hbar\left(\frac{\partial}{\partial t}\theta(t)\right). \tag{4}$$

From here it is possible to extract a formulation directly for the phase factor θ(t) as

$$\theta(t) = \frac{1}{\hbar}\int_0^t E_n\left(\vec{R}(t')\right)dt' - i\int_0^t \left\langle n\left(\vec{R}(t')\right)\middle|\frac{d}{dt}\middle|n\left(\vec{R}(t')\right)\right\rangle dt'. \tag{5}$$

Now we arrive at useful information about the phase of our state ψ(t). Here the first term is simply the dynamical phase factor, which typically does not play a role in the physical properties of a particle in state ψ (recalling that physical properties rely on a scalar multiplication which effectively nullifies this phase)[8,9]. The negative of the second term is in fact the Berry phase we sought.

$$|\psi(t)\rangle = e^{-i\frac{1}{\hbar}\int_0^t E_n\left(\vec{R}(t')\right)dt'}e^{i\gamma_n}\left|n\left(\vec{R}(t')\right)\right\rangle \tag{6}$$

$$\gamma_n = i\int_0^t \left\langle n\left(\vec{R}(t')\right)\middle|\frac{d}{dt'}\middle|n\left(\vec{R}(t')\right)\right\rangle dt' \tag{7}$$

Substituting equation 5 into equation 2 yields equation 6 in which we defined the Berry phase, γ_n in equation 7. The physical origin of the Berry phase comes from this fact that the states at a time t and t+dt are not identical[10]. While the Berry phase is important, what is actually required for our

understanding of the topology of the Hilbert space is actually related to the curvature of this space. As such we can show that the Berry phase may be used to calculate the curvature.

Since we chose to vary our parameter $\vec{R}(\mathrm{t})$, as a function of time, we can replace any time dependence and show that γ_n can be rewritten as

$$\gamma_n = i \int_C \langle n(\vec{R}) | \nabla_{\vec{R}} | n(\vec{R}) \rangle \, d\vec{R}. \tag{8}$$

Now, by analogy to Electromagnetic Theory, a Berry vector potential is defined by

$$\vec{A}(\vec{R}) = i \left\langle n(\vec{R}) \left| \frac{\partial}{\partial \vec{R}} \right| n(\vec{R}) \right\rangle, \tag{9}$$

and as such the Berry phase can now be redefined as

$$\gamma_n = \int_C d\vec{R} \cdot \vec{A}_n(\vec{R}). \tag{10}$$

It should be noted here that the Berry phase should be real and as such should be rewritten as

$$\gamma_n = -Im \int_C \langle n(\vec{R}) | \nabla_{\vec{R}} | n(\vec{R}) \rangle \, d\vec{R}. \tag{11}$$

Now using Stokes Theorem, we can choose to rewrite this formulation in equation 11 in terms of surface S as written in equation 12:

$$\gamma_n = -Im \iint_S d\vec{S}' \cdot \left(\vec{\nabla} \times \langle n(\vec{R}) | \vec{\nabla} | n(\vec{R}) \rangle \right). \tag{12}$$

We can now simplify equation 12, as seen in equation 13, in terms of a new quantity, called the Berry curvature.

$$\gamma_n = -Im \iint_S d\vec{S}' \cdot (\langle \vec{\nabla} \mathrm{n}(\vec{\mathrm{R}}) | \times | \vec{\nabla} n(\vec{R}) \rangle) \ . \tag{13}$$

Here we can now define a property called the Berry curvature in the following way:

$$F = \langle \vec{\nabla} n(\vec{R}) | \times | \vec{\nabla} n(\vec{R}) \rangle \, . \tag{14}$$

Now, for the purposes of the discussion here we can stop at the definition of Berry curvature, which in this system, can be thought of as playing the role of magnetic field, as it is defined as the curl of the Berry vector potential. The point I should make here is that this property is one that describes the curvature of the Hilbert space that has been defined by orthonormal eigenstates defined in equation 2. The arrival at a definition for the curvature of this space is critical for understanding the nature of the topology of this space our states lie in.

However, curvature is no substitute for topology. Here we can invoke the Bonnet-Gauss Theorem to connect the curvature of a region with its associated topology. This theorem allows for the direct connection of the Guassian curvature of a bounded region by a nongeodesic[7] simple curve and the topology of a compact surface, equation 15.

$$\frac{1}{2\pi} \oint_{\substack{Closed \\ Surface}} F dA = 2 - 2g \tag{15}$$

Here I should point out that quantity g is an integer called a topological invariant and allows for some simple topological classification of a region. The invariant, g, simply counts the number of

holes in a surface. A few examples would include g=0 for a sphere, g=1 for a torus, etc. As such, any two objects of identical genus can be smoothly deformed to one another, much like the donut and coffee cup example from earlier.

It is with the use of topological invariants that physicists can classify topologically distinct phases of matter. Due to the fact that this invariant is an integer and only allowed to transform in this discrete way, the inability to smoothly transform one topological phase to a distinct topological phase is of profound significance. This very notion is connected to the concept of Adiabaticity. For instance, two insulating phases can be adiabatically connected if a band structure can be smoothly deformed, or a parameter slowly turned on, to modify the size of the gap without its closure. It can be proven that in order to transform between two topologically distinct phases requires the closure of an energy gap before it can be reopened with a new topological invariant. An illustration of this can be seen in figure 1.1 in which both a topological and non-topological phase transition is pictured.

There are a large number of topological invariants, though two will be specifically discussed in later sections of this work to describe the Quantum Hall State and Spin Hall or Topological Insulator states.

These topological invariants prove to be extremely useful. As a matter of fact, most phases of matter in modern physics has been described by a phenomenological order parameter, as used in Ginsberg Landau Theory[1]. However, no such local order parameter exists for systems that may be described as Topologically Non-trivial. As such, a topological invariant can play such a role in distinguishing between phases that are topologically distinct.

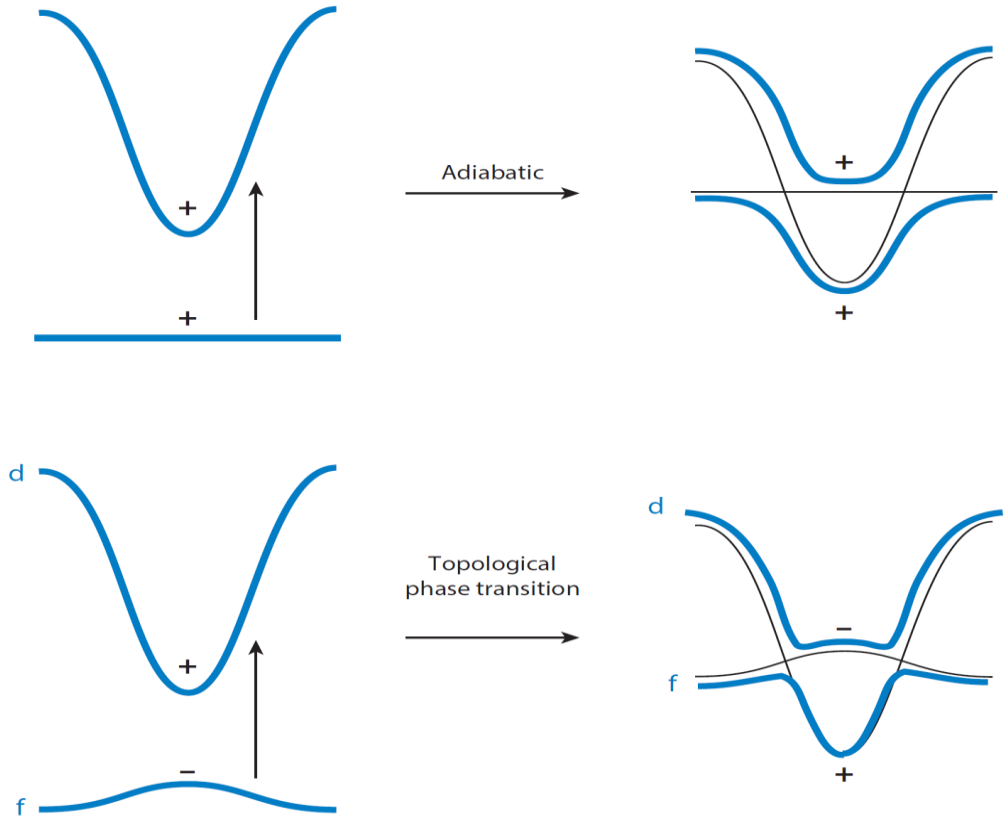

Figure 1.1: Cartoon of two band structures in which the band gap is decreased smoothly. He top scenario begins closing the gap, but due to the identical parity of the bands, repulsion occurs instead of band crossing leading to a topologically trivial change. However, the bottom cases represent a scenario in which the gap is closed before reopening, now with band crossings, leading to a topological phase transition.

1.2 Topological Phases

1.2.1 Quantum Hall Effect

The Hall Effect classically describes the behavior of charge carriers, whether they be electrons or holes, and their response to a magnetic field[2]. This work largely relies on the underpinning of the Lorentz Force, which describes a force perpendicular to a charged objects velocity and the external

magnetic field through which it travels. This force causes a deflection of the charge carrier trajectory away from the direction of the applied electric potential and leads to charge accumulation on the edges of a material. This accumulation of charges of opposite signs on opposite edges of the sample (remembering particles charged oppositely will experience a deflecting force in opposite directions) leads to an established electrical potential transverse to the applied electric potential.

However, strikingly, in clean samples of two-dimensional semiconductors, large resistance plateaus were observed in which the resistance was found to be quantized. This could be understood from a somewhat simple picture in which the electronic density of states is filled uniformly up to the Fermi Energy, as per the definition. However, upon the application of an external magnetic field, electrons begin to undergo circular orbits leading to Landau level quantization[11]. The solution to such a Hamiltonian is simply that of the harmonic oscillator in the confined plane of the sample. An observation of this effect requires clean samples due to the requirement that scattering times are longer than a single orbital period. The formation of these orbits, and by extension, Landau levels, creates a bulk in which there exist states separated by $\Delta \sim \hbar\omega_c$ worth of energy. As such when the Fermi energy lies within any of these gaps, the bulk becomes insulating.

This simple picture of electron orbits leads to another somewhat surprising consequence, a conducting edge state. These edge states can be thought of as incomplete orbits that lead to a skipping motion along the edge of the sample. This means that there exist now a set of states that carry current along the edge of an otherwise insulating bulk[12].

However, this picture is not the only one that describes the nature of the Quantum Hall Effect, and actually it is the second picture that leads to a more interesting (in my own opinion) reason to continue studying this state. It was realized that the quantization of the σ_{xy}, the Hall conductance, could be in fact a consequence of the topological nature of the system. In fact the conductance was able to be calculated in the seminal work by Thouless, Kohmoto, Nightingale, and den Nijs (TKNN)[6] in which a topological invariant, ν_{TKNN}, was used to explain the quantization of σ_{xy}, equation 16.

$$\sigma_{xy} = \frac{e^2}{h}\frac{1}{2\pi}\,\nu_{TKNN} \tag{16}$$

$$\nu_{TKNN} = \frac{1}{2\pi}\oint_C \vec{A}(\vec{R})\cdot d\vec{R} = \frac{1}{2\pi}\int_{BZ} \vec{F}(\vec{R})d^2\vec{R} \tag{17}$$

Here ν_{TKNN}, equation 17, is the topological invariant that distinguishes the separate insulating phases within the QHE. Note the inclusion of the Berry vector potential or the Berry curvature. The value of ν_{TKNN} can be also thought to represent the precise number of edge states that intersect the Fermi Energy, one for each Landau level beneath E_F. This relationship between topology and gapless edge modes had been observed in an analysis of one-dimensional field[13] theories as well as in a description of a possible soliton state in polyacetalene[14].

This topological nature of the QHE is precisely why this quantization has been measured down to about 1 part in $10^{(9)}$[15]. This also seems to explain the existence of these conductive edge modes. Due to the non-trivial topological nature of the QHE and the interface to vacuum (considered a trivial insulator) a gapless edge state must appear. As discussed earlier, it can be shown that the energy gap must close across a boundary between two insulators with differing topological

invariants. A cartoon of this edge mode can be seen in figure 1.2[16]. This edge mode is known to travel in a single direction controlled by the direction of the applied magnetic field, and as such the direction of the electronic orbits.

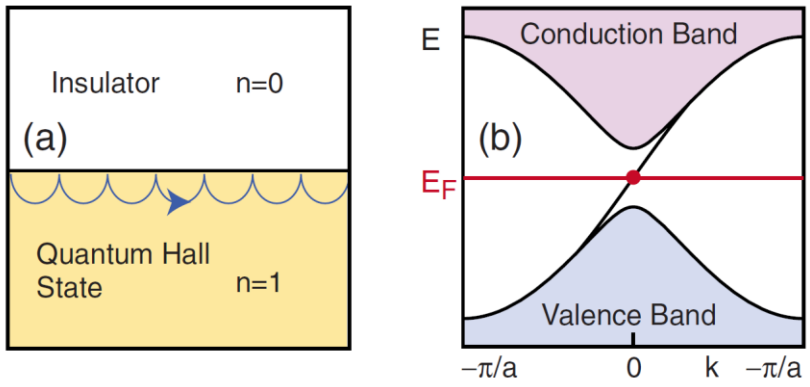

Figure 1.2: ***a)*** *Cartoon interface between n=1 QH State and n=0 vacuum with a single edge mode between them.* ***b)*** *Band structure cartoon showing a single edge mode sitting within the gap between the Valence and Conduction bands*

After the development of cleaner samples, a striking effect emerged that in conjunction to the Integer Quantum Hall Effect, the integer coming from the TKNN invariant, dramatic changes to the transport occur at fractional filling factors. This became known as the Fractional Quantum Hall Effect[17]. This effect, unlike the IQHE, is related to strong correlations between electronic states while E_F lies within partially filled Landau Levels. The resulting may particle states as described in another of Laughlin's seminal work[18] lead to various exciting properties, including fractional charge. A study of the $\nu = 5/2$ state will be discussed in more detail in Chapter 4 of this work.

1.2.2 Spin Hall and Topological Insulators

After this work, mainly in the early 2000's, physicists began looking to study a new state, a time reversal symmetric state, unlike the QHE state, that may give rise to helical edge states. This new state, the spin Hall insulator, was first proposed to be possible in graphene[19], and in other two-

dimensional semiconductors such as HgCdTe quantum wells[20,21] where the effect was shortly thereafter discovered[22].

This system has the unique property, from the point of view of the QHE, in that the edge modes present come in pairs, a consequence of the Kramers degeneracy associated with the Time Reversal Symmetry. This results in the so-called "helical" edge states, in which electrons of opposite spins are ensured to carry opposite momemta[23]. Figure 1.3a show a cartoon of these helical edge states[16].

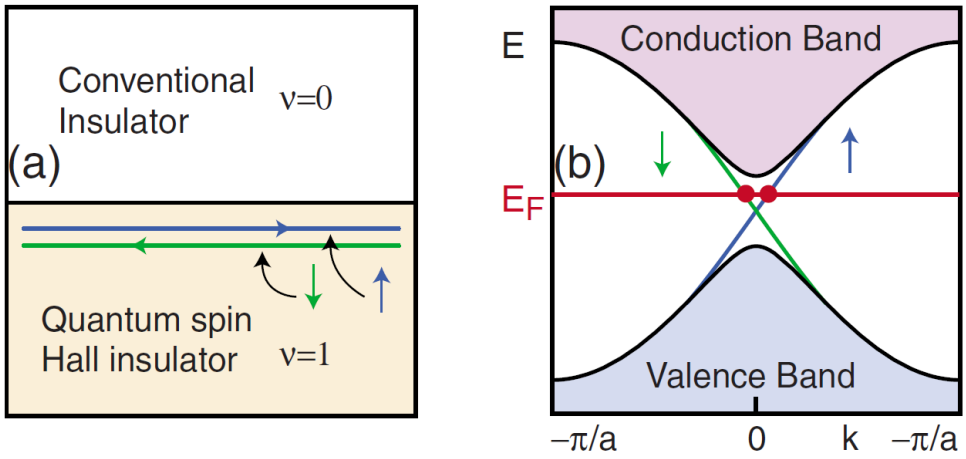

Figure 1.3 ***a)*** *Interface between a ν = 0 and ν = 1 insulator. Here we can see the emergence of the helical edge states in blue and green.* ***b)*** *Cartoon of the topologically protected states that are shown to be time reversal symmetric. This TRS is exactly why there are two protected edge modes compared to the single modes in the QHE states.*

It should be noted that due to TRS, these states are also spin-momentum locked, meaning that charges of opposite spin are confined to have opposite momenta.

An exciting revelation came with regard to the underlying nature of the spin Hall Insulator. This revelation being that there is a direct analog that can be generalized to three-dimensions[24–26]. This state can be described by a Z_2 topological invariant that can be computed in numerous ways[16], though we will focus on the description of this invariant through understanding the parity of electronic bands of interest. This relies on being able to enumerate the number of high symmetry

points in the Brillouin Zone at which band crossings exist. Band crossing must occur between bands of opposite parity, due to the band repulsion that occurs between bands of identical parity[27].

$$Z_2 = \prod_{\Gamma_i} \delta(\Gamma_i) = \begin{cases} +1 \; Conventional \; Insulator \\ -1 \; Topological \; Insulator \end{cases} \tag{18}$$

It can be shown that the Z_2 index takes on a trivial value for an even number of crossings and a non-trivial value for an odd number of band crossings, or band inversions. For cubic systems, at which there are four high symmetry points at Γ, X, M, and R, equation 18 can be reduced to[27]

$$Z_2 = \delta_\Gamma \delta_X \delta_M \delta_R \, . \tag{19}$$

This will become important in the next section where a description of a new phase of topological matter, a Topological Kondo Insulator, will be discussed.

1.3 Topological Kondo Insulators

In 2010, it was proposed that a Kondo Insulator, a well-studied strongly correlated insulator deriving its properties from the many body Kondo scattering of conduction electrons from impurity magnetic moments, could form a strongly correlated version of the Z_2 Topological Insulator. The reasons for such a proposal followed from the realization that strong spin orbit coupling (~0.5eV), relative to the rather small Kondo Gap (~5meV), responsible for the lifting of Kramers degeneracy in HgCdTe quantum wells, and likely even and odd parity band crossings may easily coexist in such physical systems[28]. Such a possibility allowed for a possible explanation of the long standing mysteries of the low temperature transport behavior in Kondo Insulator SmB_6[29,30]. SmB_6 shows an opening of a Kondo Gap, Δ~40K[31] leading to a sudden rise in resistance as temperature drops below the associated gap temperature. However, part of this anomalous behavior is easily observed

in figure 1.4, in which the thermally activated resistance increase at low temperatures gives way to a near temperature independent resistance below roughly 4K. The nature of resistance saturation in SmB_6 below 4K has led to the study of this atypical hexaboride for decades[32,33]. It had been believed that the low temperature resistance saturation in Smb_6 was caused largely by bulk impurity states. It is well known that Lanthanide elements, which possess extremely similar chemical properties, are difficult to produce in high purity[34], potentially suggesting a chemical

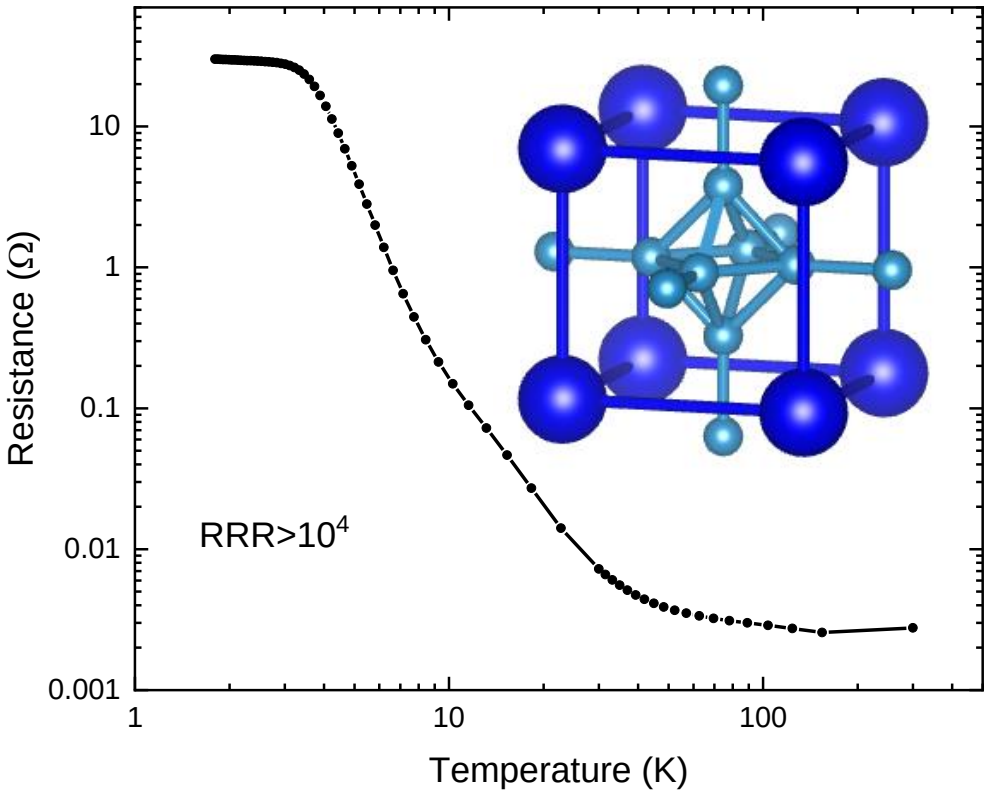

Figure 1.4: Resistance of a single crystal of aluminum flux grown SmB_6. A clear Kondo gap opens near 40K as indicative of the clear thermally activated behavior. The activated behavior gives rise to a nearly temperature independent resistance though to originate from a metallic surface state due to the vacuum/crystal interface. ***Inset*** *Ball and stick model of SmB_6 with the dark blue representing the Sm ions, and the light blue representing B. it should be noted that the boron-boron bond length within the boron cage is larger than the bond length between boron atoms spanning the Sm face. This possible dimerization has been thought to lead to the mixed valence physics in the material.*

origin of these impurities. However, as continued work was performed on the synthesis of SmB_6, and with improved sample quality, no evidence of a diminishing low temperature resistance saturation was observed[29,30,32,35,36].

1.3.1 SmB_6

During the last decade scientists began to search for evidence of topologically protected surface states that could explain the sharp departure from Kondo Insulating behavior. Evidence for such a topologically protected state came in the form of ARPES[37–39] measurements showing evidence for linearly dispersive bands near the high symmetry points, thickness independent transport properties[35,40], spin polarized transport[41], STM[42–44] and more. Calculations of the band structure show evidence of Dirac Cones at three points in the Brillouin Zone, 1 at Γ and two at X. By the parity argument in equation 19, this results in a topologically non-trivial insulator, adiabatically disconnected from vacuum.

In the span of a single year, two conflicting reports were published concerning the Fermi surface of proposed Topological Kondo Insulator SmB_6[45,46]. Quantum Oscillation experiments, which among other things can be used to probe the Fermi Surface geometry, were performed on SmB_6 to observe a Fermi Surface resulting from this two-dimensional surface state. First, a group at the University of Michigan published work that supported this two-dimensional Fermi surface picture and claimed this as evidence in support for a metallic surface state. This work had been performed on aluminum flux grown single crystals provided by our group at UC Irvine[45]. Following this result, a second QO experiment was reported on floating zone grown samples that revealed a large three-dimensional Fermi surface[46]. This Fermi surface appeared to contradict the well-known behavior of SmB_6 as a small band gap bulk insulator[33,37,47,48]. The notion that a strongly correlated

insulator could also present a bulk Fermi surface led to the development of numerous theoretical works showing that SmB_6 may host a Fermi surface of charge neutral Majorana fermions[49–51].

This charge neutral fermi surface is believed to potentially arise from the fractionalization of f-hole, separation between the charge and spin degree of freedom[50]. This leads for the formation of a composite exiton, a coupled holon and d electron, as well as a spinon. This composite exiton would as such be charge neutral but also contain a magnetic moment. This formation of a charge neutral composite fermion would lead to the formation of a chargeless Fermi surface. Furthermore, theoretical works have shown exactly how these quasiparticles couple to magnetic fields in such a way as to produce quantum oscillations, though this is non-trivial[51].

Thermal conductivity experiments, which are also adept at probing bulk excitations regardless of spin or charge, were performed by several groups with conflicting results[52,53]. Hartstein, et al. published a second work this time showing thermodynamic evidence for fermionic excitations at sufficiently high temperatures that would rule out this signature as an electronic contribution. However, these results have not been able to be reproduced[53]. In contrast an extremely comprehensive report on the thermal conductivity in SmB_6 revealed evidence for a Schottky-like anomaly resulting in a highly non-monotonic behavior of thermal conductivity with respect to magnetic field, but observe no evidence of this fermionic excitation in either flux or floating zone grown samples[52].

Around this time a group at Johns Hopkins lead by Tyrel McQueen seemed to be able to explain the exotic Mixed Valence physics that lies at the heart of SmB_6[54]. This seemed to suggest, with great success in reproducing experimental results, that the fluctuation of the valence of Sm ions was due to a slight distortion in the boron octahedral cage in which boron dimers may be pulled

from the near center of the unit cell face toward one of four Sm ions. This boron dimer proximity to a Sm ion allows for the transfer of a single electron[54].

If in fact a structural distortion lies at the heart of the bulk physics underlying SmB_6, then structural distortion may act as a powerful tuning parameter to understand the bulk behavior of this mysterious system. The power of mechanical perturbations in SmB_6 was observed in the enhancement of the surface dominated conduction temperature from 4K to nearly 240K under uniaxial strain along the <100> axis[55].

1.3.2 Oscillator Device

While the topological nature of SmB_6 was still up for debate, there was an interest in beginning to construct novel devices utilizing the proposed topological properties as well as the anomalously large self-capacitance[56,57]. A device was constructed from a small single crystal of SmB_6 placed in parallel with an external capacitor and held under a DC bias. Such a configuration lead to the observation of bias tunable voltage oscillations across the sample. Example waveforms from this device can be seen in figure 1.5a[57]. A false color SEM image in figure 1.5b highlights the simplicity of the device, though this sample is the smallest tested (due to limitations in the size of contacts and the crystal). This device was understood through a two-channel conduction model relying on a single channel with activated behavior, and the second to be nearly temperature independent. This model leads to a set of simultaneous non-linear equations that coupled the electronic and thermal degrees of freedom and predicts the voltage oscillations that were observed by Stern et al (2016).

The novelty of this device originates from its unique surface area dependence in which it was shown that the frequency of this oscillator device could be tuned over 6 orders of magnitude by a

100 times reduction in the surface area. This was believed to be direct evidence that this effect was driven by two-dimensional surface conduction available due to the topological nature of SmB_6. However, this work was incomplete as the proposed model had also predicted a set of thermal oscillations driving following the voltage oscillation. The exploration and detection of these thermal oscillations is discussed in Chapter 3 of this work[58].

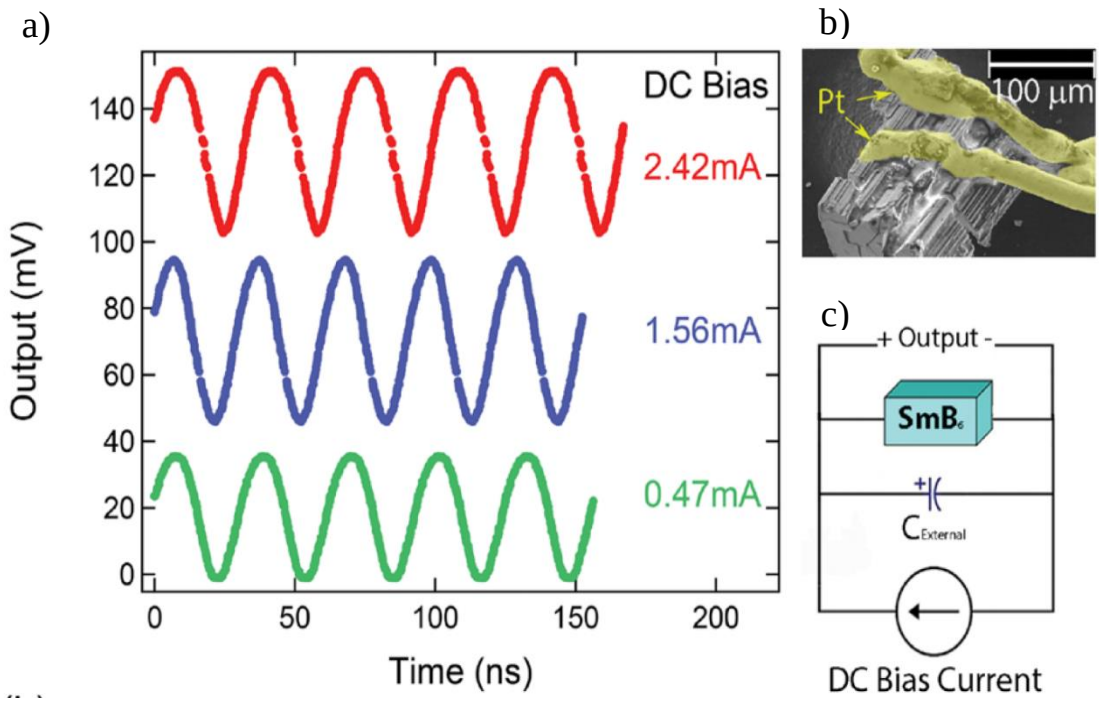

Figure 1.5: ***a)*** *Example waveforms of voltage generated from the SmB_6 single crystal oscillator. There is a well described bias current.* ***b)*** *a Scanning electron microscope image in false color showing the smallest device constructed from a microcrystal of SmB_6.* ***c)*** *Simple circuit schematic of the oscillator device, showing the external capacitor used for larger samples.*

Chapter 2

Experimental Techniques

As a Condensed Matter Experimentalist, most of the day to day work required the use of specialized cryogenic equipment and the handling of exotic materials. My interest has been in that of quantum phases of matter and in the last few years focused on topologically ordered states of matter. First this chapter will discuss the method of material synthesis performed to acquire high quality single crystals, enabling the experiments I sought to perform. Experiments in our field are only as good as the materials available to study. The use of single crystals has increased in recent decades, in part due to their availability, but also due to the interest in properties closely related to crystalline anisotropy or the material surfaces.

Experiments have been performed at exceedingly low temperatures, typically to base temperatures near 100mK. This chapter will also detail the cryostats, devices designed to perform experiments at temperatures of interest, notably below 4K. The cryostats that will be discussed are a Quantum Design Physical Properties Measurement System (PPMS) and an Oxford Dilution Refrigerator.

2.1 Crystal Growth Via Molten Flux

Single crystal growth has emerged as a crucial component to understanding the behavior of various quantum phases of matter. Devoid of scattering from grain boundaries and the well oriented nature of crystals have allowed for the in depth understanding of the physical properties of increasingly complicated phases in increasingly complicated compounds[59].

Flux growth has emerged as a highly used "Poor Man's" method of single crystal growth[59–61]. This technique relies on getting reasonably pure raw elements, tube or box furnaces, and potentially a centrifuge to aid in decanting the molten flux from the formed single crystals[61]. In contrast, Floating Zone furnaces can easily cost an order of magnitude more than the equipment required for flux growth. Synthesis of single crystals from a molten metal flux has been widely used since at least the 1960's, though the critical step of removing the crystals from the molten flux presented a challenge.

Zachary Fisk overcame complications with regard to crystal removal when he devised a method using centrifugation of the still molten flux through silica wool[61,62]. This allowed a crystal grower to now be able to remove crystals in a reasonably gentle mechanical method, as opposed to other harsh mechanical methods, or chemical leaching, which would regularly etch the crystals as much as the metallic flux they were suspended in. This centrifugation through silica wool is still widely used, though items such as fritted crucibles have become to gain popularity[59]

Flux growth utilizes a low melting point metal to dissolve raw materials into solution, known as the metallic flux. Procedurally one would have enough of the raw elements such that at sufficiently high temperatures all materials are dissolved into the molten metal to form solution. As this solution is cooled and the solubility of the dissolved elements decreases, the solution becomes supersaturated and nucleation will occur to decrease the density of solute dissolved. It is during this nucleation process that single crystals can be formed. Due to the rather slow process of nucleation, it is imperative that the solution be cooled at a sufficiently low rate, on the order of 1°C/hour. A discussion of the thermodynamics of nucleation will be discussed in some depth later in this section.

One can understand nucleation of single crystals in terms of the phenomenological construction of Classical Nucleation Theory (CNT). Though CNT was originally worked through to understand the nucleation of droplets from a vapor phase, the thermodynamic arguments presented should be directly applicable to the liquid/solid phase transformation of interest in single crystal growth[63–65]. While it is clear that within the experimental systems in question, those in which single crystals are obtained from molten flux, that nucleation occurs, it is not a given for any arbitrary metallic solution. As such, we can look closely at the thermodynamic arguments that play a role in the spontaneity of nucleation.

In considering the behavior of the free energy involved in the nucleation of a spherical nucleus, looking for a parameter space of the free energy, ΔG, becomes negative, nucleation should occur spontaneously in a manner that should allow for nucleation to continue until there is no remaining dissolved metals in solution.

$$\Delta G = \frac{-4\pi r^3}{2\nu} KT\ln(\mathrm{S}) + 4\pi r^2\sigma \qquad 1$$

An estimate of the free energy involves two terms, as seen in equation 1[66]. The first is related to the bulk of the nucleation cluster. This concerns the number of molecules within the cluster with radius r and a volume of single molecule ν. S in this context is originally defined as a vapor supersaturation ratio, though in this context we could likely consider this as to be related to the ratio of supersaturated molarity and the maximum solubility at that temperature. The second term is concerned with the energy required for the formation and stability of the 2D surface separating the nucleation cluster and the molten flux around it with σ representing the specific energy of said interface.

Figure 2.1 contains plots of both terms in ΔG, and the sum. After quick examination of this figure, it should be clear that the term accounting for the energy of the nucleation cluster should act to decrease the total free energy and would as such favor spontaneous nucleation. However, as the radius of the nucleation cluster increases, so does the free energy of that interface, increasing the Free Energy. However, it can be shown there is a maximum of ΔG at radius r_c. When the radius of the nucleus exceeds r_c, ΔG begins decreasing and crystallites with continue to nucleate out of the flux. For clusters with $r<r_c$, the stabilizing energy of nucleation formation does not compensate for the energy of the interface, and the cluster will be dissolved back into solution.

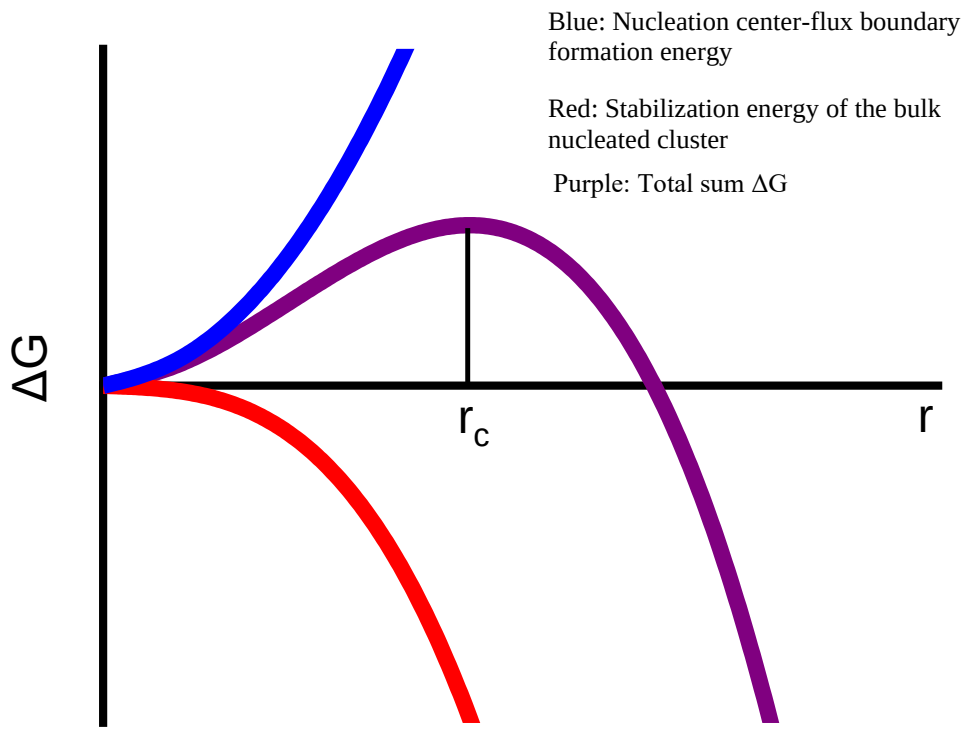

Figure 2.1: Cartoon plot of the Gibbs Free Energy as a function of the nucleated radius. The blue curve represents the surface energy. The red curve is the energy associated with the formation of a nuclear volume. The purple curve is the sum of the two. Note here that for radii greater than r_c, formation of increasing large nuclei is expected.

Unfortunately, there is still a lot of intellectual space to be covered before this more theretical discussion of nucleation can be carefully implemented to aid in crystal growth. Though this picture does allow one to understand the conditions under which nucleation and crystal growth will occur, it is not directly extendable to be used in single crystal growth. The controlling factors of single crystal growth: the concentration of elements in the solution, the temperature of the growth, and the cooling rate during nucleation, are largely parameters that are typically worked through during periods of experimental growth based largely on previous experience. Nucleation theory is an

ongoing project that Chemists and Physicists alike continue to discuss and develop quantitative methods for better insight into these processes[64].

An additional complication in this process is deciding on the correct choice of low melting point metal and proper crucible materials. Luckily after decades of work done on flux growth, there has emerged only a handful of typical metals to choose as flux, though using binary or ternary compounds as flux has been found to be exceedingly useful[59]. These metals generally include Al, Sn, Ga, Sb, Bi, Ce, etc[60,61]. With this choice of flux, finding an appropriate crucible that will not appreciably react with the molten flux at the temperatures of the intended growth is the next step. Ceramics such as alumina tend to be rather good choices, but it is also not uncommon to use high melting point and inert metals like tantalum or platinum.

Loaded crucibles would then typically be sealed in quartz ampule under vacuum or a slight inert atmosphere such as argon or nitrogen. This is usually performed to keep the pressure relatively close to atmospheric pressure during the growth process to discourage excess evaporation of constituent materials at high temperatures. For growths that exceed 1200^{o}C, it is prudent to use an ampule material other than quartz due to the softening and ultimate loss of atmospheric control, tantalum tends to be reasonably favored for these instances[59]. Other options would be to use a tube furnace that may be back filled with an inert gas, argon is my personal choice. Additionally, some flux, such as aluminum, will attack the quarts causing a similar loss of atmospheric control.

Of course, most of these considerations require extensive knowledge of material properties, and ideally a growth would be undertaken on materials that have extensive phase diagrams published. However, due to the growing complexity of certain families of crystals, such as the Cuprate and

Pnictide superconductors, these phase diagrams are almost certainly not in existence, so one must rely on partial phase diagrams and intuition developed over years of growth.

For the crystals discussed in this dissertation, an aluminum flux was chosen and loaded with stoichiometric quantities of a Rare Earth metal and boron powder. These were placed into alumina crucibles purchased from CoorsTek, the ceramic producing arm of the Coors Beer Brewery. As mentioned, aluminum attacks quartz at high temperatures so these crucibles are placed unsealed into a tube furnace which is fit with flanges designed to connect to a high purity gas cylinder and an oil pump. Air is first pumped out of the furnace after which argon is used to keep the tube at pressures higher than atmospheric pressure. If oxygen were to enter the tube, it will likely oxidize the aluminum metal at which point the flux will fail to melt at the temperatures achievable in a tube furnace, causing complete failure of the growth.

Procedurally, all REB_6 (though not all Ln will readily form hexaborides) can be grown nearly identically in which an initial rapid heating is performed to bring the crucible up to maximum temperature. This temperature is chosen to be sufficiently into the luquidus phase to allow for high kinetic energy of constituent ions to allow for diffusive mixing. This is particularly important for doped samples in which one hopes to attain homogenously doped samples. This temperature is maintained for several hours to allow for this mixing to occur. Excessively long dwell times here

would not improve crystal quality but would likely decrease the lifetime of the heating elements being used. A schematic heating and cooling cycle can be observed for YbB_6 in figure 2.2

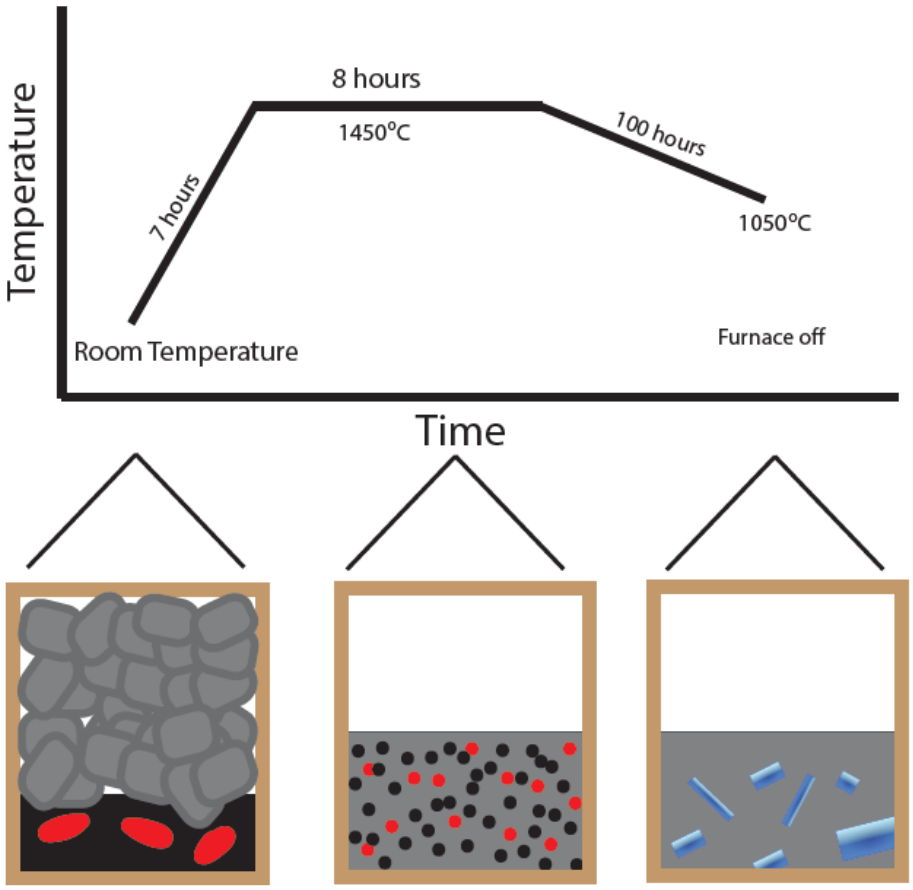

Figure 2.2: Example growth conditions of YbB_6. Her ewe can see roughly three stages of the procedure. The first in which constituent elements are loaded into the furnace at room temperature. The second, once arriving at the stable temperature maximum. At this step all elements should be dissolved into solution and mixing may occur. Third in which the slow cooling of the furnace leads to the nucleation of single crystals suspended in the aluminum flux.

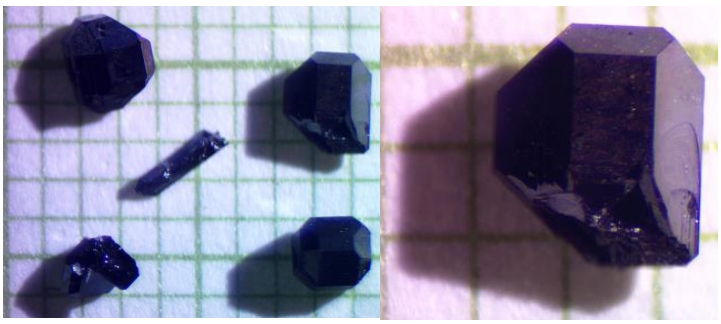

Figure 2.3: Examples of YbB_6 single crystals. These crystals have already been removed from the solid aluminum matrix via NaOH leeching.

The cooling rate and base cooling temperature are the most critical to the growth of high-quality single crystals. It is during this process that crystals will nucleate out of the solution. Unfortunately, this growth can be somewhat slow. As such cooling down slowly is critical for growing crystals of the size useful for our experiments. For REB_6 cooling down too slowly can cause the formation of quite large crystals, but ones that likely have encapsulated a large volume of molten flux. Unfortunately, this aluminum will the grow epitaxially with the crystal with a similar lattice parameter[34]. This makes finding these pockets of aluminum challenging by methods such as XRD. Looking for the diamagnetic response associated with the superconducting transition of aluminum can act as a useful screen for such inclusions if available. As such only by polishing crystals can one hope to remove all aluminum from a sample.

After heating to maximum temperatures, there is cooling period, sometimes in multiple steps, cooling at low rates as mentioned before. If the crucibles had been sealed in an ampule, the ampules may be removed from the furnace while the flux remains molten and may be loaded into a centrifuge to aid in the decanting of the flux, effectively removing all the flux from the already formed single crystals.

Our REB_6 growths were allowed instead to cool to room temperature. Once at room temperature, a high molarity solution of NaOH was used to chemically etch the aluminum metal from the crucibles leaving the crystals intact. Luckily, it does not appear that NaOH attacks these crystals, otherwise a more complicated decanting procedure would need to be employed.

2.2 Cryostats

For the study of so-called Quantum Matter, it typically becomes important that experimental materials are cooled to temperatures below that of the boiling point of liquid nitrogen (~77K). This is due in large due the fact that Quantum Phases of matter are rather fragile in that at high temperatures, phonon scattering, thermal fluctuations are large enough to "melt" the underlying order existent in these exotic phases[67].

Both SmB_6 and Quantum Hall Physics relies on temperatures that are below even 1K, requiring the use of more sophisticated cryostats than the traditional dipping probe that had been used extensively just a few decades ago.

In this section I will discuss two of the cryostats used most regularly in the work I have done in my time pursuing my Ph.D. Those include a Quantum Design Physical Properties Measurement System and an Oxford Instruments wet Dilution Refrigerator. These cryostats have base temperatures of 350mK and 30mK respectively. This means of course that for the purposes of my work that the 4K option in the PPMS and the Pulsed Tube Optical Janis cryostat are responsible largely for phases of my work that involve prototyping, as they allow for quick sample loading and high turnover rates in those experiments. In contrast the Dilution Refrigerator (DF) requires at nearly one month between successive sample changes due to the time it requires to cool samples to base temperature after the sample change and condensing helium vapor lost in the process.

2.2.1 Quantum Design Physical Properties Measurement System

Turn-key systems such as the Quantum Design Physical Properties Measurement System generally allow for high throughput measurements ideal for the characterization of many samples through standard techniques. Many common physical properties such as electrical resistivity, thermal conductivity, heat capacity, magnetic susceptibility, etc, have associated options designed and integrated by Quantum Design. One property of these systems that allows for the high rate of measurement turn-over is the standard puck design. These pucks are capable of being loaded with samples under a microscope, and place up to 12 total contacts, in the case of the standard resistivity pucks. This would allow for 3 samples to be measured in a traditional 4-probe configuration simultaneously.

However, I have focused on the use of the resistivity pucks, both for the traditional 1.8K measurement and the pucks designed for the He^3 probe due to their relatively versatile design. Using a break-out box we perform customized experiments on the aforementioned pucks that allow us to perform novel experiments, or traditional experiments that we wish to move later to other cryostats.

This makes the PPMS a workhorse in the prototyping stage of experiments, mainly the thermal conductivity experiments that will be discussed in detail later in this dissertation.

Figure 2.4: Picture of our Quantum Design PPMS fit with a CryoMech helium reliquifier allowing for extended time between liquid helium transfers.

All the work in this dissertation that was performed in the PPMS required a high degree of thermal isolation during measurements. As such it may be worth discussing the gaseous environment of the sample space as well as the method by which the puck and sample can be cooled within the cryostat.

Due to the dry environment inside the sample space, cooling is actually provided by direct thermal contact of the sample puck cold fingers, gold plated copper springs connected to the puck that make mechanical and thermal contact to the sample chamber walls. Of course, this means that that sample will only really be as cold as the sample chamber wall. The stainless-steel construction of the sample chamber walls helps to minimize the heat load on the low temperature bottom and the high temperature top of the sample space. However, cooling of the sample chamber wall relies on helium liquid that is pulled into a cooling annulus through the impedance valve at the bottom of the sample chamber assembly. Once this liquid is pulled into the cooling annulus a pump on the space lowers the vapor pressure in the annulus decreasing the temperature of the helium bath in the annulus and cooling the bottom of the sample chamber to about 1.8K.

This of course only applied for temperatures below 4.2K, the boiling point of liquid helium. For temperatures above this, helium liquid is pulled through the impedance valve and quickly boils for provide cooling. Problems in cooling at temperatures below 4.2K are traditionally associated with clogs in the impedance valve, limiting the flow of cryogen into the cooling annulus.

Now with regard to the gaseous environment in the PPMS, typical electrical transport measurements are performed under a helium vapor pressure that is typically set by the purge and seal procedure required when loading the sample that leaves a few Torr of helium vapor in the chamber. This pressure of course decreases dramatically at low temperatures as described by Gay

Lussac's Law, or maybe more generally the Ideal Gas Law. The helium pressure may be lowered further by use of a high vacuum cryopump, liquid helium cooled charcoal that is separated from the sample chamber via flapper valve that may be actuated *in situ.*

2.2.3 Dilution Refrigerator

Dilution refrigerators refer to a set of wet or dry (cryogen free) cryostats that are able to cool, for practical purposes, to about 10mK. These cryostats rely typically have a large liquid helium reserve in addition to the closed cycle dilution unit that is responsible for cooling below 2K. A picture of our CryoMech fit Oxford Dilution Refrigerator can be seen in figure 2.5.

A gaseous mixture of ^{4}He and ^{3}He is pulled from a reserve tank through a charcoal based gas trap cooled by liquid nitrogen. After initial filtering with the liquid nitrogen trap, the mixture passes through a much smaller trap cooled with liquid helium, this is stored in the dilution refrigerator helium jacket. These traps act to filter out any atmospheric gases that may have been introduced through small leaks in the close cycle tubing.

The mixture is then precooled while passing through the 1KPot. The 1KPot is a chamber in which liquid helium from the helium bath is pulled in only to be further pumped on by a mechanical pump. Adjusting a needle valve allows one to control the flow rate of liquid helium into the pot and as such effectively control the cooling power and temperature of the pot. Typically the pot is run at temperatures below 2K. After this precooling and cooling through heat exchangers the condensed mixture collects in the Mixing Chamber.

Figure 2.5 Oxford Dilution Refrigerator fit with a CryoMech helium reliquifier. The cryostat pictures here is set on a vibrationally isolated frame over a large pit which allows the helium dewar to be lowered, exposing the IVC and sample stage for use during sample changes.

Once the mixture enters the Mixing Chamber (MC), the 4He gas will undergo Bose condensation to form a superfluid. However, due to the fermionic nature of ^{3}He, such condensation cannot occur, though a fermionic condensate can be formed due to the moderate attractive potential between He^3 atoms. It is at this stage that the helium mixture will undergo phase separation due to the so-called

"forbidden region" in the phase diagram. The ^{3}He/ ^{4}He phase diagram can be seen in figure 2.6[68]. This creates two liquids, once in which all the ^{4}He superfluid and ^{3}He superfluid exist. This is called the dilute phase[68] due to the roughly 6.6% He^3 constituency. The other phase here is made of normal fluid He^3 which makes up nearly 100% of this fluid.

The cooling power from the MC comes almost entirely from the He^3 passing from the normal phase to the dilute phase. This process is highly endothermic and as such requires energy to perform. This energy is taken from the thermal energy of the environment, i.e. the sample stage. This cooling however can be shown to have a limit down to about 1mK, at which there is not enough thermal energy to continue the He^3 absorption into the dilute phase.

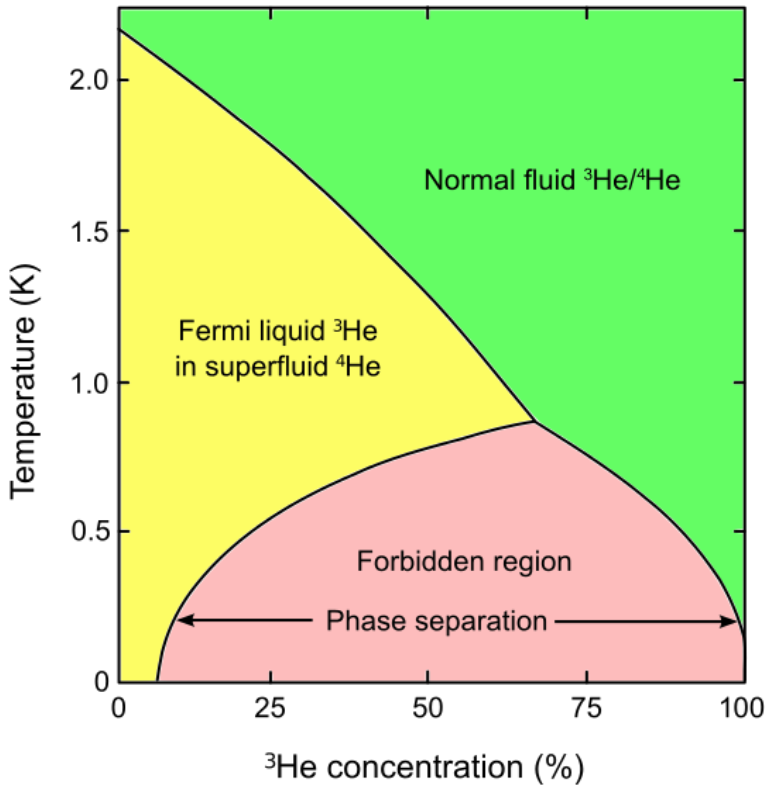

Figure 2.6: Binary phase diagram of He^4-He^3 mixture adapted from Pobel's Matter and Methods at Low Temperatures. The clear phase separation that occurs below 1K here largely drives the cooling of the Mixing Chamber allowing for temperatures down to about 10mK.

2.3 Thermal Conductivity

2.3.1 Thermal Conductivity: A Formal Treatment

I found it profoundly helpful in understanding thermal properties of materials and understanding the procedure by which thermal properties are measured to draw parallels back to electronic properties and measurements. Traditional coursework in the field of Physics tends to be rather focused on a few main topics. Of those topics Electricity and Magnetism always had the lion's share compared to thermal physics.

It is first helpful to recall Ohm's law as it is written in terms of: current density ($\vec{J}$), electrical conductivity (σ), and the electric field ($\vec{E}$). Equation 1 when making the appropriate subsitutions, integrating along a length of uniform field, allows one to arrive at the definition of electrical resistivity. In parallel, one could start with Fourier's law of heating, equation 6. Assuming that one is interested in a one-dimensional propagation of heat, the gradient can be replaced by a simple derivative, which can be approximated as the temperature difference across some length of material, l . After that approximation, a similar set of steps can allow one to arrive at a similar, yet frequently less discussed in textbooks, expression for thermal conductivity, equation 11. However, just as is the case with the electrical behavior of a material, it is the previous step that most clearly relates the quantity of interest to quantities of measurements. Equation 10 suggests that it is through the application of some power, P, into a material that a temperature gradient can be established. This is analogous to applying an electrical current and observing a potential gradient across a material. In this way one may understand that power plays the role of a current, and temperature gradient plays the role of voltage. Since we as experimentalists are generally far more accustomed

to working with electrical, instead of thermal, circuits, this analogy has proved extremely helpful in planning and designing experiments to measure thermal conductivity.

Ohm's Law		**Fourier's Law**	
$J = \sigma E$	(1)	$q = -\kappa \nabla T$	(6)
$E = \frac{V}{l}$	(2)	$q = \frac{P}{A}$	(7)
		$\nabla T \sim \frac{dT}{dx} \approx \frac{T_h - T_c}{l} = \frac{\Delta T}{l}$	(8)
$\frac{I}{A} = \frac{1}{\rho}\frac{V}{l}$	(3)	$\frac{P}{A} = -\kappa \frac{\Delta T}{l}$	(9)
$\rho = \frac{V}{I}\frac{A}{l}$	(4)	$\kappa = -\frac{P}{\Delta T}\frac{l}{A}$	(10)
$\rho = R\frac{A}{l}$	(5)	$\kappa = K\frac{l}{A}$	(11)

This can help one to better understand and plan for experiments involving non-standard thermal conductivity geometries. It is also rather helpful in understanding the role of different materials play in the leaking of heat to external parts of the experiment. As shown in Chapter 5, it can be useful to come back to the analogy to electrical circuits for exactly this reason.

A more formal derivation of thermal conductivity can be produced from the consideration of a heat current $\vec{h}$, equation 11, carried by all phonon modes. This derivation is reproduced from "Thermal Conduction in Solids" by Berman[69].

$$\vec{h} = \sum N(q)\hbar\omega\overrightarrow{v_g}(q) \tag{11}$$

At thermal equilibrium, N(q) = N(-q) and $\omega(q) = \omega(-q)$, where N(q) and ω(q) are the phonon number density and phonon frequency, respectively, suggesting that a heat current in a system in thermal equilibrium must be 0. A heat current therefore requires the phonon population to depart from equilibrium such that N(q) does not exactly cancel with N(-q).

For example, take a sample in which a temperature gradient can be generated along the z-axis such that phonons move solely in this direction. The rate of change of the number density of phonons after some time t can be found to be in the form of equation 12. Notation marking the momenta q and the polarization are omitted, though this relationship should hold for all modes. The final equality in equation 12 is valid for a full 3-dimensional treatment.

$$\left(\frac{\partial N}{\partial t}\right)_{dr_ift} = v_g\frac{\partial N}{\partial z} = -v_g\frac{\partial N}{\partial T}\frac{\partial T}{\partial z} = \left(-\overrightarrow{v_g}\cdot\overrightarrow{\nabla T}\right)\frac{\partial N}{\partial T} \tag{12}$$

As is true for all thermal transport in this dissertation, I will focus (as Berman does) on a steady state solution in which the rate of change of the phonon distribution due to phonon drift is equal to that caused by scattering, Equation (13).

$$\left(\frac{\partial N}{\partial t}\right)_{drift} + \left(\frac{\partial N}{\partial t}\right)_{scatter} = 0 \tag{13}$$

Considering the relaxation–time method, we can rewrite the scattering portion of the density change in terms of the deviation from the equilibrium distribution N^0 and the scattering time, τ as shown in equation 15.

$$N^0 = \frac{1}{e^{\frac{\hbar\omega}{k_B T}} - 1} \tag{14}$$

$$\left(\frac{\partial N}{\partial t}\right)_{scatter} = \frac{N^0 - N}{\tau} \tag{15}$$

Using the standard procedure in solving the Bolzmann equation, we assumed that ($\delta N/\delta T$) in equation 12 can be replaced by ($\delta N^0/\delta T$), meaning the distribution is assumed to only weakly deviate from the equilibrium distribution. Making this substitution and equating equations 12 and 15, we arrive at an equation 16.

$$v_g^z \frac{\partial N^0}{\partial T}\frac{\partial T}{\partial z} = \frac{N^0 - N}{\tau} \tag{16}$$

Since, as mentioned before, heat flow is concerned only with the deviation from equilibrium we can solve equation 16 for N and substitute back into equation (11) to arrive at an expression for heat flow as follows:

$$h = \sum \hbar\omega \left(v_g^z\right)^2 \tau \frac{\partial N^0}{\partial T}\frac{\partial T}{\partial z}. \tag{17}$$

Recalling that thermal conductivity, κ(T), can be calculated from the quotient of heat current and thermal gradient, as in Equation (10), we can now arrive at an expression of thermal conductivity from the Boltzmann formulation in Equation (18).

$$\kappa = \frac{-h}{\left(\frac{\partial T}{\partial z}\right)} = \sum \hbar\omega\left(v_g^z\right)^2 \tau \frac{\partial N^0}{\partial T} \tag{18}$$

We note here that this value can be calculated fairly easily given a background in the Statistical Mechanics of a free Bose gas. A detailed description of evaluating this integral is given in Berman (page 22)[69], and more generally in Pathria (page 181)[3]. Rewriting the summation to an integral over all modes, ω, can be made by including the density of states within ω and ω + dω as can be seen in Equation (19).

$$\kappa = \int_0^{\omega_{max}} \hbar\omega v_g^2 \, \tau f(\omega) \frac{\partial N^0}{\partial T} d\omega \tag{19}$$

Making all appropriate substitutions into Equation (19) yields Equation (20), a rather cumbersome integral. It is here I would recommend consulting Pathria for details on performing this integral with proper variable substitutions for x and ω_{max} as can be seen in equations (21). These substitutions lead to a more standard form in Equation (21)

$$\kappa = \frac{1}{2\pi^2 v} \int_0^{\omega_{max}} \hbar\omega^3 \tau \frac{(\hbar\omega/k_b T^2) e^{\frac{\hbar\omega}{k_b T}}}{\left(e^{\frac{\hbar\omega}{k_b T}} - 1\right)^2} d\omega \tag{20}$$

$$x = \frac{\hbar\omega}{k_b T}, \omega_{max} = \theta \frac{k_b}{\hbar} \tag{21}$$

$$\kappa = \frac{k_b}{2\pi^2 v}\left(\frac{k_b}{\hbar}\right)^3 T^3 \int_0^{\frac{\theta}{T}} \tau(x) \frac{x^4 e^x}{(e^x - 1)^2} dx \tag{22}$$

For the purposes of this discussion, one could stop here noting that the definite integral will only yield an extra multiplicative factor to T^3. The important point here is that a phonon gas is expected to contribute to thermal conductivity in a way that is cubic in temperature in the limit in which N is small enough to exclude phonon – phonon scattering and provided the generated temperature gradients are small.

$$C(x)\, dx = \frac{3k_b}{2\pi^2 v}\left(\frac{k_b}{\hbar}\right)^3 T^3 \frac{x^4 e^x}{(e^x - 1)^2} dx \tag{23}$$

However, it may be useful to note that the differential heat capacity can be calculated as such from equation 23 which allows one to directly relate the thermal conductivity with the heat capacity of a non-metallic material as seen in equation 24. Here, τ(x) is relaxation time, but l(x) is the phonon mean free path.

$$\kappa = \frac{1}{3} v^2 \int_0^{\frac{\theta}{T}} \tau(x) C(x) dx = \frac{1}{3} v \int_0^{\frac{\theta}{T}} l(x) C(x) dx \tag{24}$$

$$\kappa_{phonon} \sim \beta T^3 \tag{25}$$

It is useful to note here that at sufficiently low temperatures, small samples, with dimensions on the order of millimeters may have cross sectional areas that are comparable to the mean free path, allowing for a straight-forward estimate that even I can perform.

This estimate related the mean free path, temperature independent, to be[52]:

$$l_0 = 2\sqrt{\frac{A}{\pi}}. \tag{26}$$

This estimate will be used in Chapter 5 when trying to compare the thermal conductivity below 1K of Topological Mixed Valence Insulator, SmB_6 to that of a free phonon gas.

2.3.2 Thermal Conductivity: A Practical Discussion

First, it is important to choose materials that should help to 1) isolate the experiment from the surrounding environment, and 2) to ensure strong thermal contact between individual components of the experiment. As such, it is critically important to perform such measurements in a high vacuum environment and with all contacts directly to the cold stage (with the exception of the thermal grounding wire) to be thermally insulating. Both of these considerations help to eliminate parasitic heat loss to the environment.

Single crystalline samples, typically either plate or needle shaped are chosen to ensure the geometric factor L/A can be easily measured with a low degree of systematic errors. In fact, this parameter is frequently cited as the largest source of systematic error in these experiments.

Procedurally, thermal conductivity experiments are designed as follows: a small crystal has four contacts made to the surface. One contact is reserved for contact to an ohmic heater, two are used for contacts to two separate thermometers, and the final contact is used to make contact to the thermal ground of the experiment, usually strong thermal contact to the cryostat stage or mixing Chamber. This set up allows for a steady state temperature gradient to be generated lengthwise along the crystal which should be large enough to measure with the appropriate thermometer.

Contacts are typically made with platinum, or silver wires due to their superb thermal conductivity at relevant temperatures. Creating contacts with a low contact resistance is imperative for high sensitivity measurements. One can use the Weideman-Franz law to estimate the thermal conductivity of a contact from the contact resistance. Typically, silver epoxy or solder is used to make electrical and thermal contacts between the sample and transport components. Depositing an inert metallic layer, such as gold, can create a surface that is able to be soldered to directly, generally ensuring low contact resistance.

Thermometers for these experiments are typically ruthenium oxide, RuO_2, or ROX films mounted on a thick alumina substrate. Details of these thermometers can be found in Chapter 3 in discussion of the measurement of thermal oscillations in SmB_6. These thermometers are chosen due to their high degree of sensitivity at cryogenic temperatures, typically below 1K and as low as a few mK, where variable range hopping causes a sever loss of sensitivity[68]. These thermometers, however, need to be thermally treated before their use in experiment. Due to some internal stresses of the film that are generated in the deposition onto the alumina substrate, there is a significant hysteretic behavior to the electrical resistance with temperature. To relieve this stress one can sequentially cool the thermometers and allow them to warm back to room temperature. This can be done up to 50 times to ensure the highest degree of resistance reproducibility. Due to the sensitivity of these

films to temperature, we choose to make contacts to these thermometers via electrically conductive epoxy.

A thin silver foil is mounted to the thermometers with a spot of indium at the end. This indium can be solder very quickly at low temperatures to make contact to the silver or platinum wires connected to the sample surface. Care must be taken during this process not to allow the thermometers to heat up. This can result in a complete destruction of the thermometer.

Measurements are performed in the standard steady-state method in which the heater excitation is stepped up with a time interval between steps long enough for complete thermalization of the sample while allowing for a period of stability that data can be overaged over to increase resolution. I found it most helpful to perform all measurements with the cryostat set to its base temperature. This should allow for the cryostat cooling power to vary only slightly. I found that, particularly in the PPMS, that the system automation controlling the cooling power could be quite troublesome with regard to obtaining high quality data.

While the heater excitation is stable, the resistance of the ROX thermometers is measured using Lock-In amplifiers. The measured resistances are then checked against a calibration curve collected for both thermometers upon cooling from room temperature. Due to the hysteretic (though slight) nature of these thermometers, the *in situ* calibration is critical. The conversion to temperature from resistance can be performed wither by calculation from various fitting parameter extracted from a logarithmic power series[68], or through my preferred method, cubic spline interpolation. After this conversion, calculating the thermal gradient ΔT, in equation 10, and the calculation of the heater excitation, P, lead to a trivial calculation of thermal conductivity κ, which is usually plotted against the average temperature between the thermometer contacts.

Chapter 3

Direct observation of surface-state thermal oscillations in SmB_6 oscillators

This chapter is based on Casas, et al. (2018)[58]

This work sought to resolve open questions regarding the construction of a novel device based on candidate Topological Kondo Insulator, SmB_6. A device had been constructed from a small single crystal of SmB_6 placed in parallel with an external capacitor, the value of which was variable based on the dimensions of the crystal in use. This device, when placed under a modest DC bias, produced a highly periodic waveform in voltage. The remarkable property of this device was the massive frequency space tuning available by varying the size of the single crystal. It had been

observed that these oscillation frequencies could be tuned over six orders of magnitude up to about 50MHz.[57]

The first works published on this device suggested a model in which a cycle of self-heating due Joule heating on the high resistance surface gave rise to an increase in bulk temperature in which the Joule heating would be minimized. During this cycle, energy could be stored and then released back into the crystal via the capacitor. The work as described in this chapter sought to verify this cycle of Joule heating as a driving mechanism for these voltage oscillations.[57] Understanding the underlying mechanism for this device could better lead to the development of these devices on industrial scales for use as cryogenic voltage oscillators.

3.1 Introduction

Samarium hexaboride (SmB_6),a strongly correlated mixed valence compound[32,33],has garnered much attention recently due to the discovery of a low-temperature conducting surface state[35,40,45,47,56,70].It is proposed to form a strongly interacting version of a topological insulator[27,28,71–73],with a Kondo gap in the bulk and a gapless state on the surface that seems to be protected by time-reversal symmetry[40]. The lack of impurity conduction in the bulk has allowed the realization of a radio frequency oscillator device [57] based on SmB_6 microcrystals, where a small DC current drives the SmB_6 crystal into an oscillating state and generates large oscillating voltages. This behavior was explained by a theoretical model [57], which utilized a coupling between two conduction channels, namely metallic surface conduction and thermally activated bulk conduction, which result in significant differences in sample heating under an applied current. While this paper will focus on the verification of this model in a proposed topological Kondo insulator, a general

semiconducting sample with metallic channels with electrical and thermal coupling can be described equally well. The proposed model can be written as follows:

$$CR_s\dot{I}_s = I_0 - GI_s$$

$$C_H\dot{T} = 2I_s^2R_sG - I_sI_0R_s - \gamma(T - T_b) \quad (1)$$

Here I_S and I_0 are the surface and applied currents through the sample, respectively; C is the total capacitance representing the combined internal and external capacitance; and $G = \frac{(R_S+R_B)}{R_B}$,

where R_S is the surface resistance and $R_B = R_B^0 e^{\left[-\frac{\Delta}{T}+\frac{\Delta}{T_0}\right]}$ is the bulk resistance. R^0_B is bulk resistance in equilibrium at temperature T_0. C^0_H is the heat capacity and γ is a temperature-independent heat transfer rate through external leads.

Solving this simultaneous set of equations yields oscillatory solutions of both temperature and crystal voltage, which has a constant phase shift of 90°. Qualitatively, one can understand the production of thermal and voltage oscillations as arising from alternating the dominating conduction channels between surface- and bulk-dominated conduction. Due to the Joule heating that occurs while surface conduction dominates, the crystal may heat locally enough to enter a lower resistance bulk-dominated state. It is in this state that Joule heating is reduced; the sample temperature will equilibrate back toward that of the measurement stage and thus drive the sample back to surface-dominated conduction. This model gives predictions of oscillating voltages that agree with experiments.

The verification of this model is crucial for the search and development of novel materials and structures that can be used to improve existing oscillator technology and to realize reliable, stable, high-frequency oscillation devices. Since the design of a higher-frequency oscillator up to THz [57] relies on the validity of the above model, it is vitally important to verify experimentally the other key component of the model, namely the oscillating surface temperature. The difficulty in observing these thermal oscillations is multifaceted. Primarily, the magnitude of the temperature oscillations is predicted to be small, on the order of 1 K. Secondly, the thermometer needs to be small enough to measure the surface state. Additionally, due to the frequencies of the thermal oscillations, the measurement method needs to be able to equilibrate to the surface temperature quickly so as not to introduce a significant contribution to a phase shift between voltage and thermal oscillations. Here we have overcome these challenges with a RuO_2 microthermometer and fast data-acquisition methods.

3.2 Experimental Methods

The studied devices were constructed of a single crystal of SmB_6, held at 2K in a cryostat under no applied field, in parallel with an external capacitor stored at room temperature outside of the cryostat. A detailed schematic of this device can be seen in Figure 3.1(a). The crystal used in these experiments is roughly 1×0.8×2.7 mm. The crystal of this size was chosen due to the desire to measure low-frequency thermal oscillations, which have been shown to arise only in large single crystals [57]. Single crystals of SmB_6 were grown using an aluminum flux method described in previous work [35].

Thermometry was performed via four-probe resistance measurements of a RuO_2 thermometer mounted to a single surface of the studied crystal via thermally conducting varnish separated by a

thin electrically insulating layer. The Vishay RuO_2 thermometer, as depicted in Figure 3.1(b), is primarily constructed from an alumina substrate with electrodes capping two ends that allow for electrical contact with the RuO_2 film, which is protected by a thin epoxy layer. Due to the thick substrate sitting below the film resistor, the thermometer is mounted to the crystal such that the epoxy layer is in closest contact. Though the entire thermometer has a size on the order of that of the crystal, the RuO_2 film is only 0.80×1.15× 0.020 mm. RuO_2 was chosen as it has a high sensitivity in the vicinity of the transition of SmB_6 between bulk-dominated and surface-dominated conduction, a crucial transition for the generation of an oscillatory output voltage. In this regard, we expect the thermometer to be quite sensitive to small changes in sample temperature. Four Manganin wires soldered to the thermometer were used as electrical contacts by which a small 1 μA current was applied and a voltage measured. Manganin wires were chosen as they are poor thermal conductors at low temperatures, ensuring the thermometer is maximally thermally isolated from the thermal bath.

Thermal measurements were performed via the four-probe method as described previously. The change in thermometer resistance was used in comparison with the temperature dependent resistance data taken upon cooling the thermometer to 2 K, as seen in Figure 3.1(b), in order to infer a thermometer temperature. Due to the requirement for temporally sensitive measurements of the thermometer temperature, it was of interest first to test the response time and magnitude of the thermometer junction. It is believed that a small thermal lag could be presented due to the heat transfer through the interfacial varnish and insulating layer.

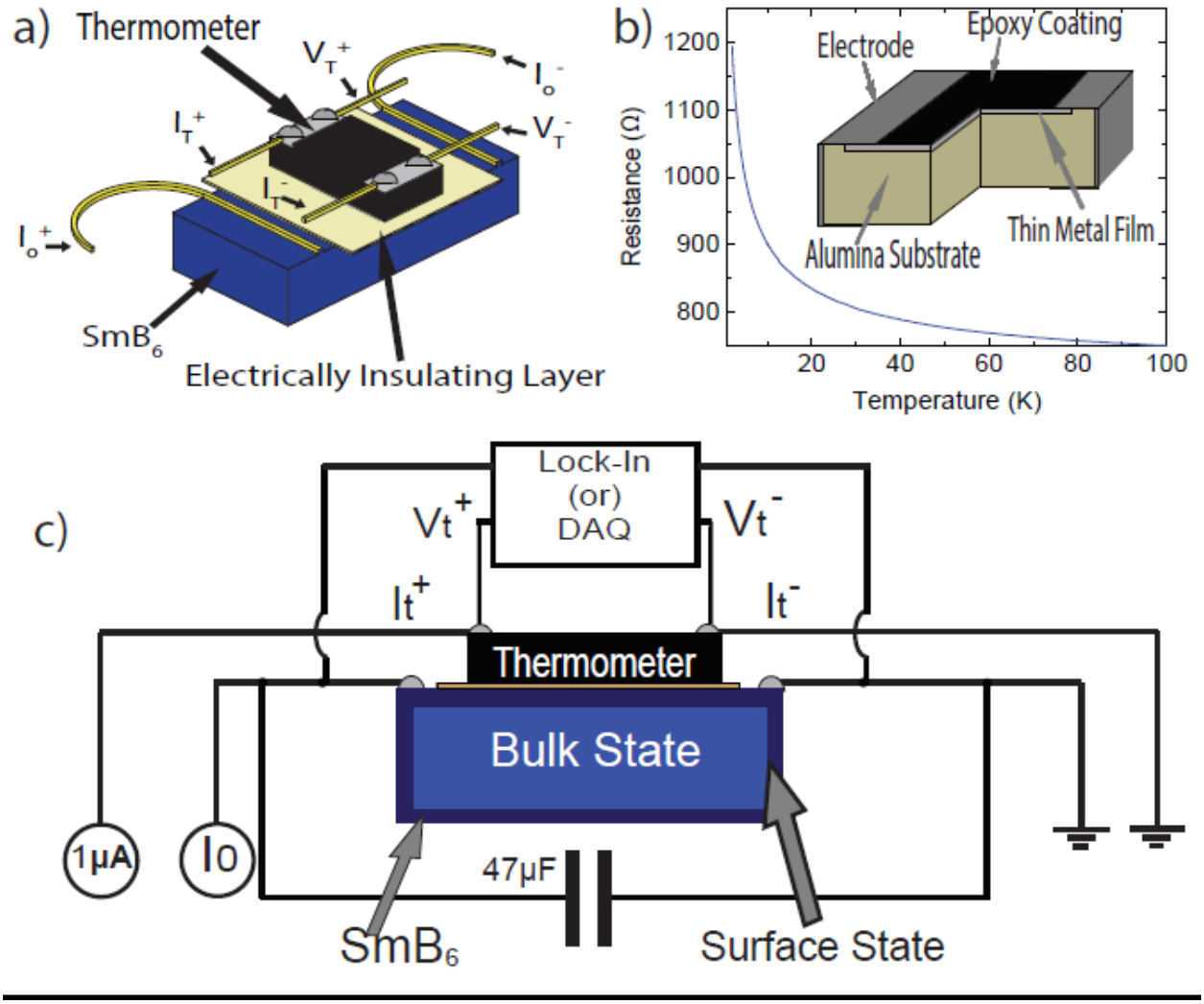

Figure 3.1: ***a)****, A RuO2 micro-thermometer is affixed via varnish to a thin electrically insulating layer on top of SmB6.* ***b),*** *Thermometer temperature dependent resistance insert construction of RuO2 thermometer* ***c),*** *Device measurement schematic in which either a Lock-In amplifier measures the thermometer voltage or a DAQ 9824.*

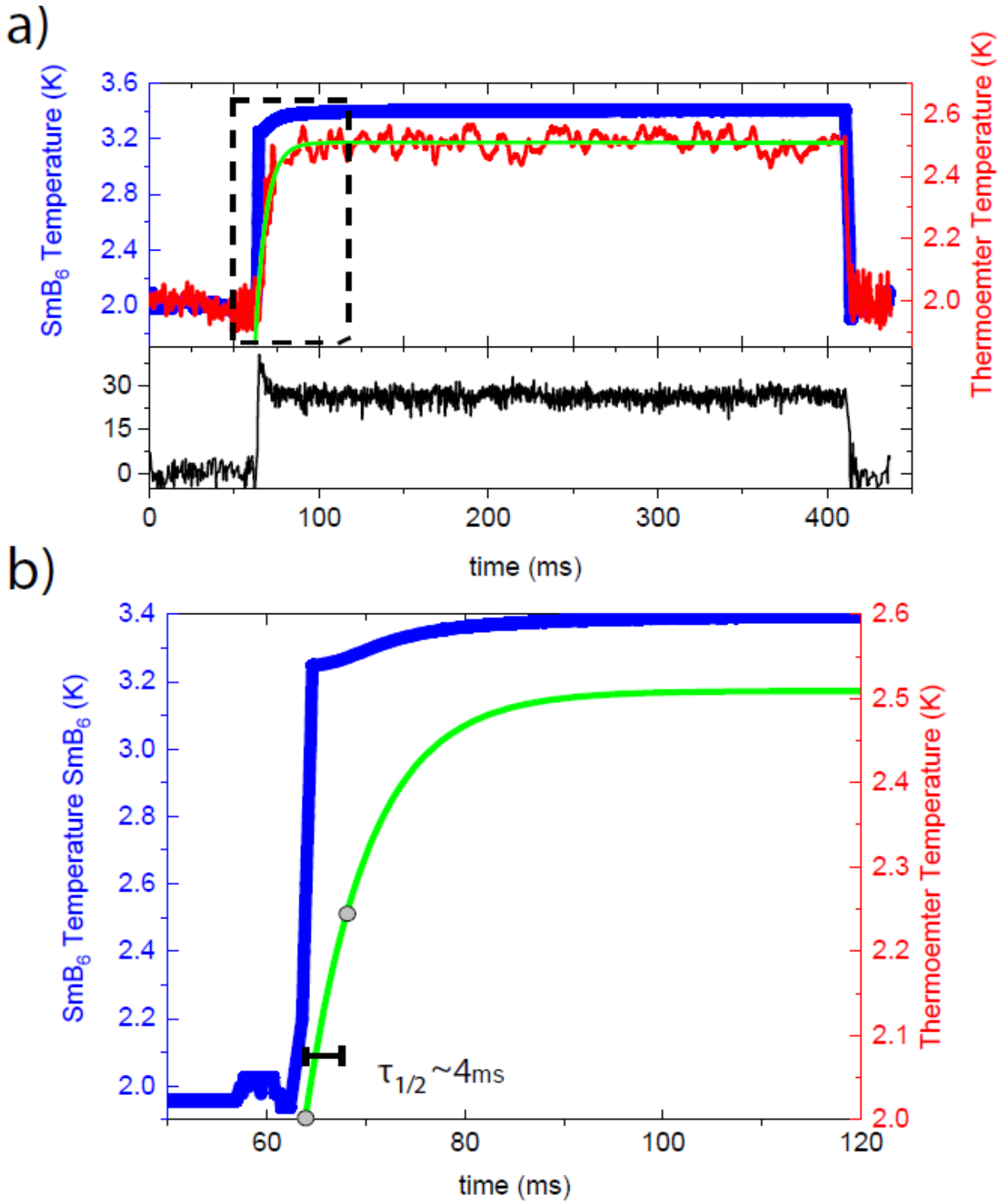

Figure3.2: ***a),*** *Response of SmB_6 crystal (blue) and RuO_2 thermometer (red) to a square wave of current. The thermometer response was fit to an exponential function plotted in green Shown in black is the percent difference between the crystal temperature and the thermometer temperature showing a peak when the current is applied that settles to roughly 25%.* ***b),*** *Enlargement of the boxed region in panel a showing the fitting curve and the crystal response which reaches one half of its equilibrium temperature in 5ms.*

Testing this response was performed by measuring the voltages across the crystal and thermometer during which a small excitation current is switched on quickly to the crystal causing Joule heating. From these data, both the crystal temperature and the thermometer temperature were calculated using their respective temperature-dependent resistance curves. This data as shown in Figure 3.2(a) show a delay time for the thermometer below a measurable time window(<0.2ms).This short delay time suggests that no substantial phase shift should be introduced by the experimental design, thus allowing for reliable time-dependent measurements within the frequency range studied. However, the time for equilibration of the thermometer temperature does lag that of the crystal. In fact, half of the overall change in temperature occurs in roughly 4 ms, as shown in Figure 3.2(b) [an enlargement of the boxed region in Figure 3.2(a)]. The 5 ms scale appears to be due in part to the slow equilibration of the crystal shortly after the current is quickly turned on, as shown by the gradual rise in temperature from 3.2 to 3.4 K over the scale of roughly 10ms. As such, we do not expect the thermometry to contribute substantially to any phase shift between the voltage oscillations and thermal oscillations, which should have a roughly constant relative phase of 90^{o}. Furthermore, at temperature saturation there is a difference in the temperatures between the crystal and the thermometer, which can be seen in black in Figure 3.2(a). The saturation difference of roughly 25% was used to scale all measured thermometer temperatures to scale up to an estimated crystal temperature. It is thought that only a portion of the heat generated by Joule heating of SmB_6 successfully transfers to the thermometer, as some is lost to the insulating layer as well as through the Pt leads to the thermal bath contact to the crystal.

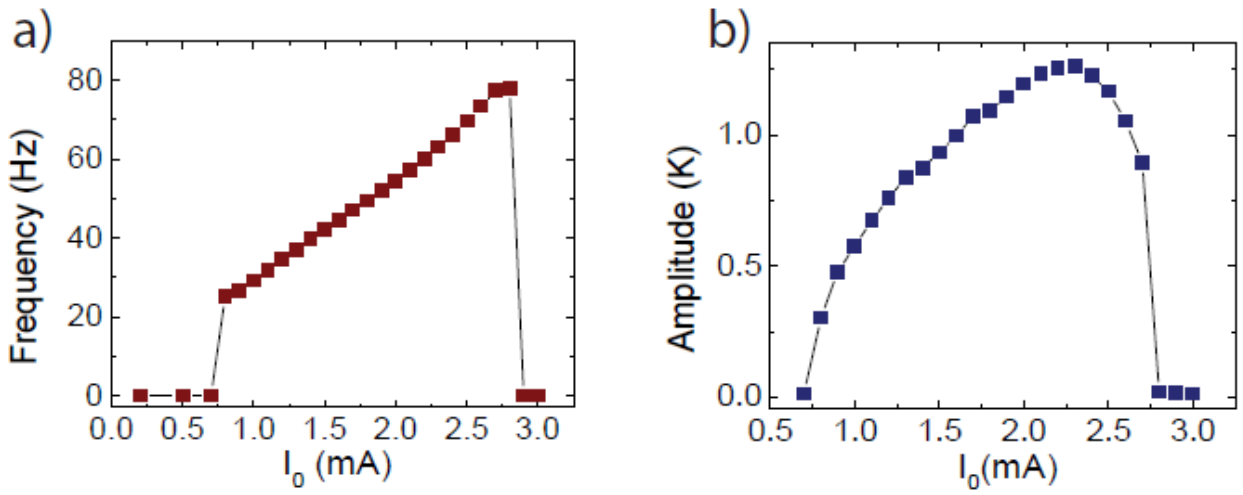

Figure 3.3: ***a),*** *As measured a Lock-In amplifier, the frequency of thermal oscillations of the* $_6$ *crystal as a function of applied DC bias.* ***b),*** *Amplitude of thermal oscillations of* SmB_6 *crystals as a function of DC bias. The sudden decrease in frequency and amplitude agree with previous simulations. This is in agreement that there is a bounded region of parameter space within which these oscillations will be stable.*

3.3 Signal Processing

Using the measurement scheme depicted in Figure 3.1(c) using the lock-in amplifier, the measurement of the thermal oscillation frequency and amplitude can be carried out reliably, due in large part to the rapid temperature response from the thermometer, as previously discussed. In this measurement design, the oscillatory voltage generated from the crystal under small dc bias is used as a reference signal for the measurement of the thermal oscillations. The data collected for the frequency and amplitude of these oscillations are shown in Figures 3.3(a) and 3.3(b). We note that the surface temperature oscillation is less than 1.5 K, which agrees with our expectation. These data also behave consistently with simulations from previous works[57]. This method, however, lacks temporal resolution to observe thermal oscillation waveforms directly, requiring rapid data collection.

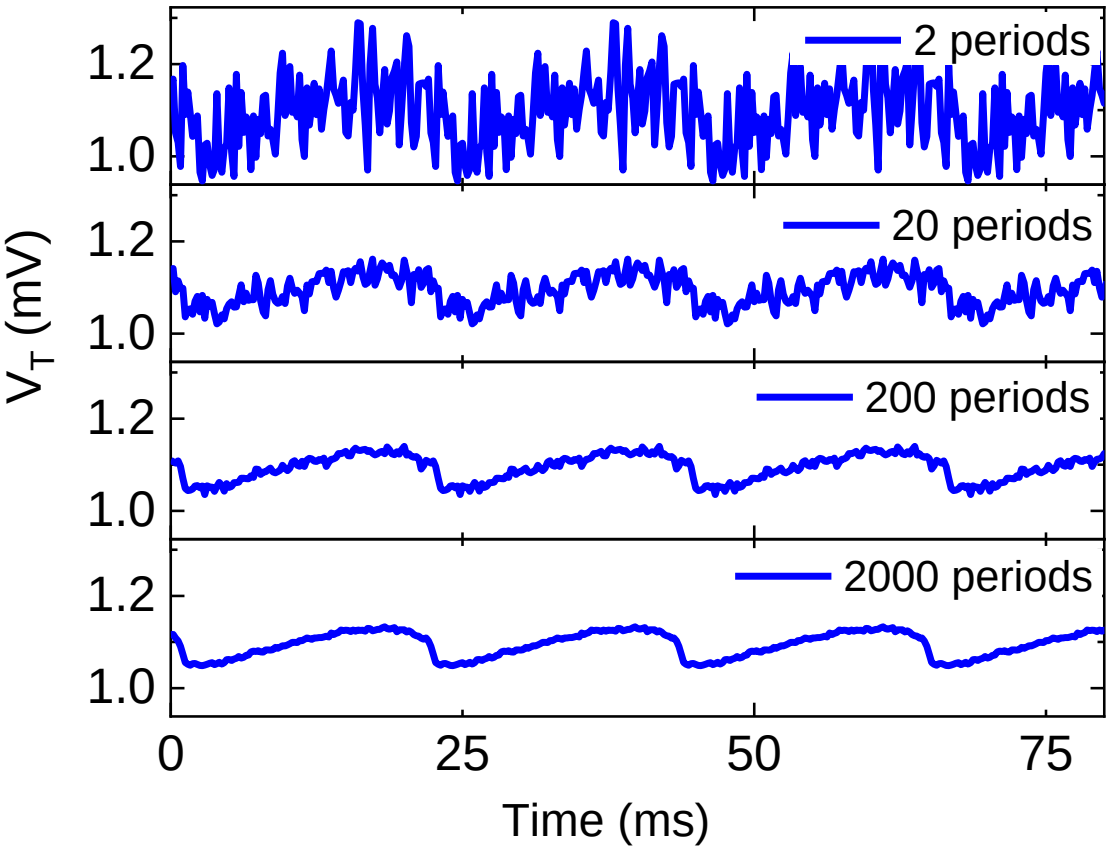

Figure 3.4: DAQ data after increased signal processing. The number of periods over which data was averaged increases downward from 2 to 2000.Data here, for the sake of presentation is a single period duplicated three times to form a cohesive waveform. All data regarding the frequency and amplitude of the physical waves is calculated from raw data, so this duplication procedure should be of no consequence.

A direct recording of the exact waveforms of thermal oscillation requires fast acquisition instruments such as a digital acquisition device (DAQ). However, due to the lack of signal-to-noise amplification that is present in a lock-in amplifier, thousands of periods of data must be collected to enable manual signal processing to observe signals with a low signal-to-noise ratio. A 9824 DAQ card was used to simultaneously measure the crystal oscillation voltage and thermometer voltage. For clarity, we label all voltages and currents applied or measured from the thermometer as Vt and It, while the crystal voltage and applied current are written as V_o and I_o,

respectively. All measured quantities are labeled in Figure 3.1(a) on an illustration of the previously described device. We constructed the measurement scheme as depicted in Figure 3.1(c) in which all measurements were performed using the DAQ, which had a maximum measuring frequency of 4800Hz, which was set constant through all measurements. The DAQ was well suited for these measurements due to its voltage resolution of roughly 1 μV. This method has the benefit of measuring both crystal voltage and thermometer voltage simultaneously, which allowed for the signal processing described in detail in this paper. The DAQ was used to measure the voltages across both the thermometer and the sample, which was placed in parallel to a 47μF capacitor that was held at room temperature outside the cryostat. A Keithley 6200 Precision Current Source applied a 1μA of DC current to the thermometer to prevent self-heating. This requisite small probing current resulted in a fairly low signal-to-noise ratio, making identification of the oscillatory voltage challenging. In using the DAQ to simultaneously measure the crystal voltage and the thermometer voltage, V_t, we were able to use Vo as a trigger for the measurement of V_t. In this way, the signal processing, i.e., averaging over thousands of periods of the data, was able to be performed without knowing the positions of the periods of thermal oscillation. As predicted, the relative phase between thermal and voltage oscillations should constantly be 90^0.

Signal processing involves three steps. First a custom script locates minima and maxima in the crystal voltage data Vo. Using these times, the data are separated into individual periods over which averaging will be performed. This averaging was typically performed over upwards of 2000 periods, though the exact number varied depending on the length of time over which data were collected. All crystal voltage data presented here are raw data, although most thermometer voltage data and temperature data have undergone this processing. The results of such processing can be

seen in Figure 3.4, in which the periods averaged over increase from 2 periods to 2000 periods moving down the figure.

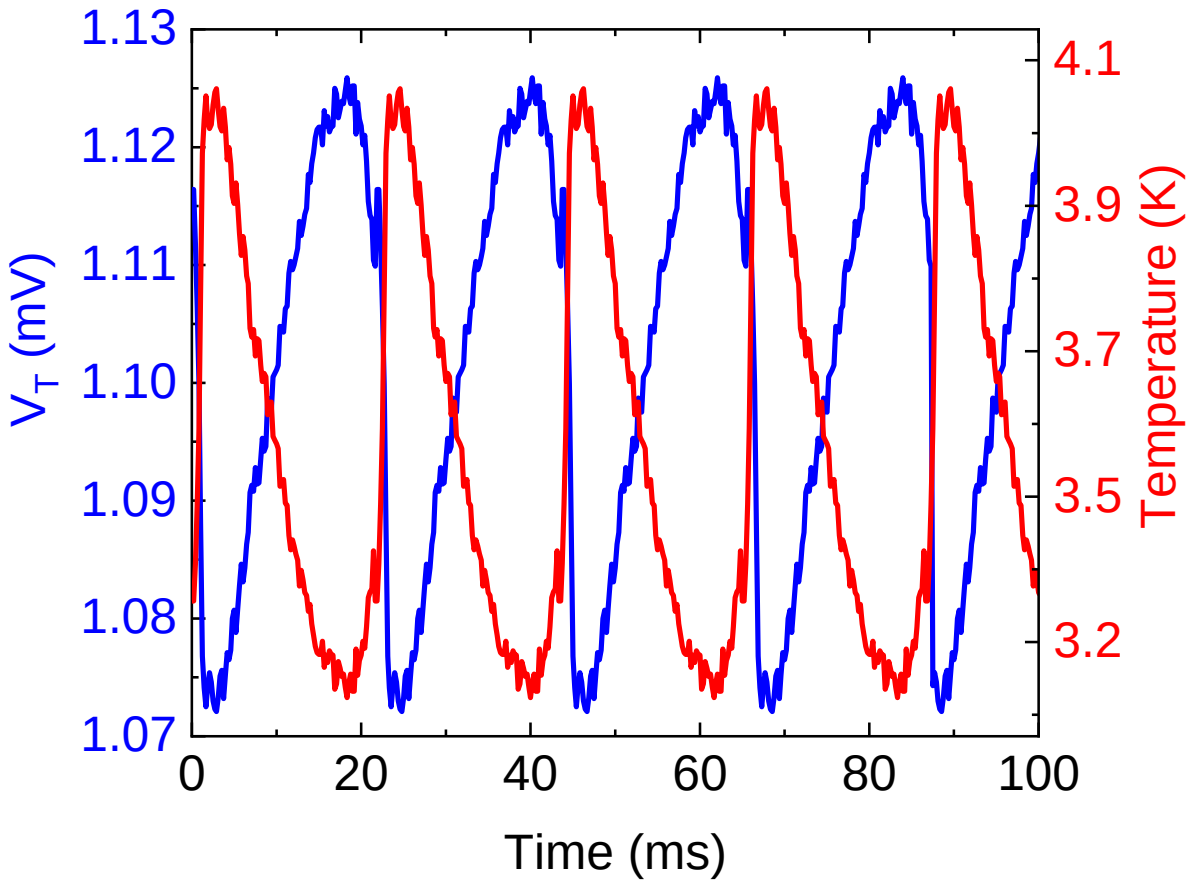

Figure3.5: Raw V_T data in blue and refined temperature oscillations in red all for sample with a 1.9mA bias. Processed V_t data and RuO_2 resistance data were used to create temperature oscillation data. As mentioned in figure 3.4, this figure shows a single averaged period that has been duplicated to show a complete waveform. The conversion here from voltage to temperature was performed via cubic spline interpolation against the thermometer calibration data collected upon each cooldown.

The final result of the processing and temperature conversion can be seen in Figure 3.5. After completing the processing, the data may be used to compare to the model as described previously. The processed thermal oscillation data and voltage oscillations data can be found in Figure 3.6. Note that these have been plotted in comparison to curves generated by solving the proposed model

in Eqs. (1), which are in good agreement with the data taken via DAQ with I_0 =1.9 mA. Due to the simplicity of the proposed model, it is not surprising to observe some deviation in the waveform shapes between the model and the experimental data.

3.4 Comparison to Model

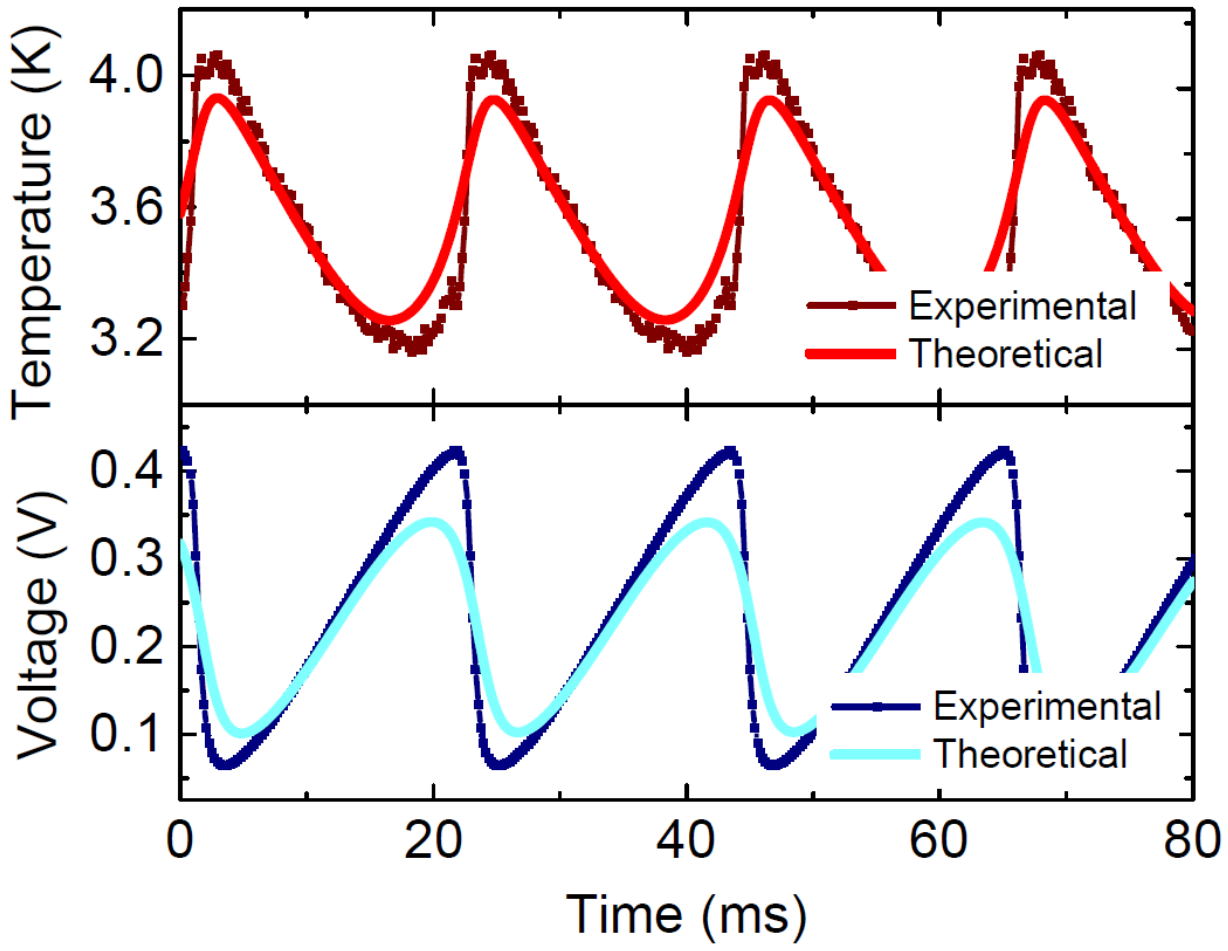

Figure 3.6: Comparing experimentally obtained temperature waveform with theoretical prediction. Temperature and crystal voltage oscillations plotted as red and blue connected points. Note that as predicted, these waves appear to be roughly 90 degrees out of phase. Solid curves in red and blue represent data produced by the aforementioned nonlinear model using specific sample parameters.

The theoretical model and its regime diagram have been discussed in detail in our previous paper [57]. Here we briefly outline fitting of the current and temperature time dependencies, presented in Figure 3.6. The model has four dimensionless controlling parameters, and it's fitting is not straightforward. Two of them $\delta = \Delta/T_B \approx 19$ and $\rho = R^0_B/R_S \approx 35$ can be calculated directly since R_S, R^0_B, and T_B have been measured in experiment. The other two $\Omega = C^0_H/\gamma C R_S$ and $i_0 = I_0 (R_S/\gamma T_B)^{1/2}$ depend on the heat transfer rate γ and heat capacitance C^0_H, which are difficult to estimate and measure. We will use them, as well as capacitance C, as fitting parameters. Ω determines the range of dimensionless external currents i^{min}_0 and i^{max}_0, where oscillations do appear. Their ratio $i^{max}_0 / i^{min}_0 = I^{max}_0 / I^{min}_0$ defines it as $\Omega \sim 0.46$. The last parameter i_0 can be calculated as $i_0 = I_0 i^{max}_0 / I^{max}_0 = I_0 i^{min}_0 / I^{min}_0 \sim 0.95$. For this set of parameters, we calculate the dimensionless period T_0 and fix the capacitance C so that $T_{exp} = C R_S T_0$. It results in $C_{fit} = 29$ μF while $C_{exp} = 47$ μF, which appear to be in modest agreement. Now all parameters in Eqs. (1) are determined, and their numerical integration results in theoretical curves in Figures 3.6 and 3.8. Deviations from the proposed model may stem from various origins. One such origin may be the previously reported nontrivial magnetic behavior manifesting as either ferromagnetic domains confined to the surface[74], or as fluctuating magnetic fields present in the bulk[75]. It is believed that the temperature range of interest in this study precludes the existence of these magnetic domains, thus no contribution to the model is expected. However, the aforementioned magnetic fluctuations may play a role in these transport data if they contribute in a way to the heat capacity of SmB_6 or the thermal linkage to the bath. However, due to the small magnitude of those fluctuations as well as the sub-μs time scale, it is unclear what affect they may have on these time-dependent thermal properties. Generally, the proposed model in Eq. (1) relies very generally on conservation of energy and charge. Specific scattering terms that occur in transport are accounted for entirely by

the surface or bulk resistance and specific heat. Any interaction that may lead to modifications of those conservation laws could in theory modify the model to suit more complex system behavior.

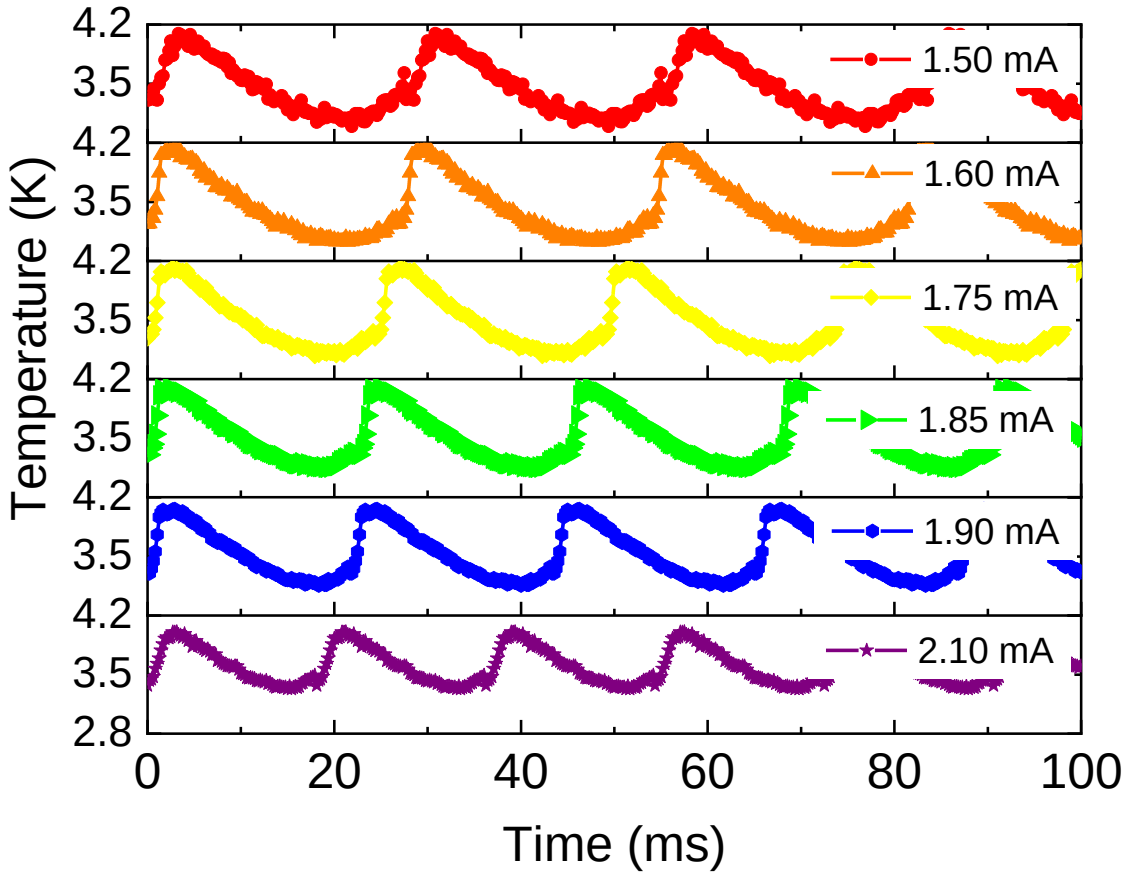

Figure 3.7 Waveforms of selected applied currents Io ranging from 1.5mA to 2.1mA. Each curve here underwent a different number of total period averages due to the amount of data available for each applied current.

Select waveforms for six currents can be seen in Figure 3.7 under various values of I_o. The frequencies of crystal voltage and thermal oscillations can be seen in Figure 3.8. To measure the frequency of the crystal voltage and temperature oscillations, FFT spectra calculated from raw data were fit using a Lorentzian to identify the center frequency and peak width. The full width at half-maximum was used to estimate an upper bound in the uncertainty in the frequency, which in all

cases was negligibly small. For the sake of comparison, the current-dependent frequency plot can be constructed from the data collected by the DAQ and processed with the method. Note that using the model described above, using parameters from this particular sample as discussed previously, we were able to construct the dashed curve of frequencies as a function of applied current, as seen in Fig.8 in black. It should be noted that the theoretical data were calculated to match the frequency of the 1.9 mA point. Interestingly, it appears that the experimental data are more sensitive to the crystal bias than the model had suggested, though both are in good agreement

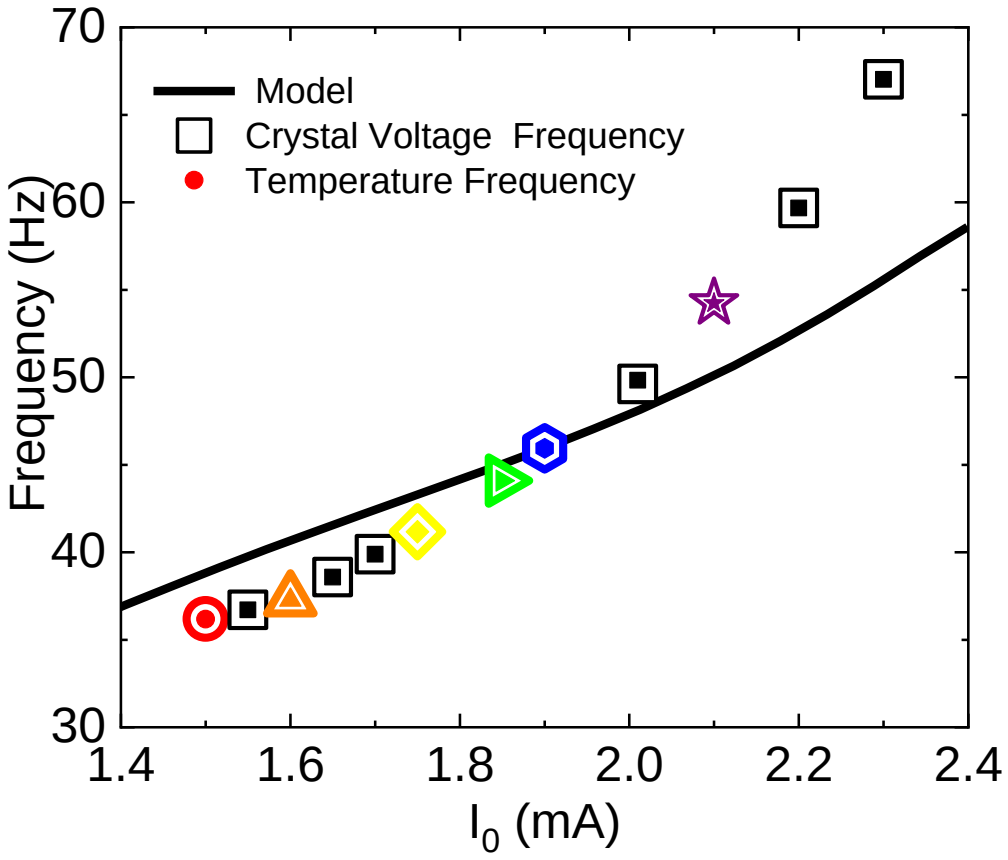

Figure 3.8 Center frequency of crystal voltage and thermal oscillations in solid and open symbols, respectively. Functional dependence derived from the model is presented as a black solid curve. Colors that are not black here represent the data shown in figure 3.7.

3.5 Conclusion

This work relied heavily on the development of this signal processing technique in order to extract the physical waveforms of the thermal oscillations. Upon presenting this work at the APS March Meeting in 2018, I was notified that using an Arduino and some simple programming, that likely this signal processing method would not have been required. As such, it is entirely possible for one to work on a similar oscillator device, say of a new Topological Kondo Insulator, $FeSb_2$[76]. Unfortunately, extending this device to other Topological Insulators likely requires systems with very few in gap states or extremely high bulk resistance, like SmB_6. This makes compound $FeSb_2$ a potential candidate material, though with all the same low temperature draw backs to SmB_6. However, as the constituent elements are cheaper than those in this work, perhaps it would present itself as a more economical option for development if the opportunity was presented.

In summary, we have experimentally demonstrated the surface-state thermal oscillation in SmB6 oscillator devices. The observed amplitude, phase, and waveform all agree well with the proposed theoretical model[57],and they will enable the development of THz SmB6 oscillators with quantitative theoretical guidance.

Chapter 4

Transition between fractional quantum Hall and meta-stable anisotropic states near filling factor v = 5/2 by uniaxial strain

We report strain-dependent low temperature magneto-transport measurements of a two-dimensional electron gas confined in GaAs single quantum wells. The sample was mounted to a piezoelectric-based strain device with which we could apply and vary tensile strain *in situ*. With this apparatus, we achieved strains as large as ~0.49% in GaAs quantum wells below 100mK. We

found that increasing strain causes the longitudinal electrical transport of the 2DEG confined in the quantum well to become anisotropic near the filling factor $\nu=\frac{5}{2}$. Further complicating the observation was that the effect of strain on the $\nu=\frac{5}{2}$ state is highly sensitive to the magnitude of the magnetic field at which strain was applied. We found that applying strain while the 2DEG is in high magnetic fields produces a profound effect, while low field strain applications yields completely isotropic transport. Additionally, the new states were metastable and would relax back into the pre-strained ground state given sufficient time and temperature.

4.1 Introduction

Two-dimensional electron gases (2DEG) in GaAs/AlGaAs heterostructures are compelling systems to study due to their low electron density and high electron mobility, causing the interactions between electrons to be dominated by their Coulomb interactions and not their collisions. When an out-of-plane magnetic field is applied to a 2DEG, the electrons separate into discreet Landau levels producing novel physics including a Fermi liquid, a stripe phase[77], and non-Abelian statistics[78]. Quantized Hall states form, signified by a quantized plateau in the Hall resistance and near-zero longitudinal resistance, for integer values of $\nu=nh/eB$ called the Integer Quantum Hall (IQH) effect[79], where ν is the integer filling factor, n is the electron density, and B is the magnitude of the perpendicular magnetic field. Quantized states form at certain fractional filling factors for ν, called Fractional Quantum Hall (FQH) states[80–84]. The most interesting FQH state is the $\nu=\frac{5}{2}$ state[85] because it is one of only two even denominator FQH states, with the other being $\nu=\frac{7}{2}$, and its potential to host quasiparticles that are naturally non-Abelian, with its possible application in quantum computing[78]. For this paper, we wish to only focus on states between $\nu=2$ and $\nu=3$ filling factors, which lie in the N=1 Landau level.

Previous experiments have revealed isotropic longitudinal resistances for the FQH state at $\nu=\frac{5}{2}$, without any external perturbation[77,85,86]. Stripe phases, evidenced by an anisotropic longitudinal resistance between the $<1\bar{1}0>$, x, and <110>, y, crystal axes, exist naturally in higher Landau levels[77], but can be reoriented by an external perturbation, such as an in-plane magnetic field[86]. At the $\nu=\frac{5}{2}$ state, in-plane magnetic field experiments revealed a stripe phase developing to replace the FQH state, but at higher fields a re-entrant isotropic state was observed[87,88]. Three-dimensional pressure measurements have revealed an anisotropic longitudinal resistance behavior around 8.5kbar and below 30mK, implying the development of a nematic phase[89,90]. However, these measurements were unable to tune the external force *in situ*, potentially inhibiting a full understanding of the underlining mechanisms. Additionally, metastable states can form through the directionality of a magnetic field sweep, which has a thermally driven relaxation dependence back to an equilibrium around $\nu=\frac{9}{2},\frac{13}{2},2$[91,92]. Our experiment sought to observe the effects of uniaxial tensile strain on GaAs quantum wells around the $\nu=\frac{5}{2}$ filling factor.

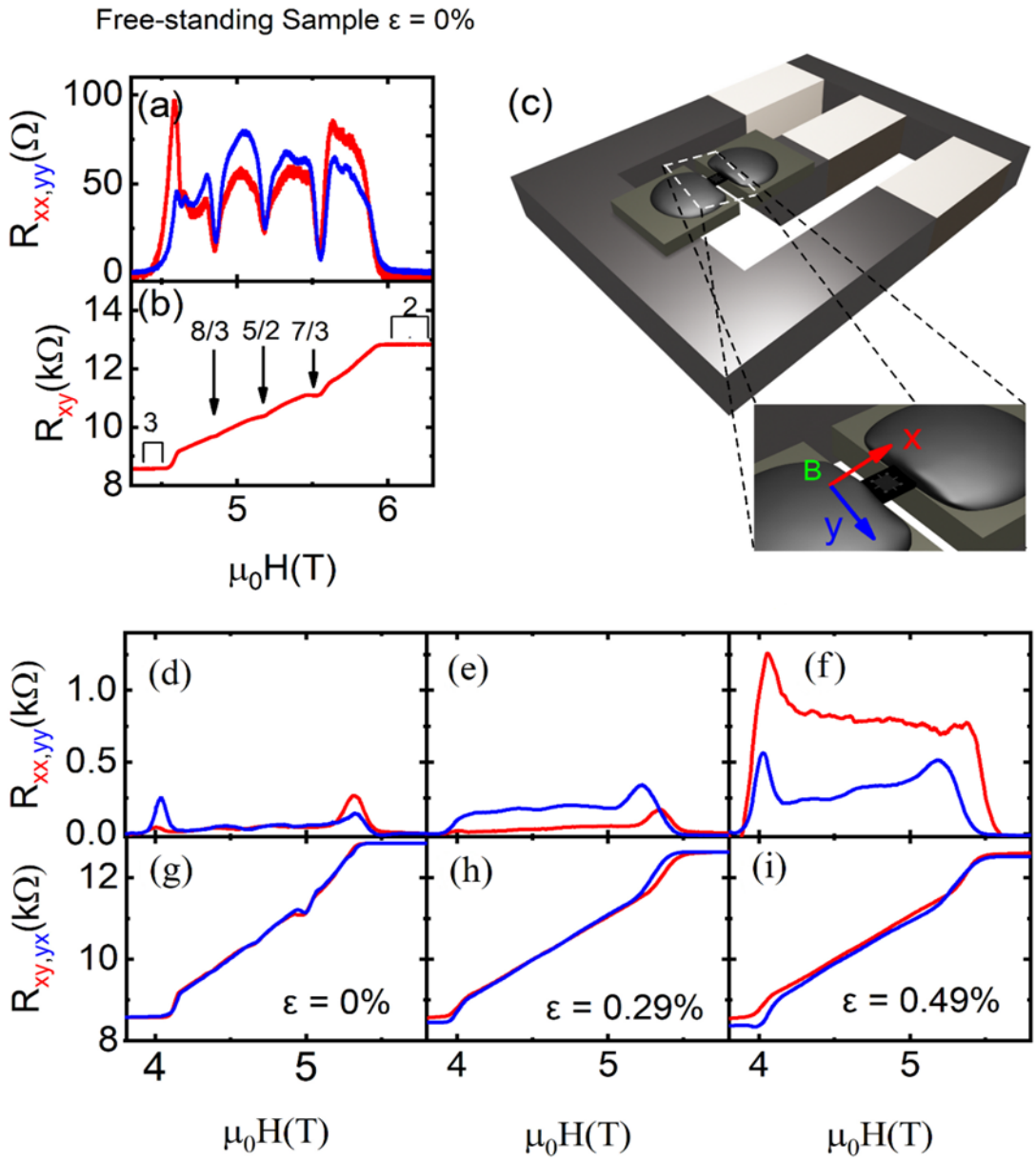

Figure 4.1: ***Experimental setup and uniaxial strain induced longitudinal resistance anisotropy.*** *(**a**) Longitudinal resistance in x(y) in red(blue) and (**b**) the matching Hall resistance at 50mK in red showing clear signatures of the FQHE states at $\nu=\frac{8}{3},\frac{5}{2},\frac{7}{3}$ labeled with arrows and integer Hall states ν = 2, 3 labeled with partial rectangles. (**c**) Simplified 3D cartoon of our homemade strain cell utilizing three piezoelectric stacks (white) to apply strain. The sample, with the 2DEG, is mounted across a gap between the washers with x and y axes labeled in red and blue, with the x-axis parallel to the direction of strain. The magnetic field, B, is labeled in green and is normal to the 2DEG. Longitudinal resistance data at 85mK under tensile strain at 0% (**d**), 0.29% (**e**), and 0.49% (**f**) showing a strong departure from isotropic transport to a highly anisotropic state with strain. Hall resistance data at 85mK under tensile strain at 0% (**g**), 0.29% (**h**), and 0.49% (**i**) in which Hall plateaus for FQHE states are suppressed at higher strain. Strain is applied with the magnetic field help constant at $\nu=\frac{5}{2}$.*

4.2 Methods

The sample was fabricated from a conventional modulation-doped AlGaAs/GaAs/AlGaAs quantum well grown via molecule beam epitaxy (MBE) on a <001>-oriented GaAs substrate. The GaAs quantum well had a width of 30 nm and was flanked by alloy $Al_{0.2}Ga_{0.8}As$. Silicon delta-doping layers in the alloy were symmetrically positioned above and below the quantum well and populated it with a 2DEG with a nominal density of 2.7×10^{11} cm^{-2} and a low temperature mobility of 8.8×10^{6} cm^2 / V·s. The sample was cleaved into a rectangle 7 mm × 3 mm and thinned from the substrate-side to a thickness of 195 μm. The 2DEG was photolithographically confined to a 1.5 × 1.5 mm square region at the center of the thinned rectangular film. Eight diffused Au/Ni/Ge ohmic contacts positioned at the corners and side midpoints of this square region provided electrical contact to the 2DEG in the quantum well and enabled low frequency AC electrical transport measurements, which were performed at a frequency of 13 Hz and with a current of 50nA with Signal Recovery lock-in amplifiers.

The sample was mounted into the strain cell via Stycast 2850FT epoxy. Measurements were performed in an Oxford Instruments dilution fridge. The magnetic field and strain were never changed simultaneously.

For our experiment, we utilized a strain cell design, shown in Figure 4.1c, which concentrates the movement of three piezoelectric stacks across a narrow gap where a sample was mounted, allowing strain to be applied uniaxially, while compensating for thermal contraction[93]. Similar devices have been used to increase the superconducting transition temperature of Sr_2RuO_4[94,95] and enhance the bandgap and surface conduction of SmB_6[55]. These experiments were performed on single crystals, but the design is compatible with thin films, provided that the cross-sectional areas are sufficiently

small. The strain cell achieved higher *in situ* uniaxial strains than previous experiments on GaAs/AlGaAs quantum wells in which the sample was mounted to the side of a piezoelectric stack with epoxy[96–99], which does not compensate for thermal contraction. The strain cell is a substantial increase over previous experiments on GaAs/AlGaAs quantum wells, where sample's material properties limit the possible strain more than the strain device's capabilities.

4.3 Development of Transport Anisotropy

For the initial measurements, the sample was cooled in a dilution refrigerator before being mounted into a strain cell. This allowed us to determine the ideal illumination conditions, reach a lower sample temperature, and measure the unstrained behavior before proceeding to strain dependent measurements. Shown in Figure 4.1a, the longitudinal data are nearly isotropic, as expected from unperturbed FQH states at 50mK. Additionally, in Figure 4.1b, the Hall data show strong IQH plateaus at ν=2,3 and the development of three FQH states at $\nu=\frac{7}{3},\frac{5}{2},\frac{8}{3}$, indicated by local-minima in R_{xx} and R_{yy} and clear quantized plateaus in R_{xy}. This indicates our sample was of good quality and an ideal candidate for uniaxial strain experiments.

All data discussed hereafter was taken while the sample was mounted in the strain cell, shown in Figure 4.1c. Shown in Figures 4.1d and 4.1g, we repeated the unstrained measurements and observed isotropic longitudinal resistances and Hall resistances with weakly developed FQH states, which can be attributed to a higher minimum sample temperature of 85mK while the sample was mounted in the strain cell. When at 0.29% tensile strain, the longitudinal resistances became highly anisotropic with a hard axis forming on the y-axis and an easy axis forming along the x-axis, signified by a higher longitudinal resistance in R_{yy} than in R_{xx} at $\nu=\frac{5}{2}$. This is shown in Figure 4.1e and the accompanying Hall data is shown in Figure 4.1h. A weakened signature of the $\nu=\frac{5}{2}$

state was still observed in the Hall resistance, though later analysis will be more enlightening. Extraordinarily, the anisotropy reoriented when a higher strain of 0.49% was applied. The x-axis became the hard axis and the y-axis became the easy axis, shown with the longitudinal data in Figure 4.1f and the Hall data in Figure 4.1i. These strain-induced anisotropic states were reminiscent of previously reported stripe phases at filling factor $\nu=\frac{5}{2}$ induced by an in-plane component of the magnetic field that emerged only at very low temperatures[88]. The data in Figures 4.1d-i were taken after applying strain in a magnetic field corresponding to the $\nu=\frac{5}{2}$ state. The significance of the magnitude of the magnetic field at which strain was applied will be discussed in detail below.

Initial measurements yielded results that, while unique, were difficult to reproduce. Inconsistencies existed in the orientation of the hard and easy axes during strain measurements. However, the origin of these inconsistencies became obvious when considering the dependence of the strain-induced behavior on the magnitude of the magnetic field at which strain was applied.

Additional measurements were taken with strain applied at several magnetic field. In short, strain had a minimal effect on the system when applied without magnetic field present, but often a large effect when applied with a high magnetic field. Alternatively, the Landau level the electrons occupy when strain was applied correlated with the development of the resistive anisotropy. To probe this complicated effect, the magnetic field was set to the desired filling factor before strain was increased. The field was held constant while the strain was applied. The strain was then held constant as magnetic field swept from $\nu=2$ to $\nu=3$.

4.4 Landau Level Dependence of Transport Anisotropy

Additional data were taken with various strain values applied at $\nu=\frac{5}{2}$ to build color plots the should the longitudinal anisotropy in Figure 4.2a and the difference of the Hall data, R_{xy}, from the classical Hall resistance in Figure 4.2d, which effectively illustrates the emergence of FQH states. Vertical dashed lines denote the approximate location of the $\nu=\frac{8}{3},\frac{5}{2},\frac{7}{3}$ states. This data provided further evidence for a hard axis reorientation from the y-axis at around 0.3% strain to the x-axis at around 0.45% strain, with minimal anisotropy for low strain values. The field at which R_{xy}-$R_{\text{Classical Hall}}$ crosses 0Ω represent the approximate location of a quantized Hall state or other quantum state. The large deviations at low and high fields in Figure 4.2d represent the emergence of IQH states, $\nu=2,3$. Although there was some slight weakening of the development of the $\nu=\frac{5}{2}$ state as strain increased, there was still evidence of fractional filling states through the entire strain region.

Similarly, data were collected with the strain applied at $\nu=2$, shown in Figures 4.2b,e. The longitudinal resistance anisotropy was qualitatively similar to that of Figure 4.2a. Both showed longitudinal anisotropy forming with the y-axis being the high resistive axis and then switching to the x-axis as the high resistive axis with higher strain. Both $\nu=\frac{5}{2}$ and $\nu=2$ lie in the N=1 Landau level, hinting that the effect was caused by the Landau level the electrons occupy at which strain was applied. Additionally, the anisotropies of the $\nu=2$ data were larger hinting that the anisotropic magnitude increased with the magnetic field at which strain was applied. Furthermore, the Hall data is remarkably similar to the $\nu=\frac{5}{2}$ data, hinting at the similarities in the effects. In this case, the survival of the $\nu=\frac{5}{2}$ state appears tenuous, as the deviations from the classical behavior was weak at strain values of 0.5%. However, clear signatures of the FQH state exist at 0.4% and lower strain.

Strain caused large longitudinal resistance anisotropies and weakened the FQH states when strain was applied at ν=2 similar to the data when strain was applied at ν=$\frac{5}{2}$.

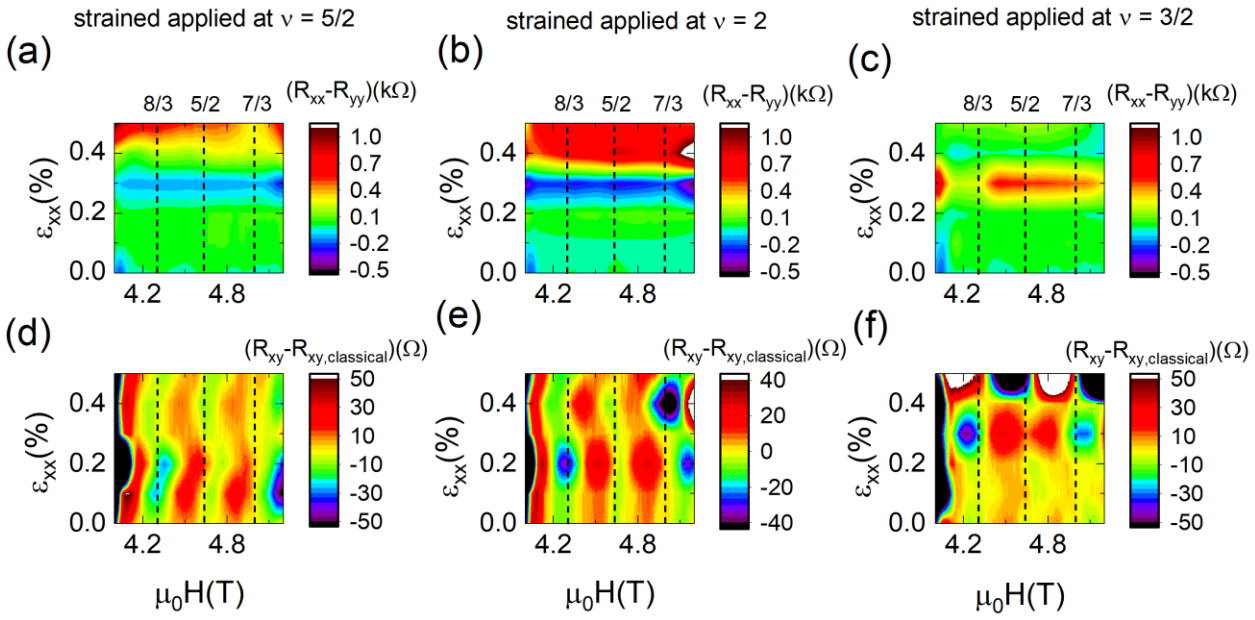

Figure 4.2: ***Large anisotropic response to uniaxial strain when applied at higher magnetic fields.*** *The ν=$\frac{8}{3}$,$\frac{5}{2}$,$\frac{7}{3}$ states are marked with dashed vertical lines. The longitudinal resistance difference (R_{xx} - R_{yy}) data plotted as a color plot to show the anisotropy developing along two different directions when strain was applied with a magnetic field that puts the system at the ν=$\frac{5}{2}$ (**a**), ν=2 (**b**), and ν=$\frac{3}{2}$ (**c**) states. Areas of blue indicate an anisotropy with R_{yy} as the hard axis, while areas of red indicate an anisotropy are plotted with R_{xx} as the hard axis. The difference of the R_{xy} Hall data and the classical Hall resistance, when strain was applied with a magnetic field that puts the system at the ν=$\frac{5}{2}$ (**d**), ν=2 (**e**), and ν=$\frac{3}{2}$ (**f**) states. Areas of rapid transition between two colors indicate a deviation from the classical Hall resistance like the presence of a Hall plateau. Rapid transitions occur for ν=$\frac{8}{3}$,$\frac{5}{2}$,$\frac{7}{3}$. There are no longer rapid transitions until 0.45% strain indicating that the FQHE states are weakened. After 0.45% strain at ν=$\frac{3}{2}$, there emerges a non-classical behavior, indicated by the large deviation from the classical Hall resistance.*

Additionally, the same experiment was repeated with strain applied at a magnetic field corresponding to ν=$\frac{3}{2}$, shown in Figures 4. 2c,f. Contrasting data in Figures 4.2a,b with Figure 4.2c, the high resistive axis around 0.3% strain was the x-axis, instead of the y-axis, opposite from when strain was applied at ν=$\frac{5}{2}$ or ν=2. Here, ν=$\frac{3}{2}$ lies in the N=0 Landau level, hinting again that the effect was influenced by the Landau level the electrons occupied when strain was applied.

Furthermore, at higher strains, the sample became more isotropic, although it seemed possible that the sample would reorient again if more strain was applied. Additionally, the difference of the Hall data, R_{xy}, and the classical Hall resistance is plotted in Figure 4.2f, showing only slow color transitions over a wide strain range signifying a weakening of the FQH states. However, for strains around 0.5%, the rapid color transitions were strong, signifying that a non-classical behavior occurred at higher strains. The orientation of the anisotropy and robustness of the FQH states were strongly affected by the field applied while the strain was increased.

In order to show that the effects were not simply due to the underlying strained lattice, and as such caused by a deformation of the Brillouin Zone boundary, we chose to examine the effects of strain application without magnetic field and at a magnetic field corresponding to the $\nu=5$ state as shown in Figures 4.3a,c and 4.3b,d, respectively. Figures 4.3a,b show the difference of R_{xx} and R_{yy} to highlight any anisotropies. The data show no major anisotropy developing over the entire range of strains. The differences of the Hall data, R_{xy}, and the classical Hall resistance are shown in Figures 4.3c,d. There are several transitions across 0Ω at several values of ν, where the signatures of FQH states remain regardless of the strain applied. When the system was strained with only a small magnetic field applied, the electrons were in higher Landau levels and the system showed only minor effects from strain. This evidence hints that the effects of strain observed in Figure 4.2 are unlikely to be explained solely on the basis of a BZ boundary deformation. It is clear, however, that in order to successfully manipulate the nature of transport anisotropy in these FQH states, the sample must be lower than the N=2 Landau Level, otherwise the states appear invariant under strain. The effect is above Hartree-Fock because stripe phases are expected at $\nu=\frac{9}{2},\frac{11}{2},\frac{13}{2}$, but there are no stripes phases forming for any value of strain. These data showed how robust the isotropy and the FQH states were to uniaxial strain without an applied field during straining.

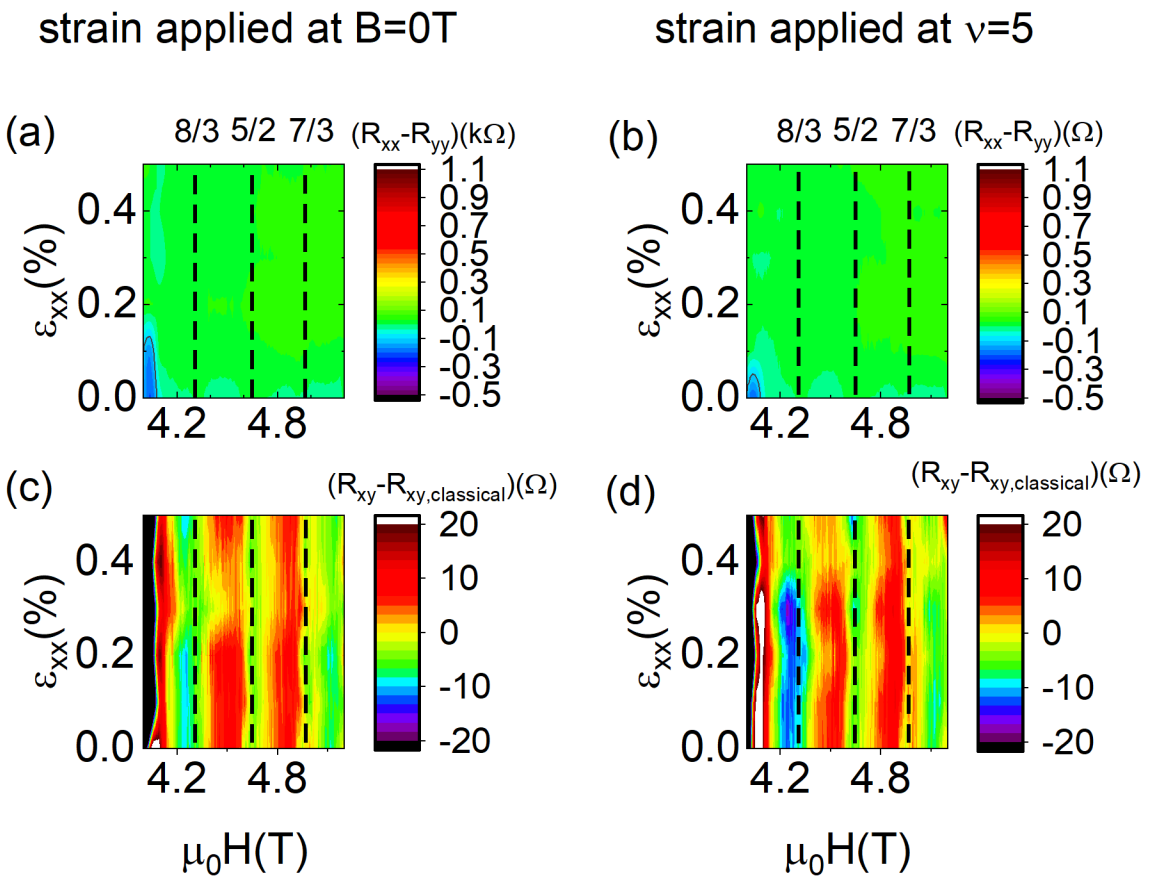

Figure 4.3: ***Isotropic response to uniaxial strain when applied at lower magnetic fields.*** *The $\nu=\frac{8}{3},\frac{5}{2},\frac{7}{3}$ states are marked with dashed vertical lines. The longitudinal resistance data difference (R_{xx} - R_{yy}) plotted as a color plot to show an isotropic behavior when strain was applied without a magnetic field applied (**a**) and with strain applied at a magnetic field corresponding to $\nu=5$ (**b**). The difference of the R_{xy} Hall data and the classical Hall resistance when strain was applied without a magnetic field applied (**c**) and with strain applied at a magnetic field corresponding to □=5 (**d**). Areas of rapid transition between two colors indicate a deviation from the classical Hall resistance like the presence of a Hall plateau. Rapid transitions occur for $\nu=\frac{8}{3},\frac{5}{2},\frac{7}{3}$.*

4.5 Metastability of Anisotropic FQH States

Consequently, there was a strong need to find a way to "reset" the system between taking data sets to avoid observing the effects of the previous strain. For this, we explored the effects of thermal cycling the sample to remove strain induced effects. The system started in an isotropic unstrained state at T=85mK, shown in Figure 4.4a. Then, the sample was strained to 0.29% in a magnetic field at $\nu=\frac{5}{2}$ to produce an anisotropic longitudinal resistance with R_{yy} as the high resistive axis, shown in figure 4b. The sample was then warmed to T=1.2K with the same strain still applied and the longitudinal resistances returned to an isotropic state, as shown in the figure 4c, which was the expected unstrained sample response at T=1.2K. Similar to the previously reported in-plane-field-induced stripe phases[91], the anisotropic electrical transport could only exist at low temperatures. Strain effects disappeared at higher temperatures. This was not surprising given the need for high quality samples to observe such an effect.

However, surprisingly, upon cooling the sample back to base temperature while maintaining the uniaxial strain at 0.29%, the sample remained in a low resistive isotropic state, as can be seen in the longitudinal data in Figure 4.4d. The matching Hall data for Figure 4.4a-d is shown in Figures 4.4e-h. The fractional Hall plateaus were not well developed, but there is a trend towards flattening in the Hall resistance at $\nu=\frac{5}{2}$ and there is a small trend towards zero in the longitudinal resistance at $\nu=\frac{7}{3},\frac{5}{2},\frac{8}{3}$. It would be improper to say we see FQH states, instead there were weak FQH states or trends towards FQH states. This could be caused by a higher sample temperature, which could come from the leakage current in the piezo stacks, which were close enough to the sample that they might not be observable by the sample thermometer. Additionally, it could also be a minor non-metastable effect of strain. However, it was crucial to apply uniaxial strain at exceptionally

low temperatures in order to create the observed anisotropic state, suggesting that applying strain at higher temperatures would lead to fast relaxations back to an isotropic state, before an anisotropic state could be stabilized and measured. This cycle can be observed in Figures 4.4a-d. We note that the piezo based strain cell is an important component to enable the above observations due to the ability to tune strain *in situ*.

To test the above hypothesis regarding the possible relaxation back to an isotropic state at elevated temperatures even with the presence of strain, we performed the following detailed temperature-dependent relaxation experiments, and have confirmed that the observed strain-induced anisotropic states were metastable in nature, which was different from previously reported stripe phases[88,89]. We knew that at T=100mK and below, an isotropy could develop with strain, while above T=1.2K, strain had a minimal effect. To study this relaxation, all strain was removed at T=1.2K. The sample was subsequently cooled below T=100mK without strain, shown in figure 4a. Strain was then applied to the sample, giving rise to the anisotropic longitudinal resistance response discussed previously and shown in Figure 4.4b. The sample was then warmed to a set temperature and allowed to relax until the longitudinal resistance anisotropy was suppressed while strain was still applied, similar to Figure 4.4c. We observed that the rate of relaxation back to an isotropic ground state was temperature dependent; relaxation times decreased with increasing temperature. Data were taken at temperatures between T=500mK and T=1350mK, shown in Figure 4.4i. The relaxation times ranged from about a minute to several days. Our estimates suggested that at temperatures of T=85mK an isotropic state would reemerge after roughly 20 years of relaxation, highlighting the high degree of stability at low temperatures. A clear knee in the data that was temperature dependent was indicative of a double relaxation mechanism with

two difference relaxation time constants. *In situ* strain created two temperature dependent metastable anisotropic states only observable at exceptionally low temperatures.

Due to the anisotropic nature of this state, evaluating the proposed order parameter[100] could potentially provide more insight. The order parameter used in this work is $P = \frac{R_{yy} - R_{xx}}{R_{yy} + R_{xx}}$.

As seen in Figure 4.4j, the proposed order parameter for two intermediate temperatures are plotted as a function of time and fit to a sum of exponential functions. This fitting function, $P = R_1 e^{-\tau_1 t} + R_2 e^{-\tau_2 t}$, appears to reproduce the qualitative nature of the data suggesting that two separate decay processes were responsible for the knees in Figure 4.4i. The nature of these two mechanisms and their relation to the strain are still under investigation.

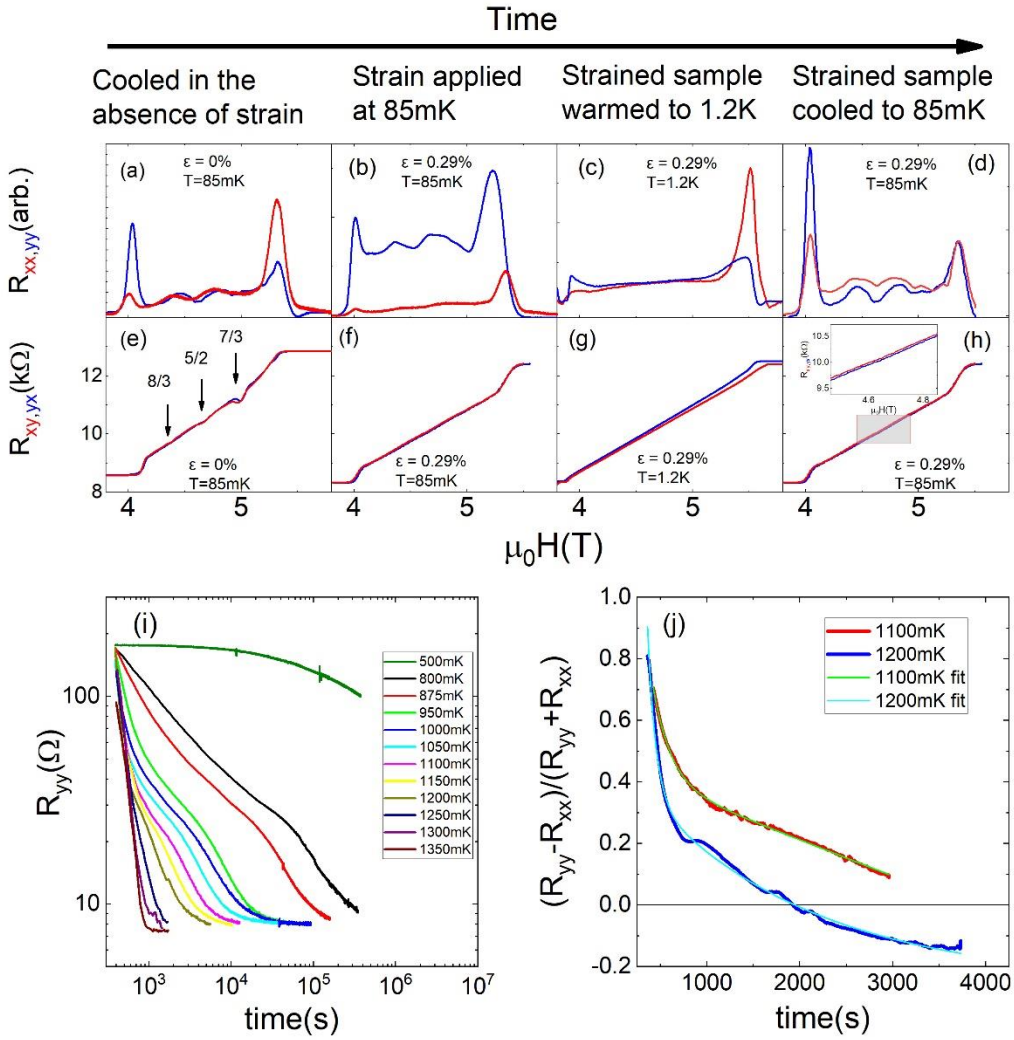

Figure 4.4: ***Metastable state cycle and higher temperature relaxations. (a)*** *The sample was cooled to 85mK in the strain cell without any piezoelectric stack actuation, therefore the sample was under minimal applied strain. (**b**) The sample was strained to 0.29% tensile strain at 85mK showing clear signs of anisotropic longitudinal resistance. (**c**) While the same strain from figure 4b was still applied, the sample was warmed to 1.2K and held at 1.2K until the sample reached electrical equilibrium. The data show no clear signature of anisotropic resistances. (**d**) The sample was returned to 85mK while 0.29% tensile strain was still applied and shows signatures of a FQHE state with near isotropic resistances. (**e-h**) Corresponding Hall resistances for figures 4a-d. (**i**) Relaxation of R_{yy} around $\nu = \frac{5}{2}$ for various temperatures towards an unstrained ground state resistance value showing a clear knee in the data indicative of two relaxation constants. The relaxation at 1350mK happens on the order a minute, while the relaxation of 500mK is not observed over several days. Temperature shows a strong dependence in the relaxation. (**j**) Relaxation of proposed order parameter for two example temperatures from Figure 4i.*

4.6 Discussion

We must examine the possibility that strain creates defects in the 2DEG. We cannot rule out that the strain was applied in such a way that it creates displacement defects rather than uniformly changing the lattice constants. Defects could cause the anisotropy since the strain was applied in an anisotropic method. This would cause additional electrons to be trapped in the defects, causing the slight reduction observed in the electron density. Although, one would also expect to see larger integer hall plateaus, which are not observed. Additionally, annealing was unlikely to occur at such a low temperature as the ions will not have sufficient thermal energy to remove the defects and return the system to its pre-strained state. This made it unlikely that defects were the primary cause.

In a previous study, metastable states were created at $\nu=\frac{9}{2},\frac{13}{2}$ by the directionality of the magnetic field sweeps[91], forming anisotropic states with directionality determined by whether the field sweep was increasing or decreasing. There were two separate ground states with an energy barrier between them, which trapped the system in the anisotropic states. The metastable nature of this state comes from the interactions between the states; where given sufficient temperature and time, the system will relax back into its original ground state.

Similar behavior was observed in this work with a few exceptions. The energy required to form a different ground state was provided by the strain, not the magnetic field sweep. Furthermore, the energy barrier was higher since a higher temperature was required to cause the relaxation. There is also a Landau level dependence that should be examined, where electrons were more sensitive to shape changes. Higher magnetic fields cause higher cyclotron frequencies and, therefore, higher electron energies. After the addition of strain, the cyclotron orbits were stretched into an ellipsoidal orbit, increasing eccentricity, which was not preferred and kicked some electrons out of their orbits

with high enough energy to jump over an energy barrier and into a new metastable state. The electrons were forced out anisotropically since strain was applied anisotropically, along only the x crystal axis, causing the observed resistance anisotropy. The anisotropy was destroyed once the electrons have enough energy, given sufficient time and temperature, to escape over the energy barrier back into their preferred ground state, which restores the isotropy. Coincidently, the energy difference between Landau levels(~0.8meV) was within an order of magnitude of the thermal energy around T~1K (~0.1meV), providing the energy needed for the system to relax into the preferred ground state. If the strain was applied at or above T=1K, then the metastable state would relax before it could be observed with a magnetic field sweep, as a magnetic field sweep would require a longer time than was required for the relaxation. After cooling, the metastable state could be reintroduced with the application of strain at T=100mK or below, causing the same process to begin again.

4.7 Conclusion

In summary, we demonstrated that uniaxial strain has in some ways a similar effect on the $\nu = 5/2$ state as other similar symmetry breaking methods, such as field tilting. The induction of transport anisotropy, and the clear change in the resistive hard and easy axes suggest that the symmetry breaking itself, not simply lattice distortion is a key component to the physics observed in this work. However, the observation of the Landau Level dependence, in which the effect of strain can be greatly mitigated or enhanced depending on the Landau Level occupied during the application of strain is a completely novel observation. This required the use of an *in situ* tuning parameter, such as piezo electric controlled strain.

The observation that we could effectively eliminate the FQH behavior at the filling factor $\nu = 5/2$ by applying strain at the fermi liquid state $\nu = 3/2$ is a fascinating development, suggestive of some memory effects in this system.

Finally, the metastability here, though in some way typical in that the clear exponential decay can be seen from the phenomenological order parameter, exhibit a strange double exponential component potentially suggestive of simultaneous and decoupled relaxations. The nature of this is still entirely unclear.

Clearly there is a plethora of rich physical phenomena at play in this system, and we hope that this work will help to spur further experiments and theoretical insights.

Chapter 5

Strained thermal conductivity in SmB_6

I report in this chapter progress on further understanding the thermal conductivity, $\kappa(T)$ in single crystals of SmB_6 growth from aluminum flux. Various experiments on thermal conductivity of SmB_6 have resulted in disparate interpretations of the magnetic field dependence of crystals grown by both floating zone (FZ) and flux grown (FG). I believe these likely originate in an underlying variation in the chemical composition of these single crystals between these two growth methods. In utilizing a uniaxial strain technique, I sought to simulate the lattice distortion effects present in FZ grown samples due to implicit Sm vacancies. As such, the development of a novel thermal conductivity experiment, compatible with the Hicks style uniaxial strain cells needed to be developed. By symmetrizing the conventional four-probe thermal conductivity experiment, I have

been able to perform thermal transport experiments in these strain cells, demonstrating the capability. This should allow for the further exploration of the magnetic field-strain-temperature parameter space required for deeper insights into the bulk transport phenomena in SmB_6.

5.1 Introduction

The description of SmB_6 as a traditional Kondo Insulator has given way to the view that it is a less typical Mixed Valence Insulator. The nature of the oxidation state fluctuations on the Sm ion has still been fairly elusive, though recent works suggest that a charge transfer mechanism between a Sm ion and a boron-boron dimer appears to reproduce much of the bulk physics observed in SmB_6[54]. These properties have included the anomalously large linear heat capacity in SmB_6, the temperature dependent evolution of the average oxidation from 2.67 to 2.5[101], as well as the pressure dependence. This lattice distortion driven charge transfer mechanism would lead to the suggestion that the valence may be tuned carefully through applications of mechanical force such as pressure cells or newly popularized uniaxial strain cells.

An investigation into the nature of the bulk excitations in SmB_6 has intensified in the last few years due to the potential for the compound to host charge neutral fermionic excitations, a potential quantum spin liquid[49–51]. Naturally, these quasi particles would not couple to the electric field in resistance measurements, which would generally be shorted out by the conductive surfaces. Quantum Oscillation experiments have proven to be a quagmire due to multiple contradictory reports[45,46]. To this date, there have been two reports of oscillations attributed to a large 3-D Fermi surface taking up more than half the Brillouin Zone [53,102].

These results out of Cambridge were followed up by various thermal conductivity studies. Thermal conductivity couples strongly to the statistical behavior of the underlying quasi particle excitations.

Thermal conductivity experiments, which are not only capable of probing bulk excitations, are also capable of distinguishing between excitations that are fermionic or bosonic in nature. Deviations from a pure phonon gas thermal conductivity would be indicative of a charge neutral excitation that, emerges as a linear temperature dependence to conductivity. Three works on floating zone grown samples show exactly this, in which the residual linear term of thermal conductivity was strongly magnetic field dependent in that the deviation from pure phonon contribution increases with increasing magnetic field up to 12T[53,102,103].

Unfortunately, this work appears to also highlight a highly nonmonotonic behavior of thermal conductivity with magnetic field for Al flux grown crystals, and a radically different behavior for floating zone grown crystals.

A systematic study of thermal conductivity below 1K of flux grown and floating grown zone samples for pure and carbon doped samples provided substantial insight into the disparities between FZ and FG samples[52]. This work highlights two experimental observations. The first is that the observed non-monotonic behavior of thermal conductivity with regard to magnetic field likely originates from a Schottky Anomaly like suppression of phonon scattering from magnetic moments. These moments were estimated to be from a J = 5/2 moment, likely due to the Sm^{3+} ions always present in SmB_6.[48,52] The second observation is that down to temperatures near 100mK there appears to be no deviation from a boundary scattering limited non-interacting phonon gas for all samples.

This disagreement from these works points to the possibility that in sample variations play a more important role in the physics of SmB_6 than previously expected. Studies have recently shown that while flux grown samples frequently contain pockets of Al[34,104] that are known to grow epitaxially

to SmB_6 with a similar structure and lattice constant, making it nearly impossible to identify from XRD, floating zone grown samples appear to suffer from non-stoichiometric crystal growth. This non-stoichiometric behavior of the growth was attributed in part to the high temperature of the synthesis, likely boiling of Sm out of the feedrod, though a precise origin has not been identified.[34] As such, it leads one to suggest that Sm vacancies, and by extension additional J= 5/2 moments that are given rise to by Sm vacancy, may be responsible for the variance of thermal conductivity and dHvA data between flux and floating zone grown samples. In fact, inverse-Corbino[105] measurements have shown that Sm deficient samples appear to have a much higher bulk electrical conductivity, undercutting the expected nature of a highly insulating bulk.

Previous work has shown that uniaxial strain experiments are capable of tuning bulk energy scales, observable through the evolution of the bulk band gap with tensile and compressive strain.[106] This behavior was suggested to be due to the local structural distortions altering the energetics required for the charge transfer leading to the oxidation state fluctuations. Though this is still an open area of research, it is clear that with lattice compression, Sm ions will tend to exist in higher numbers in the Sm^{3+} state leading to additional J = 5/2 moments. It has been recently proposed that boron dimerization between atoms crossing Sm faces, pictured in figure 5.1, and lattice distortion can account for the charge transfer mechanism required for the observation of valence fluctuations on the Sm sublattice.[54] As such, uniaxial strain studies of thermal conductivity may be the key experiment required to reconcile experimental data and verify the existence of this charge neutral fermionic excitation.

5.2 Samples and treatments

For our study, crystals of SmB_6 were grown from an aluminum flux under excess argon pressure. Upon fully cooling of the Al flux, high molarity NaOH solution was used to etch the Al matrix to retrieve single crystals with naturally oriented faces. Crystals from this form of synthesis appear to be grown with several different morphologies: needles, plates, cubes, and bars. Crystals with a needle shaped morphology, small cross-sectional area compared to overall length (L/A ~$10mm^{-1}$) are ideal for thermal conductivity and strain experiments. SmB_6 crystals of this morphology have previously been shown withstand strain up to nearly 1.0%.[106]

Selected crystals are etched with 20% HCl solution for roughly 10 minutes to remove excess metal oxides as well as adsorbed gases such as water vapor, carbon dioxide, oxygen, and other gases present in air. This is a crucial step in creating contacts with low electrical contact resistance. Low resistance contacts provide ideal thermal contacts due to the additional electronic thermal transport between the crystal surface and the thermal lead. Though successful measurements have been performed using contacts with nearly 2KΩ of contact resistance[52].

We have explored additional surface treatments capable of improving the quality of these contacts. We found that an etch in a <1.0M $ZnCl_2$ solution dramatically improved the contact resistance. However, due to the open question regarding the role of Sm vacancies, and the dissolution of Sm in the Zn^{+2} solution, we thought it best to avoid this etch for this work. Future work on the chemical nature of samples with this zinc solution etch will be performed.

All contacts to the crystal surface along the naturally grown <100> face are constructed by EpoTek H20E conductive silver epoxy. Contacts are made using both silver and platinum wires for the thermal grounding contacts and heater/thermometer contacts, respectively. Contacts are cured in air at 80^{o}C for up to 3 hours to ensure a high degree of mechanical stability. These can be used for

either electrical or thermal transport through the crystal bulk allowing for verification or use of the Wiedemann-Franz Law to estimate the electronic contribution to thermal conductivity, which for samples discussed here is not expected to be significant until less than 1mK.

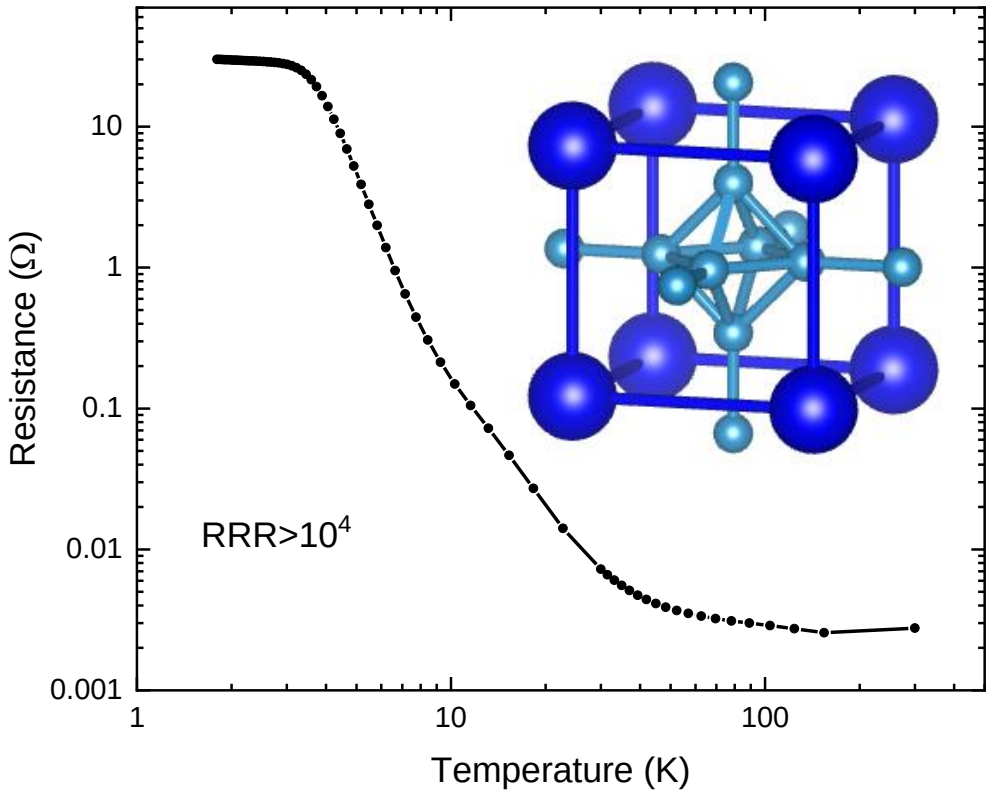

Figure 5.1: Temperature dependent resistance curve for flux grown single crystal of SmB_6 showing double activated behavior below 40K yielding to a resistance plateau below ~4K. Inset) Ball and stick model of SmB_6 *with Sm in dark blue and boron in light blue. Boron cage shows connections to nearest boron in adjacent cages.*

Three 25μm diameter Pt wires are used to establish contacts between the crystal and the single heater and two thermometers. These wires provide the flexibility required to work with such contacts, high electrical and thermal conductivity, as well as allowing for the construction of small contacts capable of decreasing contact size. This final point is crucial to the strained thermal transport experiment as the strained portion of the crystal is at largest 1mm, and desirably closer

to 0.5mm. Thermal grounding is provided by large 500 μm or 100μm (for smaller samples) thick silver wires epoxied in the same method as the aforementioned contacts. Neither silver nor platinum appear to create any additional contribution to contact resistance. These contacts regularly resulted in ~1KΩ resistance though with decreasing the time between the etch and contact placement has resulted in contact resistances less than 100Ω, an improvement over contact resistances reported on SmB_6.[52,53,102]

5.3 Thermal Transport Technique

The traditional steady state thermal transport technique is analogous to a 4-probe electrical resistance measurement. Two contacts are responsible for the injection of current or draining of current to electrical ground, while two other contacts are used in the measurement of the voltage drop. In the case of a thermal conductivity measurement, two contacts are required for the injection of a heat current and drain of that heat current to a thermal ground. Two more contacts are used to

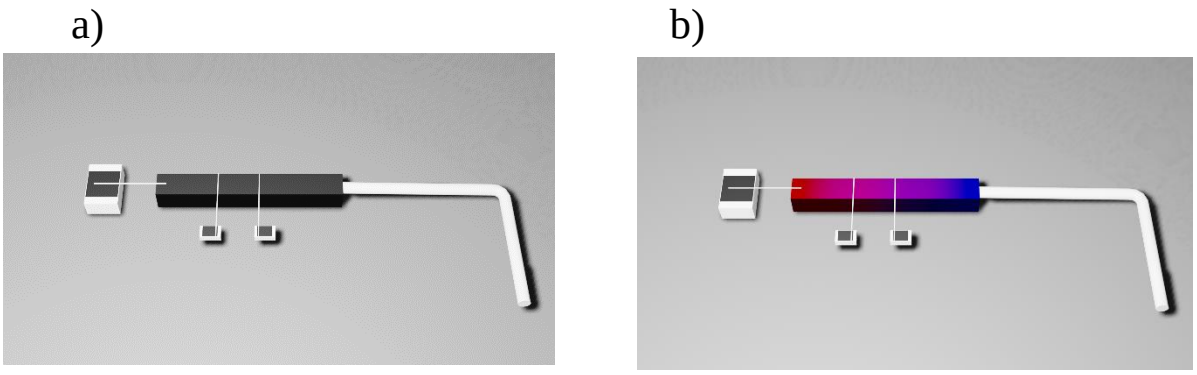

Figure 5.2: ***a)*** *Cartoon of traditional 4-point thermal conductivity experiment. Ohmic heater on the left is connected to the sample surface via silver wire. Two small Ohmic ruthenium oxide thermometers are connected for Pt wires at the center of the crystal. Large silver wire used as contact to thermal ground.* ***b)*** *Animation of the thermal gradient generated across the sample. Red and blue representing hot and cold, respectively.*

measure the temperature gradient across the sample. A diagram of such a set up can be seen below in Figure 5.2a. The resulting thermal gradient across the sample is animated in figure 5.2b.

These four contacts are then connected to thermal transport components, one 1KΩ metal film resistor, two 732Ω ruthenium oxide (ROX) thermometers. Finally, the thermal grounding wires mush be indium soldered to thermal ground. Thermal ground typically is chosen as a region of a cryostat with strong coupling to the coldest portion of the cryostat. In the case of the Oxford Instrument Dilution Refrigerator, a homemade sample stage that is thermally coupled to the Mixing Chamber will act as thermal ground. The surface of a Quantum Design ^{3}He Option puck acts as sufficient thermal ground. In each case, a thin piece of silver foil has been screwed into the available surface, onto which the large silver wire has been indium soldered to provide thermal contact. Indium solder is critical, particularly for measurements under 8K due to the superconducting transition of Pb/Sn solder and the relatively high quenching field required to re-establish strong thermal contact. Indium solder suits the needs of low temperature measurements due to the lower critical temperature and as such lower critical field required.

The steady state thermal conductivity procedure requires the application of heat from a resistor in a stepwise fashion, allowing at each increase in power, complete thermalization of the experiment. As such it is crucial to measure the thermometer response over a time interval that can include the initial response. The equilibration times provide information regarding the degree of thermal contact to thermal ground and can help in trouble shooting the experimental hardware. Lock-In Amplifier measurements for each thermometer are then averaged over a time window after complete thermalization in order to improve accuracy of the thermometer resistance measurement.

These conventional thermal transport experiments would typically require the sample to be suspended in vacuum to minimize parasitic heat loss to the surrounding environment. Both PPMS measurements and Dilution Refrigerator measurements can be performed at high vacuum due to cryopumping effects of radiation shields and charcoal sorption pumps. With proper care a thermal gradient across the crystal can be generated as depicted in Figure 2b.

However, strain measurements require the strong mechanical coupling of each sample end to the uniaxial strain cell[94,106–109]. These contacts are made on home-made spring steel washers using Stycast 2850 thermally conductive epoxy[93–95,106,109,109,110]. This epoxy has been shown by previous work[111] to perform well for a broad sample range in these uniaxial strain cells. Unfortunately, this sample geometry ensures a high degree of thermal contact of both ends to the strain cell, at odds with the thermal isolation requirements of thermal conductivity measurements.

To address this concern, a modified thermal conductivity geometry was created. This technique takes the traditional conductivity experiment and reflects it across the suspended end. A diagram can be seen in Figure 5.3. This design then allows for each end of the crystal to be thermally grounded by the same silver wires as the conventional measurement, while the heater is now placed at the center of the sample face. Two thermometers should then be mounted between the heater and a single thermally grounded end. If care is taken in constructing the contacts, the temperature gradient experienced across the crystal should be at a maximum at the center and will symmetrically decrease closer to the thermal grounding. As such, the heater should be placed in the center of the sample for most the reliable measurements. Deviations from this central position can be accounted for by a simple geometric argument that proportionally scales the heat current through each half of the crystal shown in equation 1.

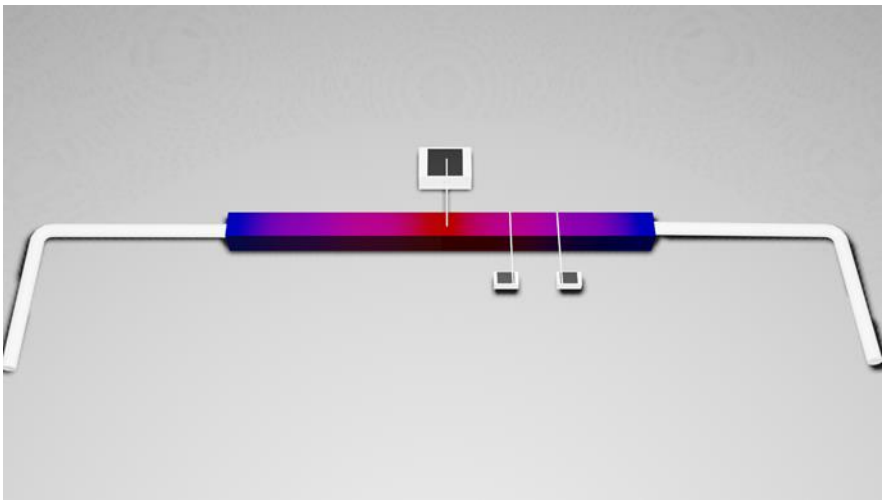

Figure 5.3: Schematic of Symmetrized thermal transport design shown with symmetric temperature gradient. Placement of the heater at the center of the crystal makes calculation of the thermal conductivity, or the heat current more specifically through the probed crystal portion, easier, though it is not required

.

$$\kappa = \frac{P}{\Delta T}\frac{L \quad L_2}{(L_1 + L_2)A} = \frac{P'}{\Delta T}\frac{L}{A} \tag{1}$$

This geometric scaling is in form of $L_2/(L_1+L_2)$, where L_1 and L_2 represent the distance between the heater and the left thermal grounding end and the right thermal grounding end. Here L still represents the separation between thermometers, P is the power dissipated across the heater, and ΔT is the thermal gradient. The second equality in equation 1 represents the traditional thermal transport equation with the newly scaled power dissipated. Of course, this formulation requires the experiment to be perfectly symmetric, apart from the heater placement. Thus, differences in the contact resistance between thermal grounding contacts should be considered for high precision calculations, though our data suggest that even naïve implementations of this formulation allow one to arrive at remarkably accurate results. A more careful formulation is provided in Section 5.4.

5.4 Symmetric thermal conductivity full estimate

The largest complication from the usage of the symmetric thermal transport design originates from the observation that heat current should pass through both halves of the crystal, the side being probed by the two ROX thermometers, and the side not monitored. Due to asymmetries in the experimental design, contact resistances, epoxy thickness, etc, it is not possible to know precisely how much of the applied heat current is passing through the probed sample portion. This uncertainty can lead to substantial error in the absolute value of $\kappa(T)$, though very likely the temperature and field dependence would be ultimately be altered. We can attempt to get a better estimate for the conductivity of the sample by considering an equivalent circuit model of the experimental geometry.

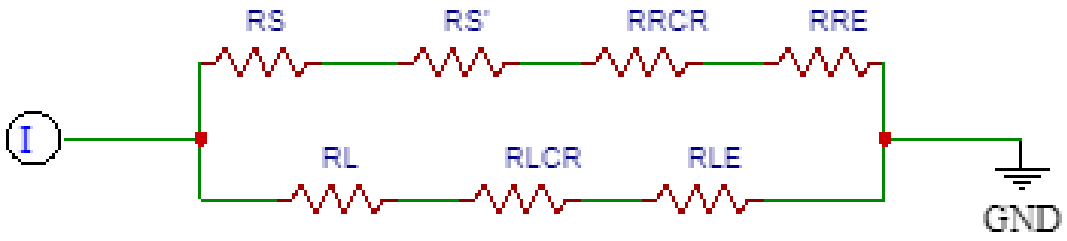

Figure 5.4: Parallel resistor model for the symmetrized thermal conductivity experiment. Current ,I, plays the role of the applied power, P. Note, that this model can likely be decoupled to describe systems with comparable electronic and phononic thermal conductivities. For the experiments on SmB_6 or other insulators, the electronic contact resistances R_{RCR}, R_{LCR} can likely be ignored until around 1mK.

A full derivation of the thermal conductivity of the associated parallel resistor model can be found in Appendix B. Recalling that in thermal conductivity experiments, total input heat power, P, plays the role of total current, I, temperature gradient ΔT plays the role of V_s. making these substitutions

leads to the final equation one can use to calculate the thermal conductivity in the symmetric thermal transport experiment.

$$\kappa = \frac{2P\frac{1}{A^2}l_s l_L}{-\left(R_{LC}P\frac{1}{A}l_s - \Delta T\frac{1}{A}(l_R + l_L)\right) \pm \sqrt{\left(\left(R_{LC}P\frac{1}{A}l_s - \Delta T\frac{1}{A}(l_R + l_L)\right)^2 - 4\left(P\frac{1}{A^2}l_s l_L\right)(-R_{RC}\Delta T)\right)}} \quad (2)$$

Equation 2 represents a more accurate estimate of the thermal conductivity of a sample measured in the symmetrized design. I would like to note here, however, that the R_{LC} and R_{RC} are no longer the electrical resistance, but the thermal resistance of these components. However, for the experiments presented in this work, a more naïve estimate using equation 1, or simply scaling the measured conductivity to the conventionally measured value has been performed on symmetrized experiments. This is in part due to the difficulty in providing good estimates for values, particularly the thermal contact resistance at the grounding ends. Additional work will be performed going forward in an attempt to better quantify these contributions.

5.5 Conventional and Symmetrized Thermal Transport

Preliminary measurements were performed in the traditional thermal transport geometry in order to confirm the quality of the samples from this batch of in house grown crystals. Thermal conductivity was measured above 1.8K in the Quantum Design PPMS under 0.1T applied field in order to quench any possible superconductivity present in the indium contacts. The peak at ~9K shown in Figure 5.5 is indicative of a thermal resistance cross-over between possible electron-phonon scattering and multi-phonon scattering channels[112]. Though I believe it is more likely that this cross over is more closely related to the onset of 3-phonon processes above 9K. The peak

height of this data is indicative of high sample quality as it is nearly 20% higher than data presented in literature.

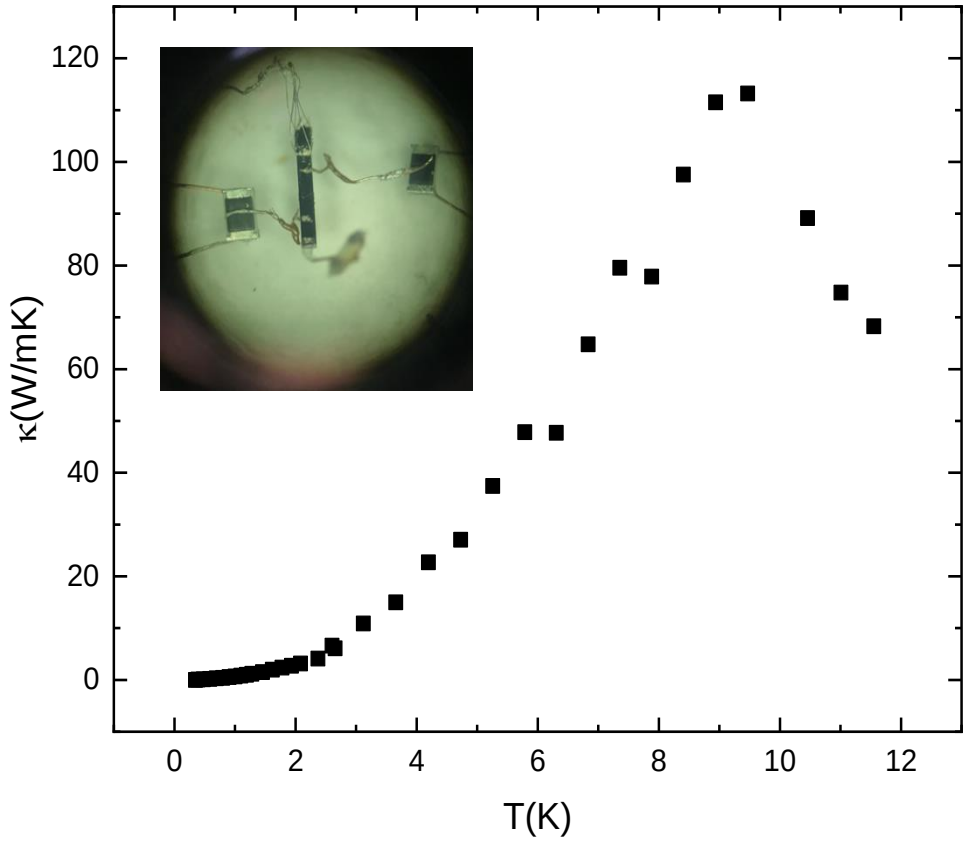

Figure 5.5: Thermal conductivity of single crystalline SmB_6 from 0.4K to 12K. The maximum in th conductivity is indicative of high sample quality and is a key feature in insulating crystals. Inset) crystal of SmB_6 with Pt wire contacts, one heater and two thermometers used for early measurem unstrained SmB_6.

Data below 1K are more critical for this experiment as it can unveil the nature of the low energy excitations in SmB_6. Below 1K we expect phonon-phonon scattering to be suppressed phonon population decreases.

Data in Figure 5.6a show the magnetic field and temperature dependence of thermal conductivity below 3K as taken in a Quantum Design He^3 probe down to roughly 400mK. Data at 0.1T

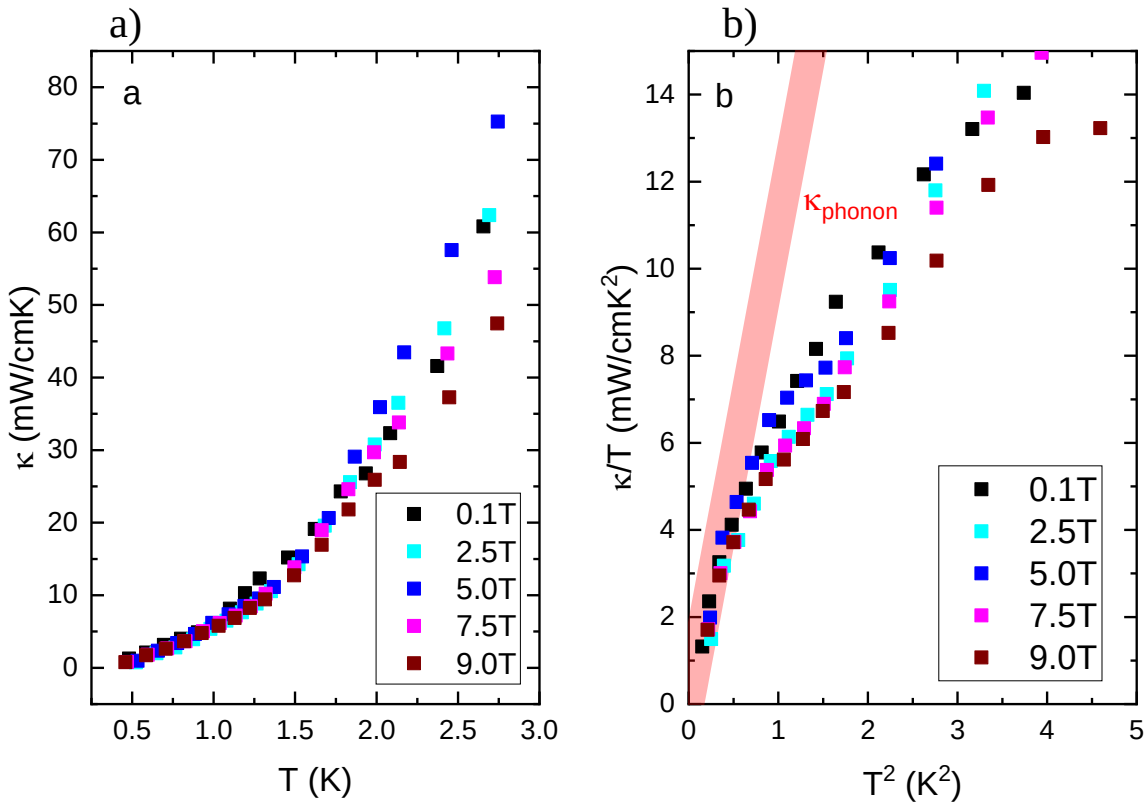

*Figure 5.6: **a)** Thermal conductivity of SmB_6 taken in He^3 refrigerator below 3K. Data show a non-monotonic behavior in the field dependence of conductivity. This had been attributed in previous studies as pertaining to a field induced scattering suppression. **b)** Thermal conductivity in figure a) plotted in k/T against T^2 with a modeled phonon gas curve in red. Low temperature compliance of data to the phonon gas suggests an absence of exotic fermionic excitation.*

reproduce the data taken with a base of 1.8K from the traditional 4K puck in the same cryostat. However, there is a clear non-monotonic behavior present induced by the magnetic field. Previous reports[52] have attributed this to a Schottky type anomaly for phonon scattering from magnetic moments present in the sample, however the magnetic field dependence in figure 5.6 appear to be much smaller than in previous work[52]. Estimates from previous work suggested this is due to J = 5/2 moment, likely caused by the Sm^{3+} ions in SmB_6. Figure 5.6b has been plotted with the inclusion of a theoretically calculated thermal conductivity for a noninteracting Bose gas, equation

3, with a mean free path limited by the sample dimensions, leading to the only phonon scattering being attributed to specular surface scattering, equation 4.[52]

$$k = \frac{2}{15}\pi^2 k_b \left(\frac{k_b T}{\hbar}\right)^3 c^{-2} l_0 * \tag{3}$$

$$l_0 = 2\sqrt[2]{\frac{A}{\pi}} \tag{4}$$

Estimates for the speed of sound, c, were calculated based on phonon velocities reported in literature.[52] The close agreement of the data below roughly 700mK and the calculated phonon conductivity indicates that at these temperatures, there is only evidence for a bosonic heat carrier. Previous reports[53] show that even above 400mK, signatures of a fermionic excitation could be observed under an applied field. However, measurements starting at 100mK would supply stronger evidence for fermionic excitations if observed in our samples.

Before proceeding to strained thermal transport measurements, it must first be confirmed that symmetrizing the thermal conductivity experiment, fixing both ends to the stage and applying heat at the center, does not in any serious way alter the qualitative behavior of κ(T). Such alterations may include changes to the temperature dependence or magnetic field dependence that would render such a measurement scheme useless for practical measurements.

As such, a single crystal of SmB_6 was prepared with 5 contacts as described earlier, three Pt wires for the heater and thermometer contacts, and two silver wires to provide contact to thermal ground. However, this sample was first measured in the "conventional" geometry in which heat is applied through a contact on one end, while the other is thermally anchored. As such, the dedicated wire centered on the crystal for the heater in the symmetric geometry is left floating. One can use the

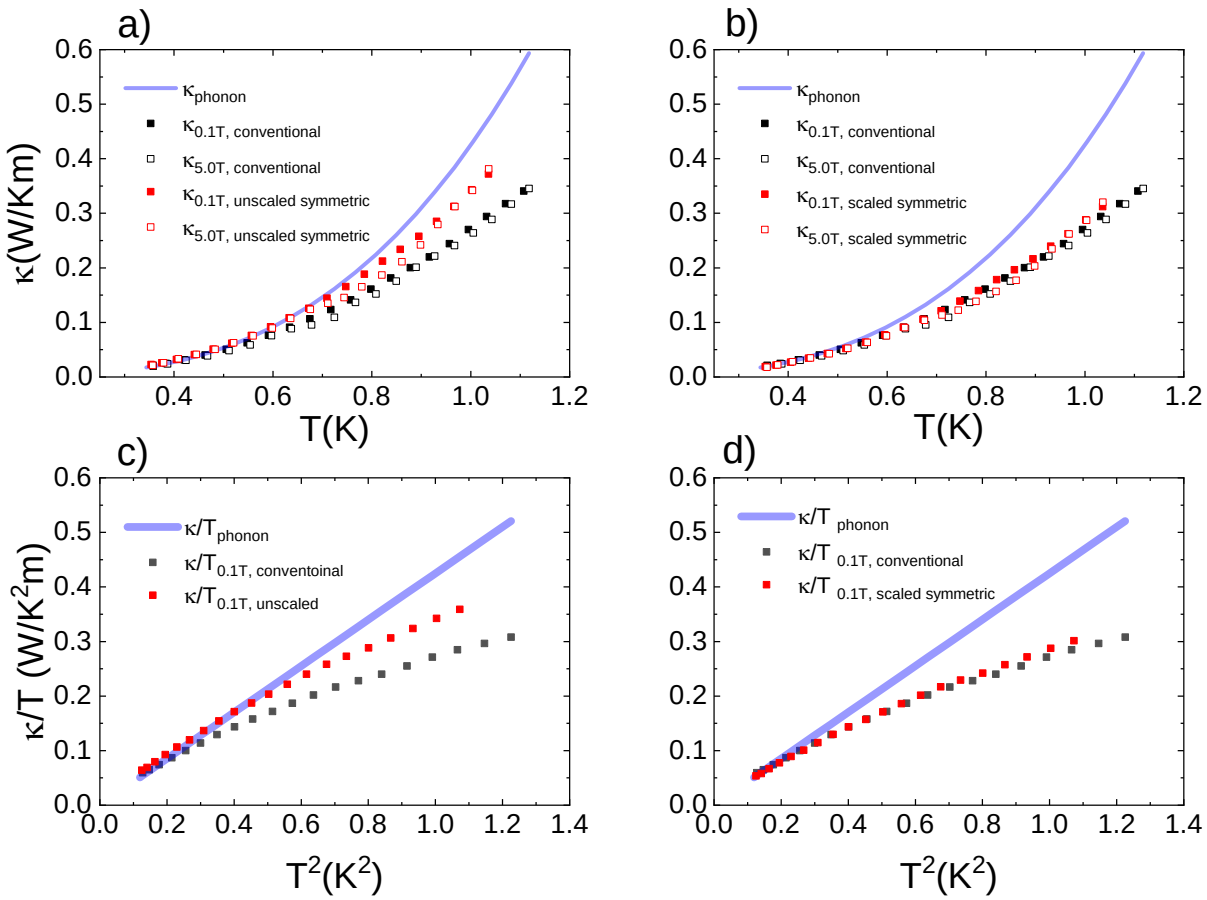

Figure 5.7: Testing of the symmetrized Thermal conductivity method. ***a)*** *Measurements of thermal conductivity of a new sample under both the conventional and symmetrized scheme. Note here that the symmetrized conductivity data is plotted here assuming all heat current generated passes through the probed half of the crystal.* ***b)*** *Identical data as in panel a), though the symmetrized data has been rescaled to account for the parallel current paths. Note here how well the symmetrized data collapses onto the conventional measurement data.* ***c),d)*** *Data from panel a), b) plotted as κ/T to more easily compare to the boundary scattering phonon conductivity.*

same thermometer contacts to measure the thermal conductivity in both a conventional and symmetric scheme.

Results of these measurements can be seen in Figure 5.7. Here, all black symbols are taken in the conventional measurement scheme. I should note that the opaque blue curve is the same boundary limited phonon scattering as used in Figure 5.5. Red symbols represent data taken in the symmetric set up. This data in panels a,c, are calculated assuming that all the heat current generated passes through the portion of the crystal being probed. Therefore, the thermal conductivity calculated in larger in the "unscaled" thermal conductivity in the symmetric design. In order to calculate the precise fraction of the heat current passing through the probed portion of the sample, the derived expression for κ may be used.

However, in practical situations, it is not easy to measure the contribution to thermal resistance to the contacts between the crystal and silver epoxy. Instead, I chose here to scale the data of the symmetric and conventional data at a single point and rescale all other points by that same scaling factor. As such, one can see near complete collapse of the curves on each other with only slight enhancement of κ at 5T. This suggests, as we believed, that the symmetrized thermal conductivity set up only complicates the measurement in that the precise value of the heat current can be challenging to determine, making a precise value of conductivity hard to determine. However, due to the relatively good agreement (even before scaling) of the conductivity, this technique continues to appear to be viable, despite the drawbacks.

For this sample, agreement between the calculated behavior and the filled data points appears lower than 500mK. This can more easily be seen in Figures 5.7c,d where κ/T is plotted against T^2. Though the agreement with pure boundary scattering of phonons occurs at lower temperatures than

in the previously mentioned sample, this is not out of line with what is expected from results in the literature[52], in which agreement was only seen below 200mK or lower.

With this confirmation of the ability to use the symmetrized thermal conductivity technique, proceeding to perform measurements in the uniaxial strain cell should be prudent.

5.6 Thermal Transport in Uniaxial Strain Cell

Confirming the absence of a fermionic excitation in unstrained flux grown SmB_6 samples we can grow, experiments involving strained thermal transport may begin. First, the sample was prepared as previously discussed with contacts in the symmetric sample geometry, Figure 5.3. This strain cell and all associated thermal transport components were loaded onto a home-built sample stage for the Oxford Instrument Dilution Refrigerator made of Teflon structural components and gold-plated annealed silver foil stage. The sample in the strain cell is then mounted to the Dilution Refrigerator stage can be seen in Figure 5.8a. The symmetrized thermal transport geometry is partially obscured by the black Stycast 28050 epoxy mounting the crystal to the steel washers. However, the noticeable feature should be the 3 epoxy contacts in the center of the roughly 1mm gap. It is within this region that the crystal itself will be strained and as such will be the only portion probed by thermal conductivity experiments in the strain cell. Contacts can more closely been seen in Figure 5.8b.

Thermal grounding to the SmB_6 crystal is established through silver wires indium soldered silver foil, which has been screwed into the sample stage. This allows for a high degree of thermal contact to the Mixing Chamber. Electrical leads for the heater and thermometers are made using coiled manganin wires, shown to be highly thermally insulating within the temperature range of interest. The addition of the black Stycast epoxy for sample mounting likely accounts for some small

additional thermal grounding, though weakly coupled to the stage through stainless steel washers and the titanium strain cell frame.

a) b)

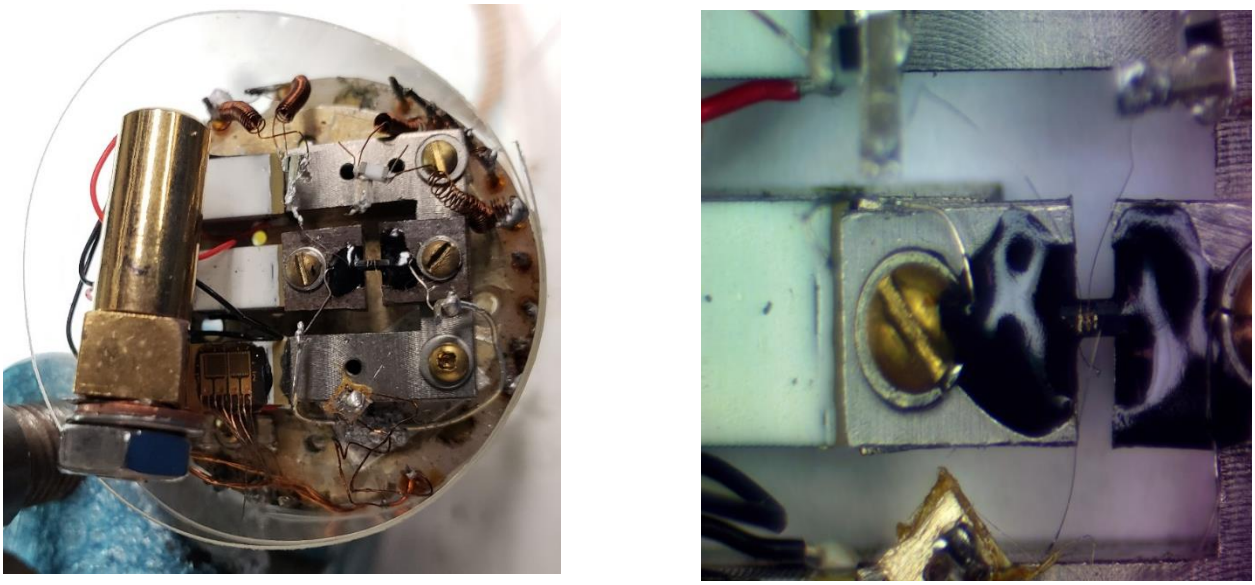

Figure5.8: Single crystal of SmB_6mounted to home-made Hicks style strain cell. ***a)*** *Strain cell shown with thermometer, transport thermometers and heater.* ***b)*** *Close up of 1mm gap between steel washers to highlight 3 handmade contacts for sample heater and thermometers. These contacts are on average 250micron in separation.*

Using the thermal transport set up as shown in Figure 5.8, we were able to perform unstrained thermal conductivity measurements to prove the validity of the symmetric thermal transport technique. Data taken with 0V piezoelectric bias show a qualitatively similar ~T^3 behavior as expected for an ideal electrically insulating single crystal, Figure 5.9a. However, in contrast to data taken in the Quantum Design PPMS in the traditional transport geometry, the data shown in Figure 5.9a lies in excess of the thermal conductivity of a surface limited phonon gas. Conductivity larger than the boson approximation for conductivity has previously been used as evidence of additional

thermal transport mechanisms, namely a charge neutral fermionic excitation.[53,102,103] However, when examining the conductivity as k/T as a function of T^2 as seen in figure 5.8b, the conductivity is well modeled by a linear fit, reinforcing the $\kappa \sim T^3$ behavior. The slope of this fit should match that of the phonon based calculation since the slope of these curves should be determined largely by fundamental constants as well as the sample dimensions, due to the specular scattering of phonons from the sample surface. For this reason, we believe that the difference between experimental and theoretical curves is likely due to the uncertainty in sample dimensions and contact separation. Due to the small contact separation between contacts (~250μm), the contact width of the same order of magnitude offers a large degree of error that propagates to the slope of the curve in Figure 5.9b. The absence of a clear residual linear conductivity offers no evidence for a fermionic excitation, in agreement with the unstrained data obtained down to 400mK in the QD PPMS in figures 5.6 and 5.7.

Actuating the piezoelectric stacks to the maximum displacement at 250V, I attempt to probe the emergence of this Fermi Surface. Our data suggests that within the strain applied to the sample under maximum piezo electric actuation, there appears to be no noticeable modification to the thermal conductivity of SmB_6 as seen in Figure 5.10. Though there is some expected change of the magnitude of thermal conductivity due to the deformation of the sample, as L/A is included in the calculation of conductivity, our experiments are insensitive to this.

Unfortunately, due to the Covid-19 outbreak and subsequent closure of the lab during much of my final months at UCI, I was unable to continue exploring the parameter space for this system. It is likely, that without the inclusion of a magnetic field, the signatures of the charge neutral fermions would be negligible, as was the case in the first observation.[53]

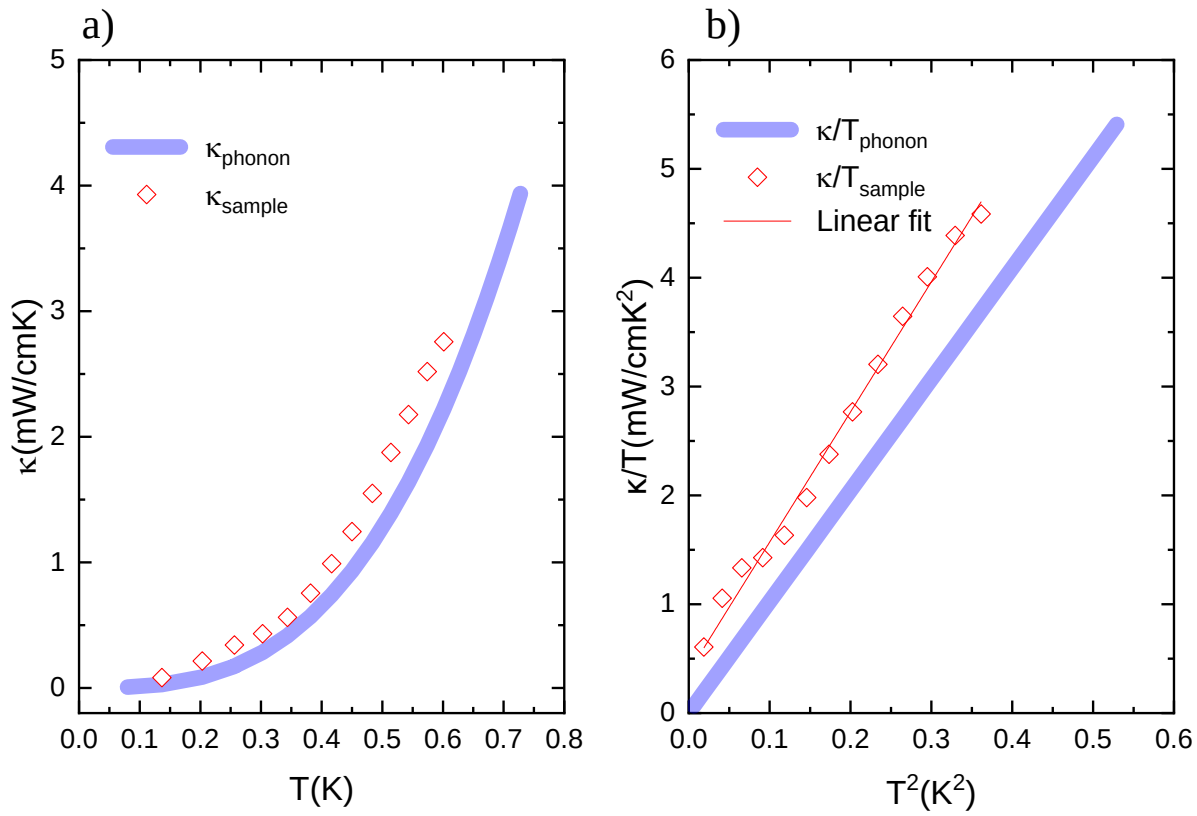

Figure 5.9: Dilution Refrigerator thermal transport measurements in uniaxial strain cell. ***a)*** *Both thermal conductivity of SmB_6 and theoretically predicted phonon curve appear in good agreement.* ***b)*** *Linear fit of temperature scaled thermal conductivity shows absence of fermionic excitation*

However, data presented in Figure 5.10 represent the first data set of any thermal conductivity under uniaxial strain. This unequivocally proves that the measurement is possible with the symmetrized thermal conductivity technique to temperatures as low as 100mK. The bonus of this technique is that it is easily extended to temperatures higher than 1K. Simple considerations for material choice for thermometers are likely to make the largest impact on this experiment. For instance, ROX thermometers should be changed out for diode thermometers for experiments optimized above 20K. Lead solder may be used in place of indium if experiments are performed in temperatures in excess of 9K, etc. The largest restriction for these experiments are represented by the physical size of the strain cell, the number of contacts requires for such experiments, and a clear way to thermally ground the sample.

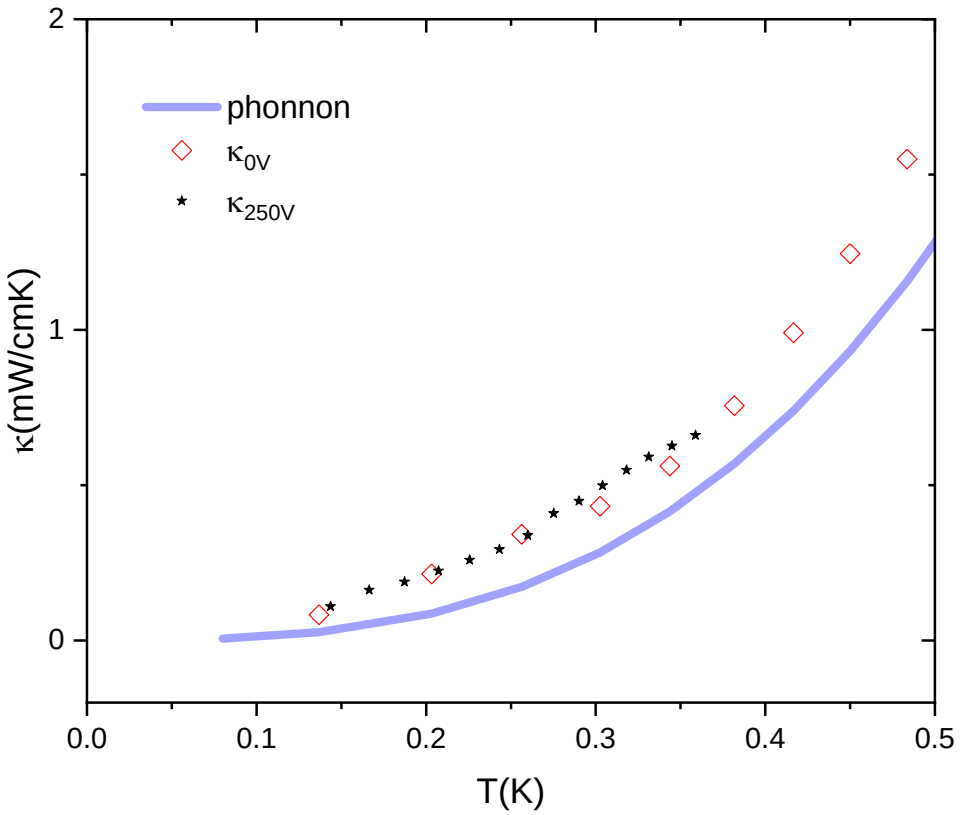

Figure 5.10: Unstrained and strained thermal conductivity. Data under both conductions show good agreement with phonon thermal conductivity.

5.7 Conclusion

Our work presented here has shown unambiguously that strained thermal conductivity experiments can be performed in a manner such that data is not only in qualitative but also good quantitative agreement with unstrained traditional measurements and theoretical descriptions. The symmetric thermal transport design can as such be extended to be used on other single crystalline or thin film samples under uniaxial strain.

The largest strain values presented in this work do not appear to be sufficient in order to observe a change in the low temperature excitations in SmB_6 and as such do not present any evidence for majorana-like fermions below 400mK.

Going further, samples with smaller cross-sectional area will be examined. These samples offer a two-fold benefit. First, thinner samples present less mechanical resistance to the piezoelectric actuation, meaning more strain can be applied. Second, thinner samples have a substantially smaller thermal conduction, leading to larger thermal gradients across the crystal making our experimental resolution less critical. Crystals of ideal size, that have already been grown, should allow for at least 200% increase in the thermal gradient for similar heater excitations.

In addition to using these thinner samples, the exploration of the behavior of conductivity under an applied external magnetic field is critical. Previously, evidence for a fermionic excitation is only available after applying a 5T field[53]. In fact, it may be critical to apply not only strain, but apply it in conjunction with uniaxial strain.

Chapter 6

Summary

In conclusion, though my time working at UCI has led to an increasingly varied subject matter, my main focus has remained on topological matter.

Early work focused on the characterization of a novel topological surface state based oscillator[57].This project required the measurement of a thermal oscillation, to lend credence to the proposed model for the aforementioned oscillations. These saw-tooth like oscillations in surface temperature of SmB_6 would lead to an alternation of surface and bulk dominated conduction, creating an oscillatory sample resistance giving rise to an oscillatory voltage.

This work utilized a standard chip based ROX thermometer, mounted directly to a crystal surface. This direct mounting was shown to thermally equilibrate on the time scale of milliseconds,

allowing for a reasonably good simultaneous measurement of the crystal voltage and temperature oscillation. Through the development of a novel signal processing script, the sub-noise oscillatory signal was recovered from electrical measurements of the thermometer. After calibrating the thermometer in-situ, these oscillations could be interpolated to show a temperature waveform for the crystal with high resolution. These waveforms were in good agreement with established theory[58]. Using a Fast Fourier Transformation on the raw thermometer voltage, resonant frequencies were extracted and found to be in reasonable agreement with the dependence on the applied current through the device.

Next work on strained topological matter took the form of two projects: strain induced anisotropy in FQH states, as well as the development of strained thermal transport technique to study bulk excitations in SmB_6.

For this work, the $\nu = 8/3,5/2,7/3$ states were examined under the influence of uniaxial strain as applied by the Hicks inspired piezoelectric based strain cell. The implicit symmetry breaking associated with uniaxial strain made the exploration for a Nematic state between the $\nu = 2,3$ IQH states rather attractive. Not only was an observed resistance anisotropy induced through the application of tensile strain, but the switching of the hard and easy axis, a feature seen in previous experiments at different fractional filling factors under field tilting, was a surprising feature. In addition to this hard axis switching, we were able to observe the continued survival of FQH signatures regardless of the applied uniaxial strain, making the observed state an anisotropic FQH, which had been only previously observed in[113] under field tilting. In addition to this exciting result, the emergence of a clear Landau Level dependence emerged showing that strain appears to affect the $\nu = 5/2$ state most strongly when applied in the N=1 LL. Some observation of nematicity was observed when strain is applied in the N=0LL at the $\nu = 3/2$ state, though with no obvious signature

of the FQH state. Furthermore, when applied at higher Landau Levels at $\nu = 5$, and at B=0T, there was no apparent effect of uniaxial strain. The complete invariance to strain in these Landau Levels creates an intriguing story that has yet to be theoretically fleshed out.

And finally, work on the strained thermal conductivity technique to probe the existence of a charge neutral fermi surface was somewhat daunting. Various technical difficulties involving three cryostats lead to the somewhat slow progress on this work. In addition to Covid-19 forcing closed the lab for three of my final six months, this experiment seemed doomed. However, throughout the course of this work, thermal conductivity, $\kappa(T)$ was measured on various crystal of SmB_6. Unstrained measurements on two samples of flux grown SmB_6 have shown little to no evidence for the charge neutral excitations as seen in previous works[102,103]. From here, a symmetrized thermal conductivity method was developed, in which a single heater contact would be placed in the crystal center along the <001> face and each end would have direct contact to the measurement stage, thermal ground. This resulted in a roughly symmetric temperature gradient that could be measured through the standard steady state method by two ROX thermometers.

Preliminary measurements of this technique in the dilution refrigerator show reasonably good agreement with a theoretical boundary limited phonon gas. We believe that deviation from this behavior was likely due to the large error in measuring contact separation, the size of which appears on the scale of the physical width of the contact itself. This implicit limitation in the sample preparation makes quantitative use of this technique somewhat limited, though the temperature dependence does not appear to be altered. This project will be adopted by another graduate student to probe the parameter space of strain-magnetic field-temperature, in search of this rich bulk SmB_6 physics.

Bibliography

1. Kardar, M. *Statistical Physics of Fields*. (Cambridge University Press, 2007). doi:10.1017/CBO9780511815881.
2. Ashcroft, N. W., Mermin, N. D. & Brooks/Cole Publishing Company. *Solid state physics*. (Brooks/Cole Cengage Learning Learning, 2018).
3. Pathria, R. K. & Beale, P. D. *Statistical mechanics*. (Elsevier/Academic Press, 2011).
4. Bardeen, J., Cooper, L. N. & Schrieffer, J. R. Theory of Superconductivity. *Phys. Rev.* **108**, 1175–1204 (1957).
5. Laughlin, R. B. Quantized Hall conductivity in two dimensions. *Phys. Rev. B* **23**, 5632–5633 (1981).
6. Thouless, D. J., Kohmoto, M., Nightingale, M. P. & den Nijs, M. Quantized Hall Conductance in a Two-Dimensional Periodic Potential. *Phys. Rev. Lett.* **49**, 405–408 (1982).
7. Carmo, M. P. do. *Differential geometry of curves and surfaces*. (Prentice-Hall, 1976).
8. Sakurai, J. J. & Napolitano, J. *Modern Quantum Mechanics*. (Cambridge University Press, 2017). doi:10.1017/9781108499996.
9. Baym, G. LECTURES ON QUANTUM MECHANICS. 6.
10. Bernevig, B. A. *Topological Insulators and Topological Superconductors*. (Princeton University Press, 2013). doi:10.1515/9781400846733.
11. Stormer, H. L., Laboratories, B., Tsui, D. C. & Gossard, A. C. The fractional quantum Hall effect. *Rev Mod Phys* **71**, 8 (1999).
12. Halperin, B. I. Quantized Hall conductance, current-carrying edge states, and the existence of extended states in a two-dimensional disordered potential. *Phys. Rev. B* **25**, 2185–2190 (1982).
13. Jackiw, R. & Rebbi, C. Solitons with fermion number \textonehalf{}. *Phys. Rev. D* **13**, 3398–3409 (1976).
14. Su, W. P., Schrieffer, J. R. & Heeger, A. J. Solitons in Polyacetylene. *Phys. Rev. Lett.* **42**, 1698–1701 (1979).
15. von Klitzing, K. Developments in the quantum Hall effect. *Philos. Trans. R. Soc. Math. Phys. Eng. Sci.* **363**, 2203–2219 (2005).
16. Hasan, M. Z. & Kane, C. L. *Colloquium* : Topological insulators. *Rev. Mod. Phys.* **82**, 3045–3067 (2010).

17. Tsui, D. C., Stormer, H. L. & Gossard, A. C. Two-Dimensional Magnetotransport in the Extreme Quantum Limit. *Phys. Rev. Lett.* **48**, 1559–1562 (1982).
18. Laughlin, R. B. Anomalous Quantum Hall Effect: An Incompressible Quantum Fluid with Fractionally Charged Excitations. *Phys. Rev. Lett.* **50**, 1395–1398 (1983).
19. Kane, C. L. & Mele, E. J. Quantum Spin Hall Effect in Graphene. *Phys. Rev. Lett.* **95**, 226801 (2005).
20. Bernevig, B. A. & Zhang, S.-C. Quantum Spin Hall Effect. *Phys. Rev. Lett.* **96**, 106802 (2006).
21. Bernevig, B. A., Hughes, T. L. & Zhang, S.-C. Quantum Spin Hall Effect and Topological Phase Transition in HgTe Quantum Wells. *Science* **314**, 1757–1761 (2006).
22. Konig, M. *et al.* Quantum Spin Hall Insulator State in HgTe Quantum Wells. *Science* **318**, 766–770 (2007).
23. Wu, C., Bernevig, B. A. & Zhang, S.-C. Helical Liquid and the Edge of Quantum Spin Hall Systems. *Phys. Rev. Lett.* **96**, 106401 (2006).
24. Roy, R. Z 2 classification of quantum spin Hall systems: An approach using time-reversal invariance. *Phys. Rev. B* **79**, 195321 (2009).
25. Moore, J. E. & Balents, L. Topological invariants of time-reversal-invariant band structures. *Phys. Rev. B* **75**, 121306 (2007).
26. Fu, L., Kane, C. L. & Mele, E. J. Topological Insulators in Three Dimensions. *Phys. Rev. Lett.* **98**, 106803 (2007).
27. Dzero, M., Xia, J., Galitski, V. & Coleman, P. Topological Kondo Insulators. *Annu. Rev. Condens. Matter Phys.* **7**, 249–280 (2016).
28. Dzero, M., Sun, K., Galitski, V. & Coleman, P. Topological Kondo Insulators. *Phys. Rev. Lett.* **104**, 106408 (2010).
29. Allen, J. W., Batlogg, B. & Wachter, P. Large low-temperature Hall effect and resistivity in mixed-valent Sm B 6. *Phys. Rev. B* **20**, 4807–4813 (1979).
30. Cooley, J. C., Aronson, M. C., Fisk, Z. & Canfield, P. C. Sm B 6 : Kondo Insulator or Exotic Metal? *Phys. Rev. Lett.* **74**, 1629–1632 (1995).
31. Fisk, Z. *et al.* Kondo insulators. *Phys. B Condens. Matter* **223–224**, 409–412 (1996).
32. Menth, A., Buehler, E. & Geballe, T. H. Magnetic and Semiconducting Properties of Sm${\mathrm{B}}_{6}$. *Phys. Rev. Lett.* **22**, 295–297 (1969).

33. Fisk, Z. *et al.* Kondo insulators. *Phys. B Condens. Matter* **206–207**, 798–803 (1995).

34. Phelan, W. A. *et al.* On the Chemistry and Physical Properties of Flux and Floating Zone Grown SmB6 Single Crystals. *Sci. Rep.* **6**, 20860 (2016).

35. Kim, D. J. *et al.* Surface Hall Effect and Nonlocal Transport in SmB6: Evidence for Surface Conduction. *Sci. Rep.* **3**, 3150 (2013).

36. Sluchanko, N. E. *et al.* Intragap states in SmB 6. *Phys. Rev. B* **61**, 9906–9909 (2000).

37. Jiang, J. *et al.* Observation of possible topological in-gap surface states in the Kondo insulator SmB6 by photoemission. *Nat. Commun.* **4**, 3010 (2013).

38. Neupane, M. *et al.* Surface electronic structure of the topological Kondo-insulator candidate correlated electron system SmB6. *Nat. Commun.* **4**, 2991 (2013).

39. Xu, N. *et al.* Direct observation of the spin texture in SmB6 as evidence of the topological Kondo insulator. *Nat. Commun.* **5**, 4566 (2014).

40. Kim, D. J., Xia, J. & Fisk, Z. Topological surface state in the Kondo insulator samarium hexaboride. *Nat. Mater.* **13**, 466–470 (2014).

41. Kim, J. *et al.* Electrical detection of the surface spin polarization of the candidate topological Kondo insulator SmB6. *Phys. Rev. B* **99**, 245148 (2019).

42. Pirie, H. *et al.* Imaging emergent heavy Dirac fermions of a topological Kondo insulator. *Nat. Phys.* **16**, 52-+ (2020).

43. Li, T. *et al.* Nontrivial Nature and Penetration Depth of Topological Surface States in SmB6 Thin Films. *Phys. Rev. Lett.* **120**, 207206 (2018).

44. Jiao, L. *et al.* Magnetic and defect probes of the SmB6 surface state. *Sci. Adv.* **4**, eaau4886 (2018).

45. Li, G. *et al.* Two-dimensional Fermi surfaces in Kondo insulator SmB6. *Science* **346**, 1208–1212 (2014).

46. Tan, B. S. *et al.* Unconventional Fermi surface in an insulating state. *Science* **349**, 287–290 (2015).

47. Zhang, X. *et al.* Hybridization, Inter-Ion Correlation, and Surface States in the Kondo Insulator SmB6. *Phys. Rev. X* **3**, 011011 (2013).

48. Konovalova, E. S. *et al.* Effect of vacancies and foreign metal ions on the valent state of samarium in SmB6. *Sov. Powder Metall. Met. Ceram.* **21**, 820–823 (1982).

49. Rao, P. & Sodemann, I. Cyclotron resonance inside the Mott gap: A fingerprint of emergent neutral fermions. *Phys. Rev. B* **100**, 155150 (2019).

50. Chowdhury, D., Sodemann, I. & Senthil, T. Mixed-valence insulators with neutral Fermi surfaces. *Nat. Commun.* **9**, 1766 (2018).

51. Sodemann, I., Chowdhury, D. & Senthil, T. Quantum oscillations in insulators with neutral Fermi surfaces. *Phys. Rev. B* **97**, 045152 (2018).

52. Boulanger, M.-E. *et al.* Field-dependent heat transport in the Kondo insulator SmB6: Phonons scattered by magnetic impurities. *Phys. Rev. B* **95**, 245141 (2018).

53. Hartstein, M. *et al.* Fermi surface in the absence of a Fermi liquid in the Kondo insulator SmB6. *Nat. Phys.* **14**, 166-+ (2018).

54. Robinson, P. J. *et al.* Dynamical Bonding Driving Mixed Valency in a Metal Boride. *Angew. Chem. Int. Ed.* **n/a**,.

55. Stern, A., Dzero, M., Galitski, V. M., Fisk, Z. & Xia, J. Surface-dominated conduction up to 240 K in the Kondo insulator SmB 6 under strain. **16**, 708–712 (2017).

56. Kim, D. J., Grant, T. & Fisk, Z. Limit Cycle and Anomalous Capacitance in the Kondo Insulator SmB 6. *Phys. Rev. Lett.* **109**, 096601 (2012).

57. Stern, A., Efimkin, D. K., Galitski, V., Fisk, Z. & Xia, J. Radio Frequency Tunable Oscillator Device Based on a SmB6 Microcrystal. *Phys. Rev. Lett.* **116**, 166603 (2016).

58. Casas, B., Stern, A., Efimkin, D. K., Fisk, Z. & Xia, J. Direct observation of surface-state thermal oscillations in SmB6 oscillators. *Phys. Rev. B* **97**, 035121 (2018).

59. Canfield, P. C. New materials physics. *Rep. Prog. Phys.* **83**, 016501 (2020).

60. Canfield, P. C. & Fisk, Z. Growth of single crystals from metallic fluxes. *Philos. Mag. B* **65**, 1117–1123 (1992).

61. Fisk, Z. & Remeika, J. P. Chapter 81 Growth of single crystals from molten metal fluxes. in *Handbook on the Physics and Chemistry of Rare Earths* vol. 12 53–70 (Elsevier, 1989).

62. Zachary Fisk. https://www.aip.org/history-programs/niels-bohr-library/oral-histories/44382 (2020).

63. Kelton, K. & Greer, A. L. *Nucleation in Condensed Matter: Applications in Materials and Biology*. (Elsevier, 2010).

64. Lutsko, J. F. How crystals form: A theory of nucleation pathways. *Sci. Adv.* **5**, eaav7399 (2019).

65. Karthika, S., Radhakrishnan, T. K. & Kalaichelvi, P. A Review of Classical and Nonclassical Nucleation Theories. *Cryst. Growth Des.* **16**, 6663–6681 (2016).

66. Karthika, S., Radhakrishnan, T. K. & Kalaichelvi, P. A Review of Classical and Nonclassical Nucleation Theories. *Cryst. Growth Des.* **16**, 6663–6681 (2016).

67. Sachdev, S. *Quantum Phase Transitions*. (Cambridge University Press, 2011). doi:10.1017/CBO9780511973765.

68. Pobell, F. *Matter and methods at low temperatures*. (Springer, 2007).

69. Berman, R. *Thermal Conduction in Solids*. (Clarendon Press, 1976).

70. Wolgast, S. *et al.* Low-temperature surface conduction in the Kondo insulator SmB6. *Phys. Rev. B* **88**, 180405 (2013).

71. Dzero, M., Sun, K., Coleman, P. & Galitski, V. Theory of topological Kondo insulators. *Phys. Rev. B* **85**, 045130 (2012).

72. Alexandrov, V., Dzero, M. & Coleman, P. Cubic Topological Kondo Insulators. *Phys. Rev. Lett.* **111**, 226403 (2013).

73. Lu, F., Zhao, J., Weng, H., Fang, Z. & Dai, X. Correlated Topological Insulators with Mixed Valence. *Phys. Rev. Lett.* **110**, 096401 (2013).

74. Nakajima, Y., Syers, P., Wang, X., Wang, R. & Paglione, J. One-dimensional edge state transport in a topological Kondo insulator. *Nat. Phys.* **12**, 213–217 (2016).

75. Biswas, P. K. *et al.* Suppression of magnetic excitations near the surface of the topological Kondo insulator SmB6. *Phys. Rev. B* **95**, 020410 (2017).

76. Xu, K.-J. *et al.* Metallic surface states in a correlated d-electron topological Kondo insulator candidate FeSb2. *Proc. Natl. Acad. Sci.* **117**, 15409–15413 (2020).

77. Lilly, M. P., Cooper, K. B., Eisenstein, J. P., Pfeiffer, L. N. & West, K. W. Evidence for an Anisotropic State of Two-Dimensional Electrons in High Landau Levels. (1999).

78. Stern, A. Non-Abelian states of matter. **464**, 187–193 (2010).

79. Pfeiffer, L. *et al.* Formation of a high quality two-dimensional electron gas on cleaved GaAs. **1697**, 2–5 (2001).

80. Eisenstein, J. P., Boebinger, G. S., Pfeiffer, L. N., West, K. W. & He, S. New Fractional Quantum Hall State in Double-Layer Two-Dimensional Electron Systems. **68**, 68–71 (1992).

81. Eisenstein, J. P., Cooper, K. B., Pfeiffer, L. N. & West, K. W. Insulating and Fractional Quantum Hall States in the First Excited Landau Level. 2–5 (2002) doi:10.1103/PhysRevLett.88.076801.

82. Eisenstein, J. P., Stormer, H. L., Pfeiffer, L. & West, K. W. Evidence for a Phase Transition in the Fractional Quantum Hall Effect. **62**, (1989).

83. Eisenstein, J. P., Stormer, H. L., Pfeiffer, L. N. & West, K. W. Evidence for a spin transition in the v=2/3 fractional quantum Hall effect. **41**, 7910–7913 (1990).

84. Xia, J., Eisenstein, J. P., Pfeiffer, L. N. & West, K. W. Evidence for a fractionally quantized Hall state with anisotropic longitudinal transport. *Nat. Phys.* **7**, 845–848 (2011).

85. Willett, R. *et al.* Observation of an Even-Denominator Quantum Number in the Fractional Quantum Hall Effect. **59**, 1776–1779 (1987).

86. Pollanen, J. *et al.* Heterostructure symmetry and the orientation of the quantum Hall nematic phases. *Phys. Rev. B - Condens. Matter Mater. Phys.* **92**, 1–9 (2015).

87. Lilly, M. P., Cooper, K. B., Eisenstein, J. P., Pfeiffer, L. N. & West, K. W. Anisotropic States of Two-Dimensional Electron Systems in High Landau Levels : Effect of an In-Plane Magnetic Field. (1999).

88. Xia, J., Cvicek, V., Eisenstein, J. P., Pfeiffer, L. N. & West, K. W. Tilt-induced anisotropic to isotropic phase transition at v=5/2. *Phys. Rev. Lett.* **105**, 1–4 (2010).

89. Samkharadze, N. *et al.* Observation of a transition from a topologically ordered to a spontaneously broken symmetry phase. *Nat. Phys.* **12**, 191–195 (2016).

90. Schreiber, K. A. *et al.* Onset of quantum criticality in the topological-to-nematic transition in a two-dimensional electron gas at filling factor ν = 5 / 2. **041107**, 5–9 (2017).

91. Cooper, K. B. *et al.* Metastable Resistance-Anisotropy Orientation of Two-Dimensional Electrons in High Landau Levels. **1**, 1–4 (2004).

92. Pollanen, J., Eisenstein, J. P., Pfeiffer, L. N. & West, K. W. Charge metastability and hysteresis in the quantum Hall regime. **245440**, 1–7 (2016).

93. Hicks, C. W., Barber, M. E., Edkins, S. D., Brodsky, D. O. & Mackenzie, A. P. Piezoelectric-based apparatus for strain tuning. *Rev. Sci. Instrum.* **85**, 1–8 (2014).

94. Steppke, A. *et al.* Strong peak in T. **9398**, (2017).

95. Hicks, C. W. *et al.* Strong Increase of. **344**, 283–286 (2014).

96. Bishop, N. C. *et al.* Valley Polarization and Susceptibility of Composite Fermions around a Filling Factor ˆ 3. **266404**, 1–4 (2007).

97. Koduvayur, S. P. *et al.* Effect of Strain on Stripe Phases in the Quantum Hall Regime. **016804**, 2–5 (2011).

98. Padmanabhan, M., Gokmen, T. & Shayegan, M. Density dependence of valley polarization energy for composite fermions. 1–5 (2009) doi:10.1103/PhysRevB.80.035423.

99. Padmanabhan, M., Gokmen, T. & Shayegan, M. Ferromagnetic Fractional Quantum Hall States in a Valley-Degenerate Two-Dimensional Electron System. **016805**, 1–4 (2010).

100. Fradkin, E., Kivelson, S. A., Lawler, M. J. & Mackenzie, A. P. Nematic Fermi Fluids in Condensed Matter Physics Further. (2010) doi:10.1146/annurev-conmatphys-070909-103925.

101. Utsumi, Y. *et al.* Bulk and surface electronic properties of SmB6: A hard x-ray photoelectron spectroscopy study. *Phys. Rev. B* **96**, 155130 (2017).

102. Tan, B. S. *et al.* Unconventional Fermi surface in an insulating state. *Science* **349**, 287–290 (2015).

103. Liu, H. *et al.* Fermi surfaces in Kondo insulators. *J. Phys.-Condens. Matter* **30**, 16LT01 (2018).

104. Thomas, S. M. *et al.* Quantum Oscillations in Flux-Grown SmB6 with Embedded Aluminum. *Phys. Rev. Lett.* **122**, 166401 (2019).

105. Eo, Y. S. *et al.* Transport gap in SmB6 protected against disorder. *Proc. Natl. Acad. Sci. U. S. A.* **116**, 12638–12641 (2019).

106. Stern, A., Dzero, M., Galitski, V. M., Fisk, Z. & Xia, J. Surface-dominated conduction up to 240 K in the Kondo insulator SmB6 under strain. *Nat. Mater.* **16**, 708-+ (2017).

107. Hicks, C. W., Barber, M. E., Edkins, S. D., Brodsky, D. O. & Mackenzie, A. P. Piezoelectric-based apparatus for strain tuning. *Rev. Sci. Instrum.* **85**, 065003 (2014).

108. Hicks, C. W. *et al.* Strong Increase of Tc of Sr2RuO4 Under Both Tensile and Compressive Strain. *Science* **344**, 283–285 (2014).

109. Barber, M. E. *et al.* Role of correlations in determining the Van Hove strain in Sr2RuO4. *Phys. Rev. B* **100**, 245139 (2019).

110. Brodsky, D. O. *et al.* Strain and vector magnetic field tuning of the anomalous phase in Sr3Ru2O7. *Sci. Adv.* **3**, e1501804 (2017).

111. Barber, M. E. Uniaxial Stress Technique and Investigations into Correlated Electron Systems. 198.

112. Flachbart, K. *et al.* Thermal conductivity of SmB6. *J. Common Met.* **88**, L11–L14 (1982).

113. Xia, J., Cvicek, V., Eisenstein, J. P., Pfeiffer, L. N. & West, K. W. Tilt-Induced Anisotropic to Isotropic Phase Transition at ν = 5 / 2. *Phys. Rev. Lett.* **105**, 176807 (2010).

Appendix A: Copyright

American Physical Society Reuse and Permissions License

05-Feb-2020

This license agreement between the American Physical Society ("APS") and Brian Casas ("You") consists of your license details and the terms and conditions provided by the American Physical Society and SciPris.

Licensed Content Information

License Number:	**RNP/20/FEB/022546**
License date:	05-Feb-2020
DOI:	10.1103/PhysRevB.97.035121
Title:	Direct observation of surface-state thermal oscillations in ${\mathrm{SmB}}_{6}$ oscillators
Author:	Brian Casas et al.
Publication:	Physical Review B
Publisher:	American Physical Society
Cost:	USD $ 0.00

Request Details

Does your reuse require significant modifications: No

Specify intended distribution locations:	Worldwide
Reuse Category:	Reuse in a thesis/dissertation
Requestor Type:	Author of requested content
Items for Reuse:	Whole Article
Format for Reuse:	Electronic

Information about New Publication:

University/Publisher:	University of California Irvine
Title of dissertation/thesis:	Electrical and Thermal Transport Studies on Topologically Non-Trivial Systems
Author(s):	Brian W Casas
Expected completion date:	Jun. 2020

License Requestor Information

Name:	Brian Casas
Affiliation:	Individual
Email Id:	bcasas1@uci.edu
Country:	United States

Copyright Clearance Center Marketplace™

Annual Reviews, Inc. - License Terms and Conditions

This is a License Agreement between Brian W Casas ("You") and Annual Reviews, Inc. ("Publisher") provided by Copyright Clearance Center ("CCC"). The license consists of your order details, the terms and conditions provided by Annual Reviews, Inc., and the CCC terms and conditions.

All payments must be made in full to CCC.

Order Date	09-Aug-2020	**Type of Use**	Republish in a thesis/dissertation
Order license ID	1054332-1		
ISSN	1947-5462	**Publisher**	Annual Reviews
		Portion	Cartoon

LICENSED CONTENT

Publication Title	Annual review of condensed matter physics	**Rightsholder**	Annual Reviews, Inc.
		Publication Type	Journal
Date	12/31/2009	**URL**	http://www.annualreviews.org/journal/conmatphys
Language	English		
Country	United States of America		

REQUEST DETAILS

Portion Type	Cartoon	**Distribution**	Worldwide
Number of cartoons	1	**Translation**	Original language of publication
Format (select all that apply)	Electronic	**Copies for the disabled?**	No
Who will republish the content?	Academic institution	**Minor editing privileges?**	No
Duration of Use	Life of current and all future editions	**Incidental promotional use?**	No
Lifetime Unit Quantity	Up to 499	**Currency**	USD
Rights Requested	Main product		

American Physical Society
Reuse and Permissions License

09-Aug-2020

This license agreement between the American Physical Society ("APS") and Brian Casas ("You") consists of your license details and the terms and conditions provided by the American Physical Society and SciPris.

Licensed Content Information

License Number:	**RNP/20/AUG/029356**
License date:	09-Aug-2020
DOI:	10.1103/PhysRevLett.116.166603
Title:	Radio Frequency Tunable Oscillator Device Based on a ${\mathrm{SmB}}_{6}$ Microcrystal
Author:	Alex Stern et al.
Publication:	Physical Review Letters
Publisher:	American Physical Society
Cost:	USD $ 0.00

Request Details

Does your reuse require significant modifications: No

Specify intended distribution locations:	Worldwide
Reuse Category:	Reuse in a thesis/dissertation
Requestor Type:	Student
Items for Reuse:	Figures/Tables
Number of Figure/Tables:	1
Figure/Tables Details:	Figure 1a), scematic of oscillator device, SEM picture and Output as a function of time.
Format for Reuse:	Electronic

Information about New Publication:

University/Publisher:	University of California, irvine
Title of dissertation/thesis:	Electronic and Thermal Transport Studies of Topologically Non-Trivial Systems
Author(s):	Brian W Casas
Expected completion date:	Aug. 2020

License Requestor Information

Name:	Brian Casas
Affiliation:	Individual
Email Id:	bcasas1@uci.edu
Country:	United States

American Physical Society
Reuse and Permissions License

09-Aug-2020

This license agreement between the American Physical Society ("APS") and Brian Casas ("You") consists of your license details and the terms and conditions provided by the American Physical Society and SciPris.

Licensed Content Information

License Number:	**RNP/20/AUG/029349**
License date:	09-Aug-2020
DOI:	10.1103/RevModPhys.82.3045
Title:	Colloquium: Topological insulators
Author:	M. Z. Hasan and C. L. Kane
Publication:	Reviews of Modern Physics
Publisher:	American Physical Society
Cost:	USD $ 0.00

Request Details

Does your reuse require significant modifications: No

Specify intended distribution locations:	United States
Reuse Category:	Reuse in a thesis/dissertation
Requestor Type:	Student
Items for Reuse:	Figures/Tables
Number of Figure/Tables:	2
Figure/Tables Details:	Figures 2 and 5 showing the band structure cartoon of the Quantum Hall and Spin Hall effects respectively.
Format for Reuse:	Electronic

Information about New Publication:

University/Publisher:	University of California, Irvine
Title of dissertation/thesis:	Electrical and Thermal Transport Studies on Topologically Non-Trivial Systems
Author(s):	Brian W Casas
Expected completion date:	Sep. 2020

License Requestor Information

Name:	Brian Casas
Affiliation:	Individual
Email Id:	bcasas1@uci.edu
Country:	United States

Appendix B: Symmetrized thermal conductivity estimate

Taking all resistors in the parallel resistor model in figure 5.4 to be unique in value, we can go ahead and solve this model for R_s, the resistance of the measured portion of crystal.

$$R_{TL} \neq R_{TR}, R_{RC} \neq R_{LC} \neq 0 \quad (1)$$

As such, I have treated the problem by considering an equivalent circuit schematic in which a total current, I, is injected into a set of parallel resistors with branches for the left, L, and right, R, side of the crystal. Here we consider the transport thermometers to be measuring a gradient across a portion of the right half of the crystal. The branch depicting the right portion of the crystal can be modeled by four resistors, R_s, $R_{s'}$, R_{RCR}, R_{RE}, labeling the measured portion of the sample, the unmeasured portion of the sample, the contact resistance, and the resistance of the H20E silver epoxy, respectively. For simplicity I have relabeled the sum of the contact resistance and the silver epoxy resistance in a single term, $R_{(R,L)C}$, for the contact.

$$R_{LC} = R_{LCR} + R_{LE} \quad (2)$$

$$R_{RC} = R_{RCR} + R_{RE} \quad (3)$$

$$R_{TR} = R_s + R_{s'} + R_{RC} \quad (4)$$

$$R_{TL} = R_L + R_{LC} \quad (5)$$

Due to the lack of guaranteed symmetry, I consider a scenario in which none of the above quantities are identical, though I do assume that the conductivity, ρ, is consistent across the entire length of the crystal.

Since the only measured quantity in the experiment is ΔT, in analogy to V_s in the circuit, I attempt to solve for the resistivity of the resistors R_s, $R_{s'}$, R_L, in terms of the contact resistances $R_{(R,L)C}$, total current I, and the differential potential V_s.

Due to the parallel arrangement of the right and left branches, I take the total current I, to be simply the sum of current through the right and left halves of the experiment.

$$I = I_R + I_L \tag{6}$$

Since I can only accurately measure the total current I in the system, I will choose to leave it in my final expression wherever possible. Additionally, while there is a V_{Total} that should be identical across both branches, I do not choose to include it in my final result as it is not a quantity I actively measure. Doing so would require a measurement of the heater temperature and the temperature of the stage, the former of which I do not record.

Calculating the resistance R_s of the measured portion of the sample can be performed by considering the voltage measured across that portion, and the current through the right branch of the circuit. However, due to the possible asymmetry in the two branches, I cannot calculate the current through this branch directly without knowledge of the total resistance of each branch. As such I rewrite R_s in terms of V_s, I, V_{TL}, and $R_{TL.}$

$$I_R = I - I_L = I - \frac{V_{TL}}{R_{TL}} \tag{7}$$

$$V = V_{TR} + V_{TL} \tag{8}$$

$$V = IR_T \tag{9}$$

$$V_s = I_R R_s \tag{10}$$

$$R_s = \frac{V_s}{I_R} = \frac{V_s}{I - I_L} = \frac{V_s}{I - \frac{V_{TL}}{R_{TL}}} \tag{11}$$

From this formulation of R_s, I perform various steps of algebraic manipulation to write it into what becomes a quadratic equation in quantity ρ. Resistivity here is assumed to be constant between the portions of the crystal being strained and those not being strained. More precise estimates of this can be considered later, though due to the nature of the strain cell, portions of the crystal embedded within the mounting epoxy should undergo no mechanical deformation, ρ will remain independent of strain. This should prove to only slightly alter the final result of the estimates.

$$R_s I - R_s \frac{V_{TL}}{R_{TL}} = V_s \tag{12}$$

$$R_s R_{TL} I - R_s V_{TL} = V_s R_{TL} \tag{13}$$

Here I utilize the known fact that $V_{TL} = V_{TR}$, due to the parallel structure of the current flow. This simplification results in the final equations for resistance.

$$R_s R_{TL} I - V_s R_{TL} - R_s V_{TR} = 0 \tag{14}$$

Since V_{TR} is not a measured quantity in these experiments, it is prudent to rewrite the final term in terms of V_s and other measured quantities as shown below.

$$V_{TL} = V_{TR} = I_R\left(R_s + R_{s'} + R_{RC}\right) = \frac{V_s}{R_s}(R_s + R_{s'} + R_{RC}) = V_s + V_{s'} + \frac{V_s}{R_s}R_{RC} \tag{15}$$

Unfortunately, this transformation now adds $V_{s'}$ the voltage drop across the portion of the crystal on the right branch not measured. However, since $\rho_s = \rho_{s'}$ and the current running through them is constant, I_R, one can rewrite $V_{s'}$ in terms of V_s.

$$R_s = \frac{\rho\, l_s}{A}\ ; R_{s'} = \frac{\rho\, l_{s'}}{A}\ ; R_L = \frac{\rho\, l_L}{A} \tag{16}$$

$$I_{s'} = I_s \tag{17}$$

$$\frac{V_{s'}}{R_{s'}} = \frac{V_s}{R_s} \tag{18}$$

$$\frac{V_{s'}}{\frac{\rho l_{s'}}{A}} = \frac{V_s}{\frac{\rho l_s}{A}} \tag{19}$$

$$V_{s'} = V_s\left(\frac{l_{s'}}{l_s}\right) = V_s\left(\frac{l_R - l_s}{l_s}\right) \tag{20}$$

Note here that $l_{s'}$ is the length of the crystal unmeasured by the probe and should be equal to the difference in the total length of the right portion of crystal and the length of crystal measured, l_s.

$$R_s R_{TL} I - V_s R_{TL} - R_s\left(V_s + V_{s'} + \frac{V_s}{R_s}R_{RC}\right) = 0 \tag{21}$$

Now I choose to expand the equation in terms of all labeled quantities in the circuit diagram.

$$R_s(R_L + R_{TL})I - V_s(R_L + R_{LC}) - R_s\left(V_s + V_{s'} + \frac{V_s}{R_s}R_{RC}\right) = 0 \tag{22}$$

Finally, I replace all resistances with the respective resistivities, and geometric factors as noted earlier. Now all that needs to be done is to solve for ρ through your favorite equation solver, or by hand if your Mathematic subscription expired as mine did.

$$\rho^2\left(I\frac{1}{A^2}l_s l_L\right)+\rho\left(R_{LC}I\frac{1}{A}l_s-V_s\frac{1}{A}l_L-V_s\frac{1}{A}l_s-V_s\frac{1}{A}(l_R-l_s)\right)-R_{RC}V_s=0 \qquad (23)$$

After solving for ρ and noting that $\sigma = \rho^{-1}$, a value for conductivity can be obtained and is shown below.

$$\sigma=\frac{2I\frac{1}{A^2}l_s l_L}{-\left(R_{LC}I\frac{1}{A}l_s-V_s\frac{1}{A}(l_R+l_L)\right)\pm\sqrt{\left(\left(R_{LC}I\frac{1}{A}l_s-V_s\frac{1}{A}(l_R+l_L)\right)^2-4\left(I\frac{1}{A^2}l_s l_L\right)(-R_{RC}V_s)\right)}} \qquad (24)$$

Replacing values in equation 25 here with the appropriate thermal conductivity values yields equation 2 in chapter 5.